N ° d'ordre NNT : 2018LYSEI062

THÈSE de DOCTORAT DE L'UNIVERSITE DE LYON

opére au sein de

l'Institut National des Sciences Appliquées de Lyon

École doctorale 162

Mécanique, Énergétique, Génie Civil, Acoustique

Spécialité :

MÉCANIQUE

Thèse soutenue le 13 juillet 2018, par :

Arthur Glacet

Ingénieur en mécanique

Study of Quasi-Periodic Architectured materials :

Vibrations, Dynamic Fracture and Homogenization

Devant le Jury composé de :

KONDO DJIMÉDO	Professeur, Université Pierre-et-Marie-Curie	Rapporteur
LAZARUS VÉRONIQUE	Professeur associé, ENSTA ParisTech	Rapporteur
MORESTIN FABRICE	Professeur, INSA-Lyon	Examinateur
MOSSERI RÉMY	Directeur de recherche, Université Pierre-et-Marie-Curie	Examinateur
RÉTHORÉ JULIEN	Directeur de recherche CNRS, Centrale Nantes	Co-Directeur de thèse
TANGUY ANNE	Professeur , INSA-Lyon,	Directrice de thèse

LaMCoS - UMR CNRS 5259 - INSA de Lyon

20, avenue Albert Einstein, 69621 Villeurbanne Cedex (FRANCE)

Département FEDORA – INSA Lyon - Ecoles Doctorales – Quinquennal 2016-2020

SIGLE	ECOLE DOCTORALE	NOM ET COORDONNEES DU RESPONSABLE
CHIMIE	**CHIMIE DE LYON** **http://www.edchimie-lyon.fr** Sec : Renée EL MELHEM Bat Blaise Pascal 3e etage secretariat@edchimie-lyon.fr Insa : R. GOURDON	M. Stéphane DANIELE Institut de Recherches sur la Catalyse et l'Environnement de Lyon IRCELYON-UMR 5256 Équipe CDFA 2 avenue Albert Einstein 69626 Villeurbanne cedex directeur@edchimie-lyon.fr
E.E.A.	**ELECTRONIQUE, ELECTROTECHNIQUE, AUTOMATIQUE** **http://edeea.ec-lyon.fr** Sec : M.C. HAVGOUDOUKIAN Ecole-Doctorale.eea@ec-lyon.fr	M. Gérard SCORLETTI Ecole Centrale de Lyon 36 avenue Guy de Collongue 69134 ECULLY Tél : 04.72.18 60.97 Fax : 04 78 43 37 17 Gerard.scorletti@ec-lyon.fr
E2M2	**EVOLUTION, ECOSYSTEME, MICROBIOLOGIE, MODELISATION** **http://e2m2.universite-lyon.fr** Sec : Sylvie ROBERJOT Bât Atrium - UCB Lyon 1 04.72.44.83.62 Insa : H. CHARLES secretariat.e2m2@univ-lyon1.fr	M. Fabrice CORDEY CNRS UMR 5276 Lab. de géologie de Lyon Université Claude Bernard Lyon 1 Bât Géode 2 rue Raphaël Dubois 69622 VILLEURBANNE Cédex Tél : 06.07.53.89.13 cordey@univ-lyon1.fr
EDISS	**INTERDISCIPLINAIRE SCIENCES-SANTE** **http://www.ediss-lyon.fr** Sec : Sylvie ROBERJOT Bât Atrium - UCB Lyon 1 04.72.44.83.62 Insa : M. LAGARDE secretariat.ediss@univ-lyon1.fr	Mme Emmanuelle CANET-SOULAS INSERM U1060, CarMeN lab, Univ. Lyon 1 Bâtiment IMBL 11 avenue Jean Capelle INSA de Lyon 696621 Villeurbanne Tél : 04.72.68.49.09 Fax :04 72 68 49 16 Emmanuelle.canet@univ-lyon1.fr
INFOMATHS	**INFORMATIQUE ET MATHEMATIQUES** **http://infomaths.univ-lyon1.fr** Sec :Renée EL MELHEM Bat Blaise Pascal, 3e étage Tél : 04.72. 43. 80. 46 Fax : 04.72.43.16.87 infomaths@univ-lyon1.fr	M. Luca ZAMBONI Bâtiment Braconnier 43 Boulevard du 11 novembre 1918 69622 VILLEURBANNE Cedex Tél :04 26 23 45 52 zamboni@maths.univ-lyon1.fr
Matériaux	**MATERIAUX DE LYON** **http://ed34.universite-lyon.fr** Sec : Marion COMBE Tél:04-72-43-71-70 –Fax : 87.12 Bat. Direction ed.materiaux@insa-lyon.fr	M. Jean-Yves BUFFIERE INSA de Lyon MATEIS Bâtiment Saint Exupéry 7 avenue Jean Capelle 69621 VILLEURBANNE Cedex Tél : 04.72.43 71.70 Fax 04 72 43 85 28 Ed.materiaux@insa-lyon.fr
MEGA	**MECANIQUE, ENERGETIQUE, GENIE CIVIL, ACOUSTIQUE** **http://mega.universite-lyon.fr** Sec : Marion COMBE Tél:04-72-43-71-70 –Fax : 87.12 Bat. Direction mega@insa-lyon.fr	M. Philippe BOISSE INSA de Lyon Laboratoire LAMCOS Bâtiment Jacquard 25 bis avenue Jean Capelle 69621 VILLEURBANNE Cedex Tél : 04.72 .43.71.70 Fax : 04 72 43 72 37 Philippe.boisse@insa-lyon.fr
ScSo	**ScSo*** **http://recherche.univ-lyon2.fr/scso/** Sec : Viviane POLSINELLI Brigitte DUBOIS Insa : J.Y. TOUSSAINT Tél : 04 78 69 72 76 viviane.polsinelli@univ-lyon2.fr	M. Christian MONTES Université Lyon 2 86 rue Pasteur 69365 LYON Cedex 07 Christian.montes@univ-lyon2.fr

*ScSo : Histoire, Géographie, Aménagement, Urbanisme, Archéologie, Science politique, Sociologie, Anthropologie

Résumé

Les Structures atomiques Quasi-périodiques (QP) possèdent des propriétés particulières, notamment dans le domaine vibrationnel. Il pourrait être intéressant de pouvoir transférer ces propriétés à des méta-matériaux macroscopiques. Des réseaux de poutres quasi-périodiques 2D sont étudiés dans cette thèse dans le cadre du modèle élément finis (EF) poutre Euler Bernoulli. Ces réseaux de poutres peuvent facilement être produits par fabrication additive ou par découpe laser. Il est possible de faire varier l'élancement des poutres (le ratio hauteur sur longueur) qui est un paramètre intéressant pour modifier la réponse mécanique du réseau. En utilisant la méthode EF, l'influence de l'élancement des poutres sur la réponse vibratoire des réseaux de poutres QP est étudiée. La méthode numérique Kernel Polynomial (KPM) est adaptée avec succès de la dynamique moléculaire aux réseaux de poutres pour étudier leurs modes de vibration sans avoir à diagonaliser complètement la matrice dynamique. Les réseaux de poutres QP présentent des propriétés similaires à leur compère atomique : en particulier la localisation de modes sur des sous-structures et une relation de dispersion hiérarchisée.
Le comportement à la fracture est aussi étudié étant donné que les symétries présentes dans les QP pourraient permettre des réseaux de poutres ne présentant pas de plans faibles pour la propagation de fissures. Cela a été démontré d'après des calculs EF statiques avec un critère de fracture fragile sur l'énergie de déformation. Les simulations statiques ne suffisent pas car elles ne peuvent pas capturer les phénomènes dynamiques complexes qui apparaissent lors de la fissuration fragile. Les propriétés de vibration du QP pourraient aussi avoir un impact sur la propagation dynamique de fissure. Un modèle dynamique de fissuration est développé afin d'étudier l'impact de l'élancement sur la capacité des réseaux de poutres QP à dissiper de l'énergie par fissuration .
Finalement une méthode Coarse Graining est développée pour identifier un milieu Cosserat continu équivalant au réseau de poutres QP pour différentes échelles. Cette méthode permet d'identifier la densité, les déformations, les contraintes et donc les modules d'élasticité du milieu Cosserat équivalent, permettant ainsi une meilleure compréhension du rôle des sous structures précédemment identifiées.

MOTS CLÉS: Quasi-periodique, Éléments Finis, Réseaux de Poutres , Vibration , Fracture, Coarse Graining.

Abstract

Quasi periodic (QP) structures have shown peculiar properties in the atomistic domain, especially the vibrational one. It could be interesting to be able to transpose these properties in macroscopic meta-materials. Quasi periodic 2D beam lattices are studied in this thesis due to the simplicity of the Euler Bernoulli finite element (FE) model. These beam lattices can easily be produced by additive manufacturing or by laser cutting. It is possible to vary the beam slenderness (i.e the ratio of height over length) that is a interesting parameter to modify the mechanical response of the lattice. Using finite element method, the influence of the beam slenderness over the vibration behavior of the QP beam lattices will be studied. The Kernel Polynomial numerical Method (KPM) is successfully adapted from molecular dynamics simulations in order to study vibrational modes of FE beam lattices without having to fully diagonalize the dynamical matrix. The QP lattices show similar properties as their atomic counterpart e.g mode localization over sub-stuctures and hierarchical dispersion relation.
The fracture behavior is also studied, as the special symmetries allowed by the quasi periodicity could result in beam lattices without weak planes for crack propagation. It was proved to be true from static FE simulations with a brittle strain energy breaking criterion. Static simulations were not enough and do not grasp the complex dynamical phenomena taking place in brittle fracture. A dynamic crack propagation model was thus developed. The vibrational properties of quasi periodic structures could also have an impact on the dynamic crack propagation. Several simulations are run in order to study the impact of the slenderness on the energy dissipated by fracture of QP lattices.
Finally, a coarse graining method (CG) was developed to identify a continuous Cosserat medium at different scales from the FE beam model. This CG method allows to identify, density, strain , stress and elastic moduli of an equivalent continuous Cosserat. This allows a better understanding of the role of previously identified characteristic sub structures.

KEYWORDS: Quasi-periodic,Finite Elements, Beam lattices , Vibration ,Fracture, Coarse Graining.

Table des matières

Table des figures

Liste des tableaux

Introduction

Quasi-periodic (QP) structures have been first studied in the mathematical domain. Although Roger Penrose is not the first to have discovered quasi-periodic tilings, he is the first who found simpler tilings with fewer different tiles. After the golden triangles and kite & dart ones, many other quasi periodic tilings have been discovered and new ways of creating them too, such as projection from higher dimension allowing also to create periodic approximations ([**?**] and [**?**]). Quasi-periodic structures are structures of interest due to the peculiar properties inherited from their quasi-periodicity. Their organization at different scales or the symmetries that they support differentiate them from both random and periodic organizations. The kite & dart tilings for exemple have regained interest after the discovery of atomistic samples with the same structures [**?**]. Quasi-periodic atomic samples are called quasi-crystals.

Quasi-crystals have been widely studied for their atomistic dynamics, phononic, magnetic and electronic properties [**?**, **?**, **?**]. These structures exhibit complex vibrational behavior, including a set of frequency ranges in which no propagative wave exists [**?**, **?**], *i.e.* band gaps. Band gaps can lead to interesting applications in various domains [**?**, **?**]. Such materials can create band gap in their vibrational mechanical response while being isotropic regarding elasticity or wave propagation for example whereas for having such interesting properties, their periodic counterpart are anisotropic. This considerably increases the difficulty for modeling their behaviour and optimizing their design.

Similar properties can also be found in meta-materials, in which an internal micro-scale architectured structure can create interesting behavior at a larger scale [**?**]. Meta-materials can be created in various ways, often by assembling simple elements in a periodic or quasi-periodic pattern (cylindrical rod in a fluid is a common example) in order to exhibit physical properties resulting from the chosen substructure more than from their constitutive parts. Meta-materials have been first studied by physicists for their electromagnetic, optical and thermodynamic properties, therefore it is often called *mechanical* meta-material when the mechanical properties are studied. As a particular case, lattice materials are interesting in many fields of application because of their low density. Due to this low density, the question regarding their mechanical properties and their integrity is important.

The recent development of additive manufacturing gives the opportunity to produce

metamaterials like closed cellular materials efficiently,*i.e.* with a perfect control of the cell shape and distribution. Additive manufactured metamaterials can be designed to exhibit unusual macroscopic behavior due to their internal structure as in ([**?**] and [**?**]). While, their effective elastic properties and energy absorption capabilities under compression have been widely studied [**?**, **?**], very little has been done on their fracture behavior. Furthermore, in the case of a periodic lattice, weak orientations exist [**?**], giving rise to directionality effects that intrinsically weaken this kind of architectures.

Most of the work that has been done up to now focuses on the identification of fracture toughness K_c used in theory of linear elastic fracture mechanics (LEFM) ([**?**] [**?**]), although the possiblility of such a continuous description is still a matter of debate. Indeed the local phenomena taking place in the fracture of continuous linear-elastic materials and in fracture of beam lattices are completely different and it can become impossible to identify a fracture toughness K_c. Moreover, the scale ratio between the crack size and the micro structure in beam lattices can be problematic to the use of LEFM. In some works the fracture behavior is identified from crack propagation simulation on an homogenized continuous material ([**?**] and [**?**]) which is once again a questionable hypothesis. More can be found in this review [**?**].

Being able to model beam lattices by a continuous elastic material is a needed step in order to simplify numerical models and to shorten simulation times. Classical homogenization methods allow identifying homogeneous medium easily only for periodic structures [**?**] and without the ability to take into account heterogeneity that has a dominant role in stress concentration, crack initiation and crack propagation [**?**] [**?**]. It has been shown that classical elasticity is not always able to exhibit the peculiar mechanical properties of architectured materials, and that generalized continuum is a better candidate [**?**] [**?**]. Such continuum introduces additional degrees of freedom (Cosserat, micomorphic media [**?**]...) or higher order gradients of the displacement field (second gradient materials [**?**]...). Coarse Graining (CG) methods allow the identification of an equivalent continuous material while keeping heterogeneity at the desired scale for any type of discrete structures (periodic, amorphous or quasi-periodic). This method has already been applied at the atomic scale or for granular materials in order to identify a classic or Cosserat equivalent continuum [**?**, **?**].

The analysis of lattice materials is usually limited to periodic patterns. But, using additive manufacturing there is no shape limitation and quasi-periodic arrangements can be obtained. Considering that quasi-periodic structures have demonstrated unique properties regarding various physical phenomena (*e.g.* to store energy in local non-propagative vibration modes or to resist to the propagation of defects), it should be interesting to produce additive manufactured quasi-periodic lattices that inherit outstanding properties from their specific arrangement. Moreover, the macroscopic beam structure offers additional possibilities in terms of large scale interactions and control parameters for tuning the vibrational properties.

The mechanical and vibrational properties of quasi-periodic and of amorphous structures are related to complex mathematical problems due to the impossibility of periodic simplifications. Therefore, in order to solve these problems, big size matrix problems have to be dealt with. Moreover, usual Fourier transform-based computational tools, or Bloch Wave expansions that are very interesting for periodic structures [**?**] would be very unefficient for such systems.

In order to study the vibrational, mechanical and dynamic failure of quasi-periodic beam lattices, Euler-Bernoulli finite element (FE) beams will be used as a modeling tool and several numerical methods will be developed in order to overcome the special challenges due to quasi-periodic organizations.

A first chapter will be dedicated to the reminder of models used in this work *i.e.* FE euler beam model, discrete system vibrations and Cosserat medium characteristics. A second chapter will focus on the vibrational studies. The numerical approaches followed in this thesis deal with completely resolved calculations on very large matrices, thus avoiding the required simplifications associated to (even highly and recently elaborated) homogeneization tools as in [**?**]. In the later case, the degree of spatial resolution that depends on the waves frequency is crucial for an accurate description, as well as the hypotheses concerning the order of expansion of the constitutive laws in the different order parameters (displacements and rotations of beam nodes for example) [**?**]. In contrary, our method allows for direct insights into the dynamical behaviour at any vibrational frequency of non-periodic systems, including the description of possible localized vibrations that are difficult to identify and to take into account in homogeneization procedures [**?**, **?**, **?**].

A third chapter will be dedicated to crack propagation in FE beam model, using a strain energy failure criterion. A static and dynamic FE crack propagation model is developed in order to simulate the fracture of periodic and quasi periodic beam lattices. The influence of slenderness on the energy dissipation behavior of QP lattices will be studied to analyze the influence of the elementary properties of the lattice onto its macroscopic behaviour.

The last chapter focuses on the development of a coherent coarse graining (CG) method to identify an equivalent continuous Cosserat medium from FE beam lattice simulations. The CG method will be applied firstly on periodic lattice for validation purposes and then to the QP lattices to better understand the properties emerging for the peculiar organization of the quasi periodic lattices at different scales.

Chapitre 1

Models

Contents

1.1 Quasi-Periodic Structures

Quasi periodic structures have regained interest after the discovery of quasi crystals by Dan Shetchman in 1982. He observed an alloy producing diffraction pattern with a symmetry of order 5. The sample has a large scale organization while having a symmetry of order 5, that is impossible for classical crystals. The atomic organization thus needs to be quasi periodic. However, quasi periodic structures have been studied previously by mathematicians.

1.1.1 Quasi-Periodic Construction

The Fibonacci chain is a classical example of a 1D quasi periodic structure that can be used to introduce the different ways of constructing such structures. The Fibonacci chain is alternating long (L) and short (S) segments with the length ratio between L and S being the golden ratio, an irrational number. A first way of constructing the chain is to use a substitution or subdivision method : starting from a segment, at each step of the construction each L is substituted by LS and S becomes L. 3 steps of the subdivision method are presented in figure.1.1.

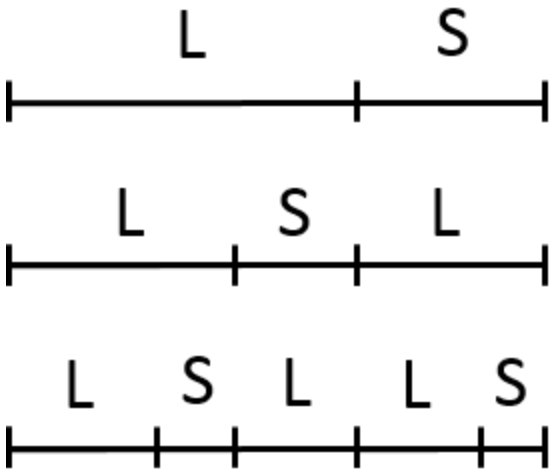

FIGURE 1.1 – 3 steps of the subdivision method to create a Fibonacci chain.

An other method to construct the Fibonacci chain is the slicing and projection method. This method starts from a periodic grid, here a square grid. Then the grid is sliced by a tilted line. The line is tilted at an irrational angle, here again related to the golden ratio. The part of the grid bellow the line is removed and the nodes closest to the line are projected onto it. This produces the Fibonacci chain. As the line is tilted at an irrational number it is easy to see that the pattern projected onto the line will never repeat itself. This method also allows to create periodic approximate by using a rational

approximation of the golden ratio. The figure.1.2 illustrates the method.

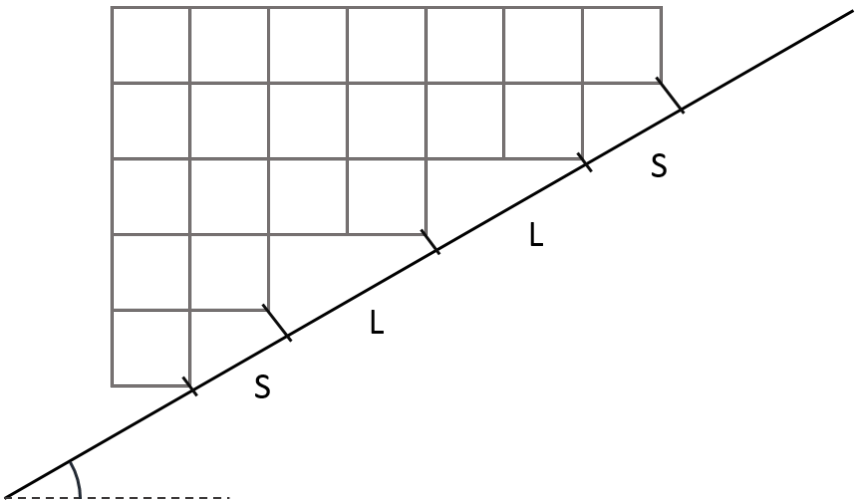

FIGURE 1.2 – Example of the slice and projection method to create a Fibonacci chain.

This last method can also be used to obtain 2D tiling by starting from a higher dimension grid sliced by a hyper-plane tilted at an irrational angle. This can produce the octogonal Penrose tiling. The figure.1.3 shows a fourth approximant of the octogonal Penrose tiling. This tiling can easily be transformed into a beam lattice by replacing each edge by a beam.

1.1.2 QP Symmetries

One property of the QP is the uniformity. One can easily identify QP repetitions of patterns into the QP tiling. Some of these patterns are highlighted in figure.1.4. In fact, any pattern (as big as wanted) can be found an infinite amount of time into the infinite QP tiling. The mean distance between these patterns increases with their size. In crystals the distance of repetition is constant and equals to the period of the grid.

The uniformity properties imply that for any selected pattern the tiling can be translated so that the pattern is invariant by translation. Moreover several patterns can coincide and they are separated by regions that do not match. The same can be observed for rotational symmetries. It can be shown that if a two-dimensional tiling contains more than a single point, about which an n-fold rotation ($n > 2$) brings it into perfect coincidence with itself, then the tiling is necessarily periodic. Thus QP tilings having a n-fold symmetry cannot contain more than a single point of ”exact” n-fold symmetry. None the less as for translation any patch of the rotated mesh can be found in the original mesh and patches of coincident tiles are separated by regions of non matching tiles. This is illustrated in the figure.1.5.

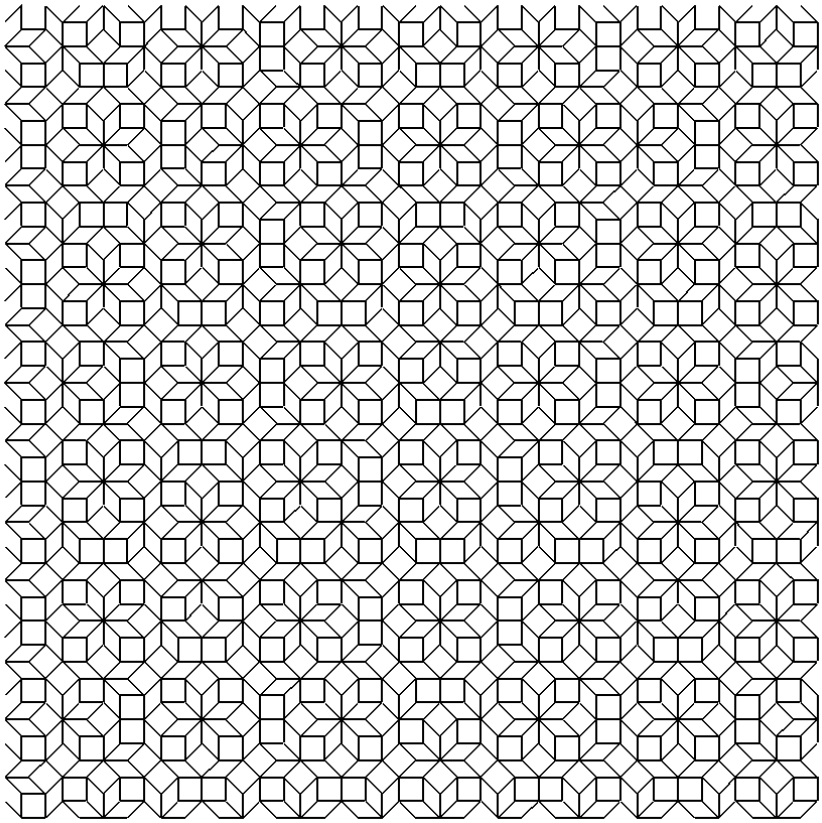

FIGURE 1.3 – 4th approximant of Penrose tiling beam structure.

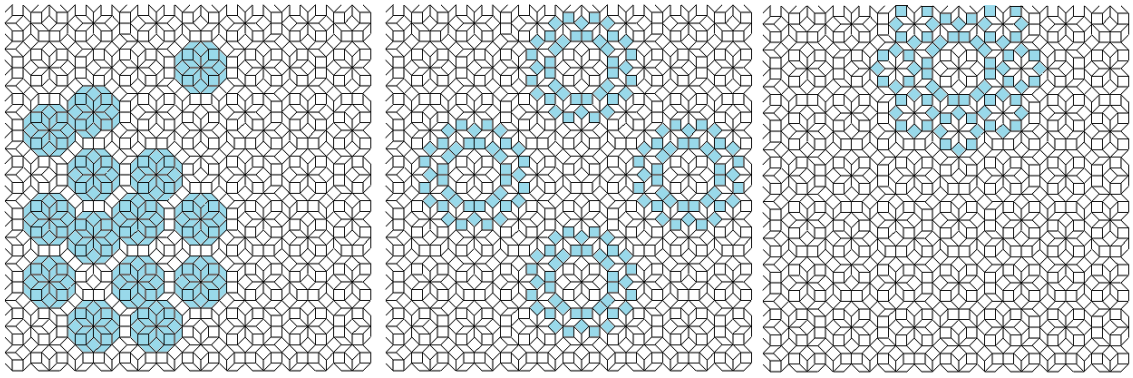

FIGURE 1.4 – Identification of patterns of increasing size in a 4th approximant of Penrose tiling beam structure.

An other way to look at symmetries is that the original and the transformed tilings contain the same statistical distribution of patterns of arbitrary size. Two crystals whose

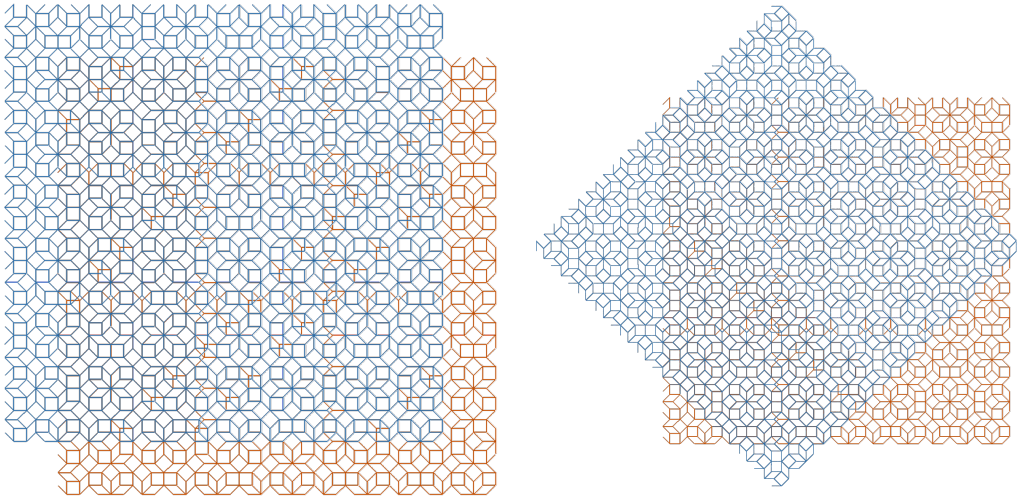

(a) (b)

FIGURE 1.5 – Superposition of translated(a) and rotated(b) 4th approximant of Penrose lattice.

patterns densities are statistically the same in this sense are called *indistinguishable*, a term which was coined by Dan Rokhsar, David Wright, and David Mermin. Only when the crystal is periodic does the notion of indistinguishability reduce back to the traditional notion of symmetries.

1.2 QP beam lattices

QP beam lattices could exhibit intresting mechanical beahaviour emerging from their quasi-periodicity. Two sets of quasi periodic lattices will be studied in this thesis :

The octohedric Penrose tiling is later used for its ability to create a periodic approximant to the quasi-periodic tiling thus allowing the use of periodic boundary conditions as suggested in [**?**]. It has been shown in [**?**] that, for ferromagnetic properties, the approximant with periodic boundary conditions closely mimics the infinite lattice properties.

And the Kite and Dart (KD) Penrose lattice is studied for it's 5-fold symmetry but their is no periodic approximant to this lattice. A section of the KD is shown in figure.1.6. A 5-fold symmetry ensures a isotopic behavior at large scale that can be useful for versatile mechanical meta-material.

1.3 Beam theory

In this work we only consider 2D beam lattices thus only traction/compression and flexural loads will be considered.

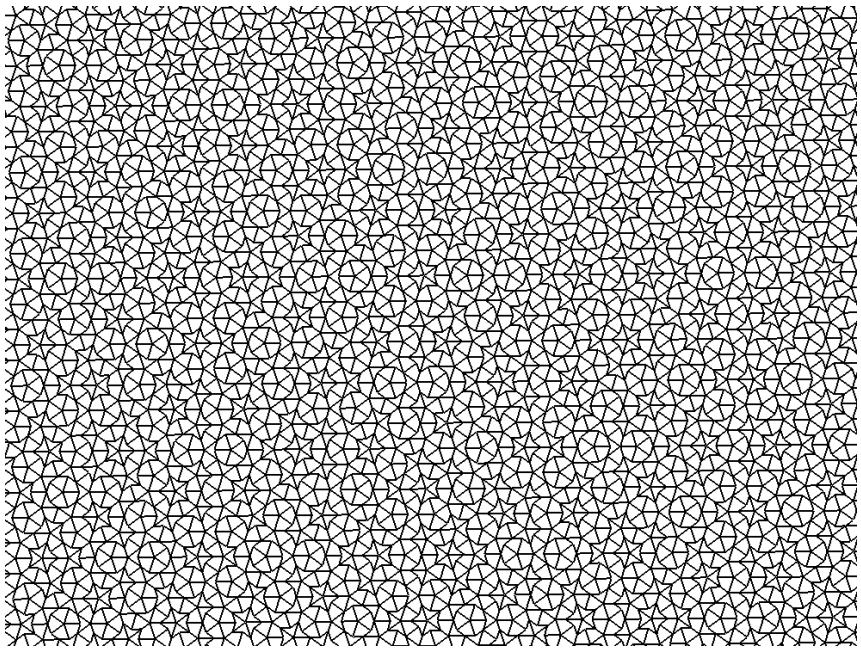

FIGURE 1.6 – Kite and Dart beam lattices.

1.3.1 Euler-Bernoulli Continuous Beam Definition

Let us consider a beam of length L and cross section S. Any point of the beam can be defined with l the curvilinear abscissa along the mean path and t the position of the point in the cross section. The cross sections are assumed to stay planar. In small displacement hypothesis, the displacement vector $\mathbf{d}(l,t)$ can be calculated as :

$$\mathbf{d}(l,t) = \begin{pmatrix} u(l) - t\theta(l) \\ v(l) \end{pmatrix} \tag{1.1}$$

Where $u(l)$ is the longitudinal displacement of the center of S, $v(l)$ the transverse displacement and $\theta(l)$ the rotation of S. From this definition the strains can be expressed as :

$$\varepsilon_{ll}(l,t) = \frac{\partial u(l)}{\partial l} - \frac{\partial \theta(l)}{\partial l} t \tag{1.2}$$

In the Euler-Bernoulli model, the shear strain energy is neglected which leads to $\frac{\partial v(l)}{\partial l} = \theta(l)$. It can be shown that the hypothesis of negligible shear is valid if the length L of the beam is ten times bigger than the maximum transverse position t. Thus the derivative of the transversal displacement along the mean path is equal to the rotation of the cross section. Then by using a simple Hooke's linear Elastic law $\sigma_{ll} = E\varepsilon_{ll}$ one can obtain the following relation :

$$\sigma_{ll}(l,t) = E\frac{\partial u(l)}{\partial l} - E\frac{\partial^2 v(l)}{\partial l^2}t \tag{1.3}$$

by defining the Flexural momentum of S as :

$$Mf_z(l) = -\int_S \sigma_{ll}(l,t)tds = \int_S E\frac{\partial^2 v(l)}{\partial l^2}t^2 ds = E\frac{\partial^2 v(l)}{\partial l^2}I_z \tag{1.4}$$

with $I_z = \int_S t^2 ds$, We can identify the state at any point of the beam from the following equations :

$$\sigma_{ll}(l,t) = \frac{N(l)}{A} - \frac{Mfz(l)}{I_z}t \tag{1.5}$$

$$N(l) = EA\frac{\partial u(l)}{\partial l} \tag{1.6}$$

and (1.4),
where A stand for the area of the section S. This constitutive law can be written in a matrix form :

$$\boldsymbol{\sigma}(l) = \left\{ \begin{array}{c} N(l) \\ Mf_z(l) \end{array} \right\} = \left[\begin{array}{cc} EA & 0 \\ 0 & EI_z \end{array} \right] \left\{ \begin{array}{c} \dfrac{\partial u(l)}{\partial l} \\ \dfrac{\partial^2 v(l)}{\partial l^2} \end{array} \right\} = \mathbf{C}\boldsymbol{\varepsilon}(l) \tag{1.7}$$

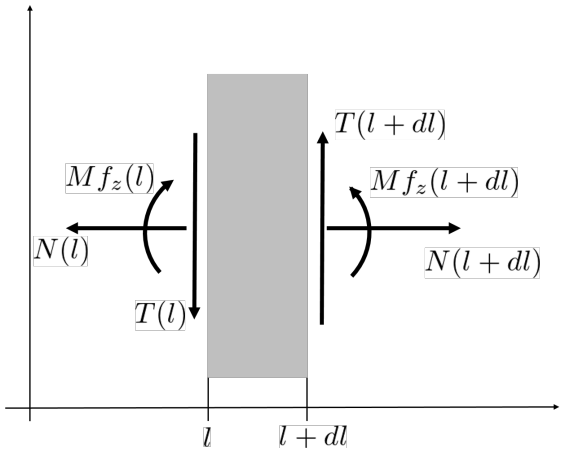

FIGURE 1.7 – Infinitesimal section of a beam

From the dynamic equilibrium of a infinitesimal section of width dl, and in the absence of distributed force or momentum, one can obtain the flowing equations :

$$\frac{\partial N(l)}{\partial l} = A\rho\ddot{u}(l) \tag{1.8}$$

$$\frac{\partial T(l)}{\partial l} = A\rho\ddot{v}(l) \tag{1.9}$$

$$\frac{\partial Mf_z(l)}{\partial l} + T(l) = I_z \rho \ddot{\theta}(l) \tag{1.10}$$

When the rotational inertia I_z of the section is neglected, the equations can be reduced to :

$$\frac{\partial N(l)}{\partial l} = A\rho\ddot{u}(l) \tag{1.11}$$

$$-\frac{\partial^2 Mf_z(l)}{\partial l^2} = A\rho\ddot{v}(l) \tag{1.12}$$

$$\frac{\partial Mf_z(l)}{\partial l} = -T(l) \tag{1.13}$$

1.3.2 Euler-Bernoulli Finite Elements Beam Definition

With Finite Elements beam modelization, the displacements, strains and stresses at any point of the beam can be deduced from the quantities at the extremities of the beam. Each node i has 3 degrees of freedom, u_i the longitudinal displacement, v_i the transverse displacement and θ_i the rotation. The external forces applied on each node i are : Fu_i the longitudinal force, Fv_i the transversal force and Mz_i the momentum. Those quantities are graphically defined in Fig.1.8. From those quantities one can create $\mathbf{q}_e$, the degrees of freedom (dof) array and $\mathbf{F}_e$ the force array for each element linking two nodes.

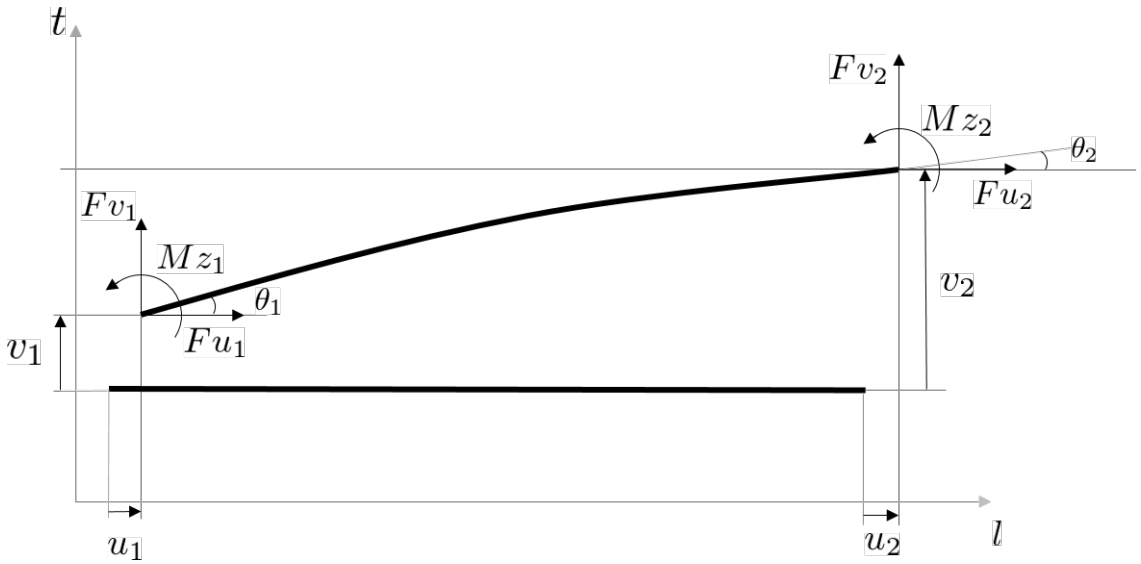

FIGURE 1.8 – FE definition of the beam element

$$\mathbf{q}_e = \{ \; u_1 \quad v_1 \quad \theta_1 \quad u_2 \quad v_2 \quad \theta_2 \; \}^t \tag{1.14}$$

$$\mathbf{F}_e = \{ \; Fu_1 \quad Fv_1 \quad Mz_1 \quad Fu_2 \quad Fv_2 \quad Mz_2 \; \}^t \tag{1.15}$$

The displacement at any point of the mean path of the beams is obtained by polynomial interpolation.

$$\mathbf{d}(l) = \left\{ \begin{array}{c} u(l) \\ v(l) \end{array} \right\} = \left\{ \begin{array}{c} u_1 p_1(l) + u_2 p_2(l) \\ v_1 p_3(l) + v_2 p_4(l) + \theta_1 p_5(l) + \theta_2 p_6(l) \end{array} \right\} = \mathbf{P}(l)\mathbf{q}_e \tag{1.16}$$

$$\mathbf{P} = \begin{bmatrix} p_1 & 0 & 0 & p_2 & 0 & 0 \\ 0 & p_3 & p_5 & 0 & p_4 & p_6 \end{bmatrix} \tag{1.17}$$

These functions p_1 to p_6 are called *shape functions* and must satisfy the boundary conditions i.e :
$u(0) = u_1$, $u(L) = u_2$, $v(0) = v_1$, $v(L) = v_2$, $\dfrac{\partial v(l)}{\partial l} = \theta(l)$, $\theta(0) = \theta_1$ and $\theta(L) = \theta_2$.
One valid choice for the shape functions is :

$$\begin{array}{ll} p_1(l) = \dfrac{L-l}{L} & p_2(l) = \dfrac{l}{L} \\ p_3(l) = 1 - 3\left(\dfrac{l}{L}\right)^2 + 2\left(\dfrac{l}{L}\right)^3 & p_4(l) = 3\left(\dfrac{l}{L}\right)^2 - 2\left(\dfrac{l}{L}\right)^3 \\ p_5(l) = L\left(\dfrac{l}{L} - 2\left(\dfrac{l}{L}\right)^2 + \left(\dfrac{l}{L}\right)^3\right) & p_6(l) = L\left(-\left(\dfrac{l}{L}\right)^2 + \left(\dfrac{l}{L}\right)^3\right) \end{array} \tag{1.18}$$

The previously defined strains can then be calculated in the beam from the nodal quantities by :

$$\boldsymbol{\varepsilon}(l) = \left\{ \begin{array}{c} \dfrac{\partial u(l)}{\partial l} \\ \dfrac{\partial^2 v(l)}{\partial l^2} \end{array} \right\} = \mathbf{B}(l).\mathbf{q}_e \tag{1.19}$$

$$\mathbf{B} = \begin{bmatrix} \dfrac{\partial p_1}{\partial l} & 0 & 0 & \dfrac{\partial p_2}{\partial l} & 0 & 0 \\ 0 & \dfrac{\partial^2 p_3}{\partial l^2} & \dfrac{\partial^2 p_5}{\partial l^2} & 0 & \dfrac{\partial^2 p_4}{\partial l^2} & \dfrac{\partial^2 p_6}{\partial l^2} \end{bmatrix} \tag{1.20}$$

1.3.3 Weak Formulation

Starting from the dynamic equilibrium equations one can apply the virtual power principle to obtain the following equations :

$$\int_L \frac{\partial N(l)}{\partial l} u^*(l) dl - \int_L \frac{\partial^2 M f_z(l)}{\partial l^2} v^*(l) dl = \int_L \rho A \ddot{u}(l) u^*(l) dl + \int_L \rho A \ddot{v}(l) v^*(l) dl \tag{1.21}$$

Using divergence flux theorem :

$$\begin{aligned} [N(l)u^*(l)]_L^0 - \int_L N(l) \frac{\partial u^*(l)}{\partial l} dl - [\frac{\partial M f_z(l)}{\partial l} v^*(l)]_L^0 + \int_L \frac{\partial M f_z(l)}{\partial l} \frac{\partial v^*(l)}{\partial l} dl \\ = \int_L \rho A \ddot{u}(l) u^*(l) dl + \int_L \rho A \ddot{v}(l) v^*(l) dl \end{aligned} \tag{1.22}$$

$$[N(l)u^*(l)]_L^0 - \int_L N(l).\frac{\partial u^*(l)}{\partial l}dl - [\frac{\partial Mf_z(l)}{\partial l}v^*(l)]_L^0 + [Mf_z(l)\frac{\partial v^*(l)}{\partial l}]_L^0 - \int_L Mf_z(l)\frac{\partial^2 v^*(l)}{\partial l^2}dl = \int_L \rho A\ddot{u}(l)u^*(l)dl + \int_L \rho A\ddot{v}(l)v^*(l)dl \quad (1.23)$$

using (1.13) one get,

$$\int_L N(l)\frac{\partial u^*(l)}{\partial l}dl + \int_L Mf_z(l)\frac{\partial^2 v^*(l)}{\partial l^2}dl + \int_L \rho A\ddot{u}(l)u^*(l)dl + \int_L \rho A\ddot{v}(l)v^*(l)dl = [N(l)u^*(l)]_L^0 + [T(l)v^*(l)]_L^0 + [Mf_z(l)\theta^*(l)]_L^0 \quad (1.24)$$

and using the eq.(1.6) and (1.4).

$$\int_L \frac{\partial u(l)}{\partial l}EA\frac{\partial u^*(l)}{\partial l}dl + \int_L \frac{\partial^2 v(l)}{\partial l^2}EI_z\frac{\partial^2 v^*(l)}{\partial l^2}dl + \int_L \rho A\ddot{u}(l)u^*(l) + \int_L \rho A\ddot{v}(l)v^*(l)dl = [N(l)u^*(l)]_L^0 + [T(l)v^*(l)]_L^0 + [Mf_z(l)\theta^*(l)]_L^0 \quad (1.25)$$

Regrouping terms in vector notation using the definitions (1.7) and (1.16).

$$\int_L \boldsymbol{\varepsilon}^t(l)\mathbf{C}\boldsymbol{\varepsilon}(l)dl + \int_L \ddot{\mathbf{d}}^t \begin{bmatrix} \rho A & 0 \\ 0 & \rho A \end{bmatrix} \mathbf{d}^*(l)dl = [N(l)u^*(l)]_L^0 + [T(l)v^*(l)]_L^0 + [Mf_z(l)\theta^*(l)]_L^0 \quad (1.26)$$

And using the FE definitions eq.(1.16) and (1.19) :

$$\int_L \mathbf{q}_e^t\mathbf{B}^t\mathbf{C}\mathbf{B}\mathbf{q}_e^* dl + \int_L \ddot{\mathbf{q}}_e{}^t\mathbf{P}^t \begin{bmatrix} \rho A & 0 \\ 0 & \rho A \end{bmatrix} \mathbf{P}\mathbf{q}_e^* dl = \mathbf{F}_e^t\mathbf{q}_e^* \quad (1.27)$$

The matrix formulation of the dynamic problem for one element is thus :

$$\mathbf{K}_e\mathbf{q}_e + \mathbf{M}_e\ddot{\mathbf{q}}_e = \mathbf{F}_e \quad (1.28)$$

with :

$$\begin{aligned} \mathbf{K}_e &= \textstyle\int_L \mathbf{B}^t.\mathbf{C}.\mathbf{B}dl \\ \mathbf{M}_e &= \textstyle\int_L \mathbf{P}^t.\begin{bmatrix} \rho A & 0 \\ 0 & \rho A \end{bmatrix}.\mathbf{P}dl \end{aligned} \quad (1.29)$$

Once the integration is done, the elementary stiffness matrix and the elementary mass matrix are :

$$\mathbf{K}_e = \begin{bmatrix} \frac{EA}{L} & 0 & 0 & -\frac{EA}{L} & 0 & 0 \\ 0 & 12\frac{EI}{L^3} & 6\frac{EI}{L^2} & 0 & -12\frac{EI}{L^3} & 6\frac{E}{L^2} \\ 0 & 6\frac{EI}{L^2} & 4\frac{EI}{L} & 0 & -6\frac{EI}{L^2} & 2\frac{EI}{L} \\ -\frac{ES}{L} & 0 & 0 & \frac{ES}{L} & 0 & 0 \\ 0 & -12\frac{EI}{L^3} & -6\frac{EI}{L^2} & 0 & 12\frac{EI}{L^3} & -6\frac{EI}{L^2} \\ 0 & 6\frac{EI}{L^2} & 2\frac{EI}{L} & 0 & -6\frac{EI}{L^2} & 4\frac{EI}{L} \end{bmatrix} \quad (1.30)$$

and

$$\mathbf{M}_e = \begin{bmatrix} \frac{1}{3}L\rho A & 0 & 0 & \frac{1}{6}L\rho A & 0 & 0 \\ 0 & \frac{13L\rho A}{35} & \frac{11L^2\rho A}{210} & 0 & \frac{9L\rho A}{70} & -\frac{13L^2\rho A}{420} \\ 0 & \frac{11L^2\rho A}{210} & \frac{L^3\rho A}{105} & 0 & \frac{13L^2\rho A}{420} & -\frac{L^3\rho A}{140} \\ \frac{1}{6}L\rho A & 0 & 0 & \frac{1}{3}L\rho A & 0 & 0 \\ 0 & \frac{9L\rho A}{70} & \frac{13L^2\rho A}{420} & 0 & \frac{13L\rho A}{35} & -\frac{11L^2\rho A}{210} \\ 0 & -\frac{13L^2\rho A}{420} & -\frac{L^3\rho A}{140} & 0 & -\frac{11L^2\rho A}{210} & \frac{L^3\rho A}{105} \end{bmatrix} \tag{1.31}$$

These matrices depend on three parameters :

$$\begin{aligned} &K_v = 12\frac{EI}{L^3} \text{ the flexural stiffness.} \\ &K_u = \frac{ES}{L} \text{ the traction/compression stiffness.} \\ &m = \rho SL \text{ the mass of a beam element.} \end{aligned} \tag{1.32}$$

Note that the ratio $\frac{Kv}{Ku}$, depends here only on the geometry of the beam cross section and on its length.

1.3.4 Dynamic FE problem

Once the elementary stiffness and mass matrix are obtained the matrix formulation for the full problem can be obtained by assembling these matrices using the mesh connectivity. In order to assemble the global matrices, the elementary matrices have to be rotated to accommodate the orientation of the real element in the global lattice. The full matrix problem is written :

$$\mathbf{Kq} + \mathbf{M\ddot{q}} = \mathbf{F} \tag{1.33}$$

1.4 Vibrational Properties of Discrete Systems

Once the Beam lattice has been modelized using FE, it can be seen as an assembly of interacting nodes, that is a discrete system. In this section the classical problem of 1D discrete system will be used to introduce to the vibrational Properties of discrete systems. It will be shown how a band gap can be created by changing parameters of the problem.

1.4.1 1D mono-mass spring chain

The problem is an infinite periodic chain with springs of stiffness k and mass m as can be seen in figure1.9. The dynamic equilibrium can be written on the mass n :

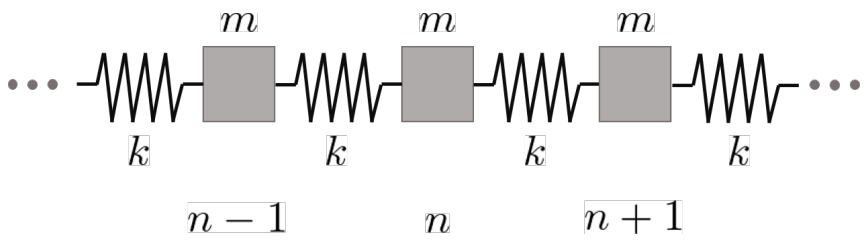

FIGURE 1.9 – infinite spring and mono-mass chain.

$$k(u^{n-1} - u^n) - k(u^n - u^{n+1}) = m\ddot{u^n} \tag{1.34}$$

With u^n being the displacement of the mass n along the chain direction and $\ddot{u^n}$ its acceleration. Studying the vibrational response of this infinite system one can assume a solution of the form :

$$u^n = Aexp(i(Kx^n - \omega t) \tag{1.35}$$

With x^n the initial position of the mass n, ω is the angular frequency and K the wave vector. This form can only be used in case of periodic systems. By substituting the solution (1.35) in the dynamic equilibrium (1.34) one obtains :

$$k(exp(i(Kx^{n-1} - \omega t) - 2exp(i(Kx^n - \omega t)) + exp(i(Kx^{n+1} - \omega t)) = -m\omega^2 exp(i(Kx^n - \omega t) \tag{1.36}$$

Lets note d the initial distance between masses, then after simplification :

$$k(exp(i(-Kd) - 2 + exp(i(Kd)) = -m\omega^2 \tag{1.37}$$

$$2k(cos(Kd) - 1) = -m\omega^2 \tag{1.38}$$

$$4k(sin^2(\frac{1}{2}Kd)) = m\omega^2 \tag{1.39}$$

This equation can be solved for $\omega \geq 0$ giving the dispersion relation

$$\omega = 2\sqrt{\frac{k}{m}}|sin(\frac{1}{2}Kd)| \tag{1.40}$$

This dispersion curve has been plotted with example values of $k = 1Nm^{-1}$,$m = 1Kg$,$d = 1m$ in figure.1.10.

1.4.2 1D by-mass spring chain

Now the infinite chain is modified by changing the mass of one over two masses as shown in figure1.11.

Writing the dynamic equilibrium on a mass m_1 and a mass m_2, the following equations are obtained :

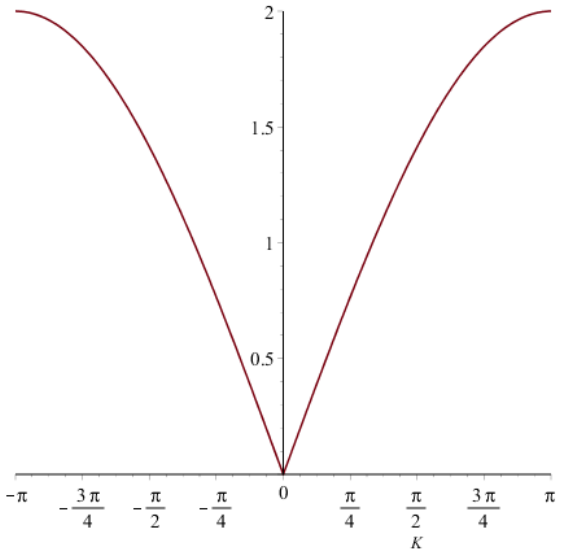

FIGURE 1.10 – dispersion curve for mono-mass chain.

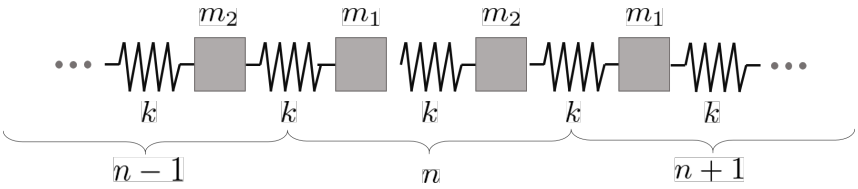

FIGURE 1.11 – infinite spring and by-mass chain.

$$\begin{aligned} k(u_2^{n-1} - u_1^n) - k(u_1^n - u_2^n) &= m_1 \ddot{u_1^n} \\ k(u_1^n - u_2^n) - k(u_2^n - u_1^{n+1}) &= m_2 \ddot{u_2^n} \end{aligned} \tag{1.41}$$

Two equations can be written, yielding to two dispersion curves. Using a vibrational solution of type :

$$\begin{aligned} u_1^n &= A_1 exp(i(Kx_1^n - \omega t) \\ u_2^n &= A_2 exp(i(Kx_2^n - \omega t) \end{aligned} \tag{1.42}$$

Dynamical equilibria become :

$$\begin{aligned} k(A_2 exp(i(Kx_2^{n-1}) - 2A_1 exp(i(Kx_1^n)) + A_2 exp(i(Kx_2^n))) &= -\omega^2 m_1 A_1 exp(i(Kx_1^n) \\ k(A_1 exp(i(Kx_1^n) - 2A_2 exp(i(Kx_2^n)) + A_2 exp(i(Kx_1^{n+1}))) &= -\omega^2 m_2 A_2 exp(i(Kx_2^n) \end{aligned} \tag{1.43}$$

Thus

$$\begin{aligned} k(A_2 exp(i(-Kd) - 2A_1 + A_2 exp(i(Kd))) &= -\omega^2 m_1 A_1 \\ k(A_1 exp(i(-Kd) - 2A_2 + A_2 exp(i(Kd))) &= -\omega^2 m_2 A_2 \end{aligned} \tag{1.44}$$

that is

$$\begin{aligned} 2k(A_2 cos(Kd) - A_1) &= -\omega^2 m_1 A_1 \\ 2k(A_1 cos(Kd) - A_2) &= -\omega^2 m_2 A_2 \end{aligned} \tag{1.45}$$

The existence of non zero solution, $(A_1, A_2) \neq (0,0)$ implies the determinant equation :

$$\begin{vmatrix} \omega^2 m_1 - 2k & 2kcos(Kd) \\ 2kcos(Kd) & \omega^2 m_2 - 2k \end{vmatrix} = 0 \tag{1.46}$$

Whose solutions are :

$$\omega_{\pm}^2 = k(\frac{1}{m_1} + \frac{1}{m_2}) \pm k\sqrt{(\frac{1}{m_1} + \frac{1}{m_2})^2 - \frac{4sin^2(\frac{1}{2}Kd)}{m_1 m_2}} \tag{1.47}$$

These dispersion curves have been plotted with example values of $k = 1Nm^{-1}$, $m_1 = 1Kg$, $m_2 = 2Kg$, $d = 1m$ in the figure.1.12 Contrary to the previous dispersion curve for the

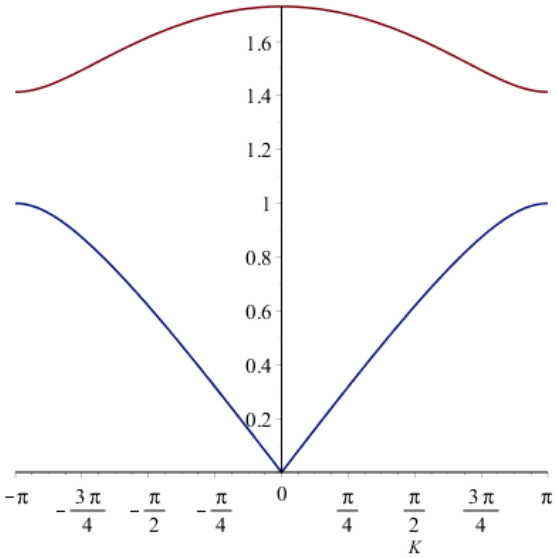

FIGURE 1.12 – dispersion curve for by-mass chain.

mono-mass chain one can observe the existence of two curves. The lower curve is called the acoustic branch while the upper curve is called the optical branch.

Whereas in the acoustic branch masses moves in phase, they vibrate against one another in opposite directions in optical branch. In ionic crystals (i.e. where there are opposite charges connected to the two species), these modes can therefore couple to electromagnetic radiation and are responsible for much of the characteristic optical behavior of such crystals. This is why, even in non-ionic crystals, these modes are called optical modes, and their dispersion curve is called the optical branch.

The band of non existing modes between the acoustic and optical branch is known as a band gap. As no modes exists in this ω region, an excitation having a angular frequency in this band gap would not propagate in the medium and give rise to an evanescent wave.

This method can be applied to obtain analytical result for periodic structures by imposing the periodicity of the wave response. It will latter be used to calculate the dispersion curves for a 2D square beam lattice but it can not be applied easily if the system studied is not periodic.

1.5 Cosserat 2D medium

In this section we present the Cosserat medium. It will be seen that the elementary elements of the Cosserat have the same dofs and interactions than the FE beam model thus making the Cosserat medium a good candidate to approximate beam lattices by a continuous medium.

1.5.1 Degrees of freedom

The three dofs for the elementary element of the 2D Cosserat are : u_x and u_y the two displacements along x and y axis and θ the rotation along the out of plan axis. One can indicate the displacement vector as :

$$\mathbf{u} = (u_x, u_y)^t \tag{1.48}$$

1.5.2 Forces and torques

Cohesive forces and torques are drawn in figure1.13 for a continous 2d system. Each edge of normal $\mathbf{i}$ transmit tangent forces $F_{ij}\mathbf{j}$ and normal forces $F_{ii}\mathbf{i}$ as well as a torque $M_i\mathbf{z}$.

The definition of the stresses and distributed torques are :

$$\begin{aligned} \mathbf{F}_{\alpha\beta} &= F_{\alpha\beta}\boldsymbol{\beta} = \sigma_{\alpha\beta} d\alpha\boldsymbol{\beta} \\ \mathbf{M}_{z\alpha} &= m_\alpha d\beta\mathbf{z} \end{aligned} \tag{1.49}$$

$d\alpha$ being the length of the sides, i.e dx or dy. Stresses and distributed torques tensors are defined as :

$$\boldsymbol{\sigma} = \begin{pmatrix} \sigma_{xx} & \sigma_{xy} \\ \sigma_{yx} & \sigma_{yy} \end{pmatrix} \tag{1.50}$$

$$\mathbf{m} = \begin{pmatrix} m_x \\ m_y \end{pmatrix} \tag{1.51}$$

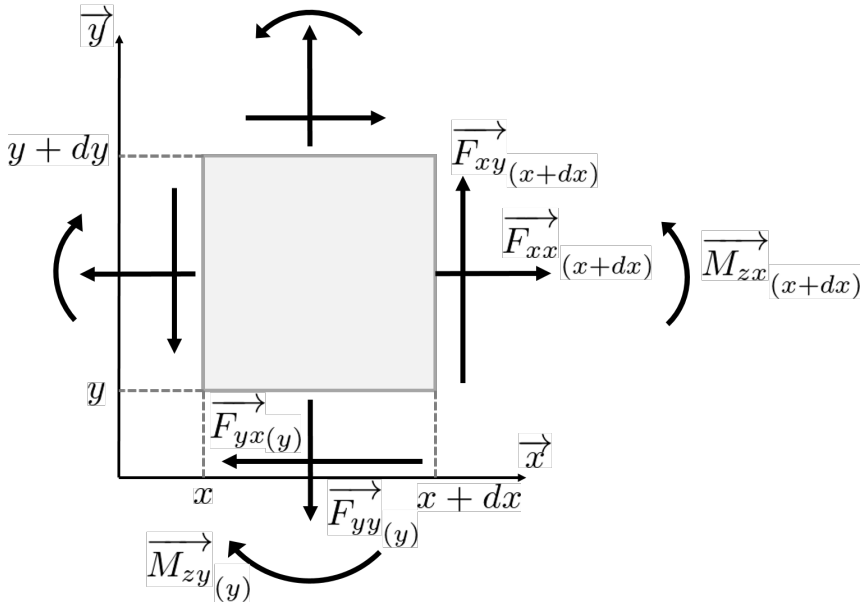

FIGURE 1.13 – Forces and torques definition.

1.5.3 Dynamical equilibrium equations

In this section the 2D Cosserat equilibrium equations will be obtained from the equilibrium of an elementary square, using the previously defined cohesive forces and torques.
-projected forces equilibrium :

$$\begin{array}{ll} \mathbf{x}: & F_{xx}(x+dx)-F_{xx}(x)+F_{yx}(y+dy)-F_{yx}(y)=\rho dxdy\ddot{u}_x \\ \mathbf{y}: & F_{yy}(y+dy)-F_{xx}(x)+F_{yx}(x+dx)-F_{yx}(x)=\rho dxdy\ddot{u}_y \end{array} \tag{1.52}$$

-projected torques equilibrium in $\{x+dx, y+dy\}$:

$$\mathbf{z}: \quad M_{zx}(x+dx)-M_{zx}(x)+M_{zy}(y+dy)-M_{zy}(y)+F_{xy}dx-F_{yx}dy=I_z dxdy\ddot{\theta} \tag{1.53}$$

The equilibrium equations can be transformed to :

$$\mathbf{div}(\boldsymbol{\sigma})=\rho\ddot{\mathbf{u}} \tag{1.54}$$

$$div(\mathbf{m})-(\sigma_{xy}-\sigma_{yx})=I_z\ddot{\theta} \tag{1.55}$$

1.5.4 Weak formulation

By writing the virtual power principle over a domain Ω as defined in figure1.14 we obtain :

$\{\forall \mathbf{u}^* \in C^1, \forall \theta^* \in C^1\}$:

$$\int_\Omega \mathbf{div}(\boldsymbol{\sigma}).\mathbf{u}^* ds+\int_\Omega div(\mathbf{m})\theta^* ds-\int_\Omega(\sigma_{xy}-\sigma_{yx})\theta^* ds=\int_\Omega \rho\ddot{\mathbf{u}}.\mathbf{u}^* ds+\int_\Omega I_z\ddot{\theta}\theta^* ds \tag{1.56}$$

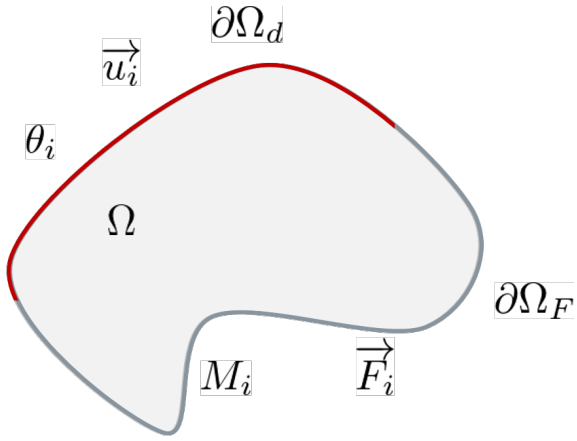

FIGURE 1.14 – Domain Ω definition.

$$-\int_\Omega \boldsymbol{\sigma} : \nabla \mathbf{u}^* ds - \int_\Omega \boldsymbol{\sigma} : \begin{bmatrix} 0 & \theta^* \\ -\theta^* & 0 \\ 0 & 0 \end{bmatrix} ds - \int_\Omega \mathbf{m}.\nabla\theta^* ds + \int_{\partial\Omega} \boldsymbol{\sigma}.\mathbf{n}.\mathbf{u}^* dl + \int_{\partial\Omega} \mathbf{m}.\mathbf{n}\theta^* dl = \int_\Omega \rho\ddot{\mathbf{u}}.\mathbf{u}^* ds + \int_\Omega I_z\ddot{\theta}\theta^* ds \quad (1.57)$$

$$\int_\Omega \boldsymbol{\sigma} : \boldsymbol{e}^* ds + \int_\Omega \mathbf{m}.\mathbf{k}^* ds + \int_\Omega \rho\ddot{\mathbf{u}}.\mathbf{u}^* ds + \int_\Omega I_z\ddot{\theta}\theta^* ds = \int_{\partial\Omega} \boldsymbol{\sigma}.\mathbf{n}.\mathbf{u}^* dl + \int_{\partial\Omega} \mathbf{m}.\mathbf{n}\theta^* dl \quad (1.58)$$

Where the strain tensor and curvature tensor are identified as :

$$\mathbf{e} = \begin{pmatrix} u_{x,x} & u_{x,y} + \theta \\ u_{y,x} - \theta & u_{y,y} \end{pmatrix} \quad (1.59)$$

$$\mathbf{k} = \begin{pmatrix} k_x \\ k_y \end{pmatrix} = \begin{pmatrix} \theta_{,x} \\ \theta_{,y} \end{pmatrix} \quad (1.60)$$

We define $\mathbf{F} = \boldsymbol{\sigma}.\mathbf{n}$ and $M = \mathbf{m}.\mathbf{n}$

$$\int_\Omega \boldsymbol{\sigma} : \boldsymbol{e}^* ds + \int_\Omega \mathbf{m}.\mathbf{k}^* ds + \int_\Omega \rho\ddot{\mathbf{u}}.\mathbf{u}^* ds + \int_\Omega I_z\ddot{\theta}\theta^* ds = \int_{\partial\Omega_d} \mathbf{F}.\mathbf{u}_\mathbf{i}^* dl + \int_{\partial\Omega_F} \mathbf{F}_\mathbf{i}.\mathbf{u}^* dl + \int_{\partial\Omega_d} M\theta_i^* dl + \int_{\partial\Omega_F} M_i\theta^* dl \quad (1.61)$$

By choosing $\mathbf{u}^*$ and θ^* as statically admissible we obtain :

$$\int_\Omega \boldsymbol{\sigma} : \boldsymbol{e}^* ds + \int_\Omega \mathbf{m}.\mathbf{k}^* ds + \int_\Omega \rho\ddot{\mathbf{u}}.\mathbf{u}^* ds + \int_\Omega I_z\ddot{\theta}\theta^* ds = \int_{\partial\Omega_F} \mathbf{F}_\mathbf{i}\mathbf{u}^* dl + \int_{\partial\Omega_F} M_i\theta^* dl \quad (1.62)$$

1.5.5 Cosserat Constitutive law

In a Cosserat medium θ is the material rotation. We can also define $\Omega = \frac{1}{2}(u_{y,x} - u_{x,y})$ the non symmetric part of displacement gradient, the classic symmetric strain tensor $\boldsymbol{\varepsilon} = \frac{1}{2}(\mathbf{grad}(\mathbf{u}) + \mathbf{grad}(\mathbf{u})^t)$, and $\Phi = \theta - \Omega$ the relative rotation. It can be noticed that $u_{x,y} + \theta = \varepsilon_{xy} + \Phi$ and $u_{y,x} + \theta = \varepsilon_{yx} - \Phi$. the two notations are used in literature.

The stresses and torques tensors can be rewritten using the Voigt notation :

$$\widehat{\boldsymbol{\sigma}} = \begin{pmatrix} \sigma_{xx} & \sigma_{yy} & \sigma_{xy} & \sigma_{yx} & m_x & m_y \end{pmatrix}^t \tag{1.63}$$

as well as the strains and curvatures tensors :

$$\widehat{\mathbf{e}} = \begin{pmatrix} e_{xx} & e_{yy} & e_{xy} & e_{yx} & k_x & k_y \end{pmatrix}^t \tag{1.64}$$

The constitutive law for a isotropic elastic Cosserat medium is :

$$\widehat{\boldsymbol{\sigma}} = \mathbf{D}.\widehat{\mathbf{e}} \tag{1.65}$$

$$\mathbf{D} = \begin{bmatrix} \lambda+2\mu & \lambda & 0 & 0 & 0 & 0 \\ \lambda & \lambda+2\mu & 0 & 0 & 0 & 0 \\ 0 & 0 & \mu+\mu_c & \mu-\mu_c & 0 & 0 \\ 0 & 0 & \mu-\mu_c & \mu+\mu_c & 0 & 0 \\ 0 & 0 & 0 & 0 & \mu_3 & 0 \\ 0 & 0 & 0 & 0 & 0 & \mu_3 \end{bmatrix} \tag{1.66}$$

1.6 Conclusion

The models, methods, equations and definitions detailed in this chapter will be used in the chapters to follow in order to study several aspects of the QP beam lattices.

Chapitre 2

Harmonic study

Contents

2.1 Introduction :

The octohedric Penrose tilling is chosen in this chapter for its ability to create a periodic approximant to the quasi-periodic tilling thus allowing the use of periodic boundary conditions as suggested in [**?**].It has been shown in [**?**] that, for ferromagnetic properties, the approximant with periodic boundary conditions closely mimics the infinite lattice properties. The numerical methods used here for the vibrational study of big systems were inspired from atomic vibration analyses and adapted to finite element modeling of large scale complex beam structures. First, the vibrational eigenmodes are computed by exact diagonalization of the dynamical matrix restricted to the beam nodes. Then, Kernel Polynomial Method (KPM) is used to calculate the complete Vibrational Density Of States (VDOS) and the Dynamical Structure Factor (DSF), giving rise to the complete dispersion relation without the need of exact diagonalization of the dynamical matrix. The KPM method is detailed by [**?**] and was adapted recently to the study of the vibrational properties of large-size atomic systems by [**?**]. We apply it here to large scale beam structures. This method allows accurate description of the vibrational properties of large scale systems, and thus a better understanding of the vibrational response of quasi-periodic structures. Thanks to this work, it will now be easy to transfer this method to the detailed vibrational study of any beam structure.

This chapter is organized as follows : first the modeling and numerical methods are explained in Section 2.2 and 2.3. These methods are firstly applied on a simple periodic beam structure in Section 2.4, in order to be validated, and to show the influence of the bending stiffness on the vibrational response. Then in Section 2.5 the methods are applied to the complete analysis of the vibrational response of a quasi-periodic Penrose approximant, including the detailed analysis of its eigenmodes.

2.2 Model

Using the FE model reminded in section 1.3 the dynamical matrix problem is :

$$\mathbf{K}.\mathbf{d} + \mathbf{M}.\mathbf{d} = \mathbf{F}. \tag{2.1}$$

Where $\mathbf{d}$ is now the dof vector whereas it was $\mathbf{q}$ in the Chapter1 as q will be used for the wave vector later on. When studying the vibrational response, the external forces on each node are zero because the system would be at equilibrium at rest, and the displacement is assumed to be a wave solution, that is :

$$\ddot{\mathbf{d}} = -\omega^2 \mathbf{d}, \tag{2.2}$$

where ω is the angular frequency of the wave. Thus the dynamical problem can be written

$$\mathbf{K}.\mathbf{d} = \omega^2 \mathbf{M}.\mathbf{d} \tag{2.3}$$

The periodic boundary conditions are imposed by modifying the previous equation thus equating the DFs of the homologous nodes. By denoting $\mathbf{M} = \mathbf{L}\mathbf{L}^t$ 2.3 becomes a classical eigenmodes problem :

$$\mathbf{H}.\mathbf{d}' = \lambda \mathbf{d}', \tag{2.4}$$

with

$$\mathbf{H} = \mathbf{L}^{-1}.\mathbf{K}.\mathbf{L}^{-t} \; ; \; \lambda = \omega^2 \; ; \; \mathbf{d}' = \mathbf{L}^t \mathbf{d}, \tag{2.5}$$

where $\mathbf{H}$ is a symmetric positive definite square matrix. As shown in section 1.3 this dynamical matrix depends on three parameters :

$$\begin{aligned} &K_v = 12\frac{EI}{L^3} \text{ the flexural stiffness.} \\ &K_u = \frac{ES}{L} \text{ the traction/compression stiffness.} \\ &m = \rho SL \text{ the mass of a beam element.} \end{aligned} \tag{2.6}$$

Note that the ratio $\frac{Kv}{Ku}$, depends here only on the geometry of the beam cross section and on its length. The influence of this ratio on the vibrational properties will be discussed latter.

Moreover, the discretization of the system on the nodes at the extremities of the beams does not allow getting insight on vibrations at a scale smaller than half of the smallest beam length, thus limiting the highest frequency reached. The highest vibrational frequency ω_{max} is of the order of the highest possible frequency supported by the smallest element, that is given by solving the equation $det(\mathbf{K_e} - \omega^2 \mathbf{M_e}) = 0$ and depends on the aspect ratio of the beams. Due to the very large number of nodes, we will solve Eq. 2.3 with numerical methods that are adapted to very large system sizes. We will compare the exact diagonalization of the matrix $\mathbf{H}$ (allowing exact identification of the modes but only for $N \lesssim 10000$) to the recursive calculation of the frequency density (VDOS) and of the dispersion relation (DSF) that will be presented later and that is not size limited.

2.3 Numerical Methods

2.3.1 Exact diagonalization

The exact diagonalization of the dynamical matrix $\mathbf{H}$ allows getting directly $\mathbf{d}'$ from Eq. (2.3), and thus the DF vector $\mathbf{d} = \mathbf{L}^{-t}.\mathbf{d}'$. The diagonalization is performed using the build in function *eigsn* in Matlab software. The calculation is limited by the system size. For sufficienlty small systems ($N \lesssim 10000$), it allows visualizing the $3 \times N$ eigenvectors that are the resonant modes of the system (see Section 2.5). It allows also for computing the participation ratio (PR) of each mode. For a given eigenmode j, the PR gives information on the ratio of particles participating in each vibration mode. It was used for example

to identify possible localized vibrations in disordered systems [**?**, **?**, **?**, **?**]. It is defined as :

$$PR(\omega) = \frac{1}{N} \frac{(\sum_i |\mathbf{u_i}|^2(\omega_j))^2}{\sum_i |\mathbf{u_i}|^4(\omega_j)} \tag{2.7}$$

where $\mathbf{u_i}$ is the displacement vector $\mathbf{u_i} = \{u_{x_i}, u_{y_i}\}$ for the ith node and ω_j the pulsation of the jth eigenmode. It means that $PR = 1/N$ when only one isolated node over N supports the vibration, while $PR = N/N = 1 = 100\%$ in case of uniform translation.

The determination of the eigenfrequencies and eigenmodes from the resolution of Equation 2.5 is highly computationaly demanding, especially for non-periodic systems. For this reason, approximate methods that do not require exact resolution of the eigenvalue problem have been developed [**?**, **?**]. The computation of several quantities like the vibrational density of states and the dynamical structure factor (spectral densiy of states) is useful for analyzing the vibrational properties of a material. They are obtained without solving the eigenvalue problem as detailed below.

2.3.2 Vibrational Density of States

The VDOS corresponds to the modal distribution. It is defined as :

$$VDOS(\omega) = \frac{1}{3N} \sum_{j=1}^{3N} \delta(\omega - \omega_j) \tag{2.8}$$

where δ is the Dirac function. Using the Kernel Polynomial Method (KPM), the VDOS can be obtained without the exact resolution of the eigenvalue problem (2.4). The KPM thus allows to compute the VDOS even for very large systems [**?**, **?**]. It is based on the approximation of the δ-function in Eq. 2.8 by a series of Tchebychev polynomials, yielding to an exact expression of the distribution of the eigenvalues without calculating the eigenvalues itself. The method is detailed in [**?**, **?**]. The starting point is the expansion of the δ-function as

$$\delta(\varepsilon - \varepsilon_j) = \frac{2}{\pi} \sqrt{1-\varepsilon^2} \sum_{b=0}^{\infty} T_b(\varepsilon) T_b(\varepsilon_j). \tag{2.9}$$

where $\varepsilon_j = 2\omega_j^2/\omega_{max}^2 - 1$. ω_{max} is the maximum frequency supported by the individual beams : it is given by the resolution of the equation $det(\mathbf{K}_e - \omega^2 \mathbf{M}_e) = 0$, thus $-1 < \varepsilon_j < 1$, T_b are Tchebychev polynomials that can be obtained either by the recurrence relation

$$T_0(\varepsilon) = 1, \tag{2.10}$$

$$T_1(\varepsilon) = 2\varepsilon, \tag{2.11}$$

$$T_b(\varepsilon) = 2\varepsilon U_{b-1}(\varepsilon) - U_{b-2}(\varepsilon). \tag{2.12}$$

or by a trigonometric definition :

$$T_b(\varepsilon) = \frac{\sin((b+1)\arccos(\varepsilon))}{\sqrt{1-\varepsilon^2}}. \tag{2.13}$$

The VDOS can thus be rewritten as

$$VDOS(\omega) \approx \frac{8\omega}{3N\pi\omega_{max}^2} \sum_{j=1}^{3N} \sum_{b=0}^{B} \gamma_b T_b(\varepsilon_j) T_b(\varepsilon) \tag{2.14}$$

where γ_b are Jackson's damping coefficients [**?**] introduced to avoid Gibbs oscillations

$$\gamma_b = \frac{(B+1-b)\cos\frac{\pi b}{B+1} + \sin\frac{\pi b}{B+1}\cot\frac{\pi}{B+1}}{B+1} \tag{2.15}$$

and B is a maximum number controlled by the desired accuracy of the calculations, the approximate solution converging to the continuous solution $VDOS(\omega)$ when B goes to infinity [**?**]. Here we chose $B = 300$. The Tchebychev momenta are defined as

$$\mu_b = \frac{1}{3N} \sum_{j=1}^{3N} T_b(\varepsilon_j) = \frac{1}{3N} \sum_{j=1}^{3N} \langle \mathbf{u}_j | T_b(\mathbf{H}_t) | \mathbf{u}_j \rangle \tag{2.16}$$

with $\mathbf{H}_t = \frac{2\mathbf{H}}{\omega_{max}^2} - \mathbf{I}$. The bth momenta can be approximated as

$$\mu_b \approx \overline{\langle \mathbf{d}_0^r | \mathbf{d}_b^r \rangle} \tag{2.17}$$

where $|\mathbf{d}_0^r\rangle$ is a $3N$ Gaussian random vector with unit norm, the upper bar is the average over R random realizations of this random vector, and $|\mathbf{d}_b^r\rangle$ follows the recurrence relations

$$\begin{aligned} |\mathbf{d}_1^r\rangle &= 2\mathbf{H}_t |\mathbf{d}_0^r\rangle, \\ |\mathbf{d}_b^r\rangle &= 2\mathbf{H}_t |\mathbf{d}_{b-1}^r\rangle - |\mathbf{d}_{b-2}^r\rangle = T_b(\mathbf{H}_t) |\mathbf{d}_0^r\rangle \end{aligned} \tag{2.18}$$

When R is large enough, the variability due to the random generation of the $\{d_0^r\}$ can be neglected [**?**]. We used $R = 30$. Using Eqs.2.132.14, the $VDOS$ can thus be computed as

$$VDOS(\omega) = \frac{4\omega}{3N\omega_{max}^2} \sum_{b=0}^{B} \gamma_b \mu_b \sin\left(2(b+1)\arcsin\left(\omega/\omega_{max}\right)\right) \tag{2.19}$$

that is a function of the angular frequency ω only, without the need of ω_j neither of $\mathbf{u}_j$.

2.3.3 Dynamical Structure Factor

The DSF is also called *Spectral Density of Energy* [**?**]. It corresponds schematically to the combined spatial and temporal Fourier transforms of the displacements inside the system, thus giving the amplitude of the harmonic waves as a function of q the wave vector and w the angular frequency. In atomistic samples, it is related to the cross-section of photons that are scattered by atomic vibrations in non-elastic x-ray or neutron scattering experiments [**?**]. For longitudinal modes for example, it is related to the spatial correlation function of density fluctuations. As an indicator of the connection between wave-vectors and frequency during the dynamical response of the system, the DSF can be used to obtain

the dispersion law. The DSF is calculated separately for transverse (T) and longitudinal (L) displacements. For longitudinal modes, it is defined by :

$$DSF_L(\omega,\mathbf{q}) = \sum_{j=1}^{3N}(\sum_{i=1}^{N}\mathbf{q}_n.\mathbf{u}_i(\omega_j)e^{\mathbf{q}.\mathbf{N}_i})^2\delta(\omega-\omega_j) \tag{2.20}$$

where $\mathbf{q}_n$ is the normalized wave vector and $\mathbf{N}_i$ the position vector for the ith node. As mentioned before, this expression results from the calculation of the fluctuations in the density of nodes :

$$\begin{aligned} DSF_L(\omega,\mathbf{q}) &\propto \int \exp(-i\omega t)\left\langle(\rho(\mathbf{q},t)-\rho_{\mathbf{q}}).(\rho(-\mathbf{q},t)-\rho_{-\mathbf{q}})\right\rangle dt \\ &\approx \int \exp(-i\omega t)\sum_{ij}(\mathbf{q}.\mathbf{u}_i)(\mathbf{q}.\mathbf{u}_j)\exp\left(i\mathbf{q}.\left(\mathbf{N}_i-\mathbf{N}_j\right)\right)dt \end{aligned}$$

due to

$$\begin{aligned} \rho(\mathbf{q},t)-\rho_{\mathbf{q}} &= \int\rho(\mathbf{r},t)\exp(i\mathbf{q}.\mathbf{r})d\mathbf{r}-\int\rho(\mathbf{R},0)\exp(i\mathbf{q}.\mathbf{R})d\mathbf{R} \\ &= \sum_{i=1}^{N}\exp\left(i\mathbf{q}.\left(\mathbf{N}_i+\mathbf{u}_i(t)\right)\right)-\exp\left(i\mathbf{q}.\mathbf{N}_i\right)\approx\sum_{i=1}^{N}i\mathbf{q}.\mathbf{u}_i(t)\exp\left(i\mathbf{q}.\mathbf{N}_i\right) \end{aligned} \tag{2.21}$$

where $\mathbf{u}_i(t)$ is the displacement supported by the node i in a random excitation, that is next decomposed on the eigenmodes with frequencies ω_j [**?**]. $DSF_L(\omega,\mathbf{q})$ thus corresponds to the Fourier transform of the longitudinal components of the waves with frequency ω. Its transverse counterpart is

$$DSF_T(\omega,\mathbf{q}) = \sum_{j=1}^{3N}(\sum_{i=1}^{N}\mathbf{q}_n\times\mathbf{u}_i(\omega_j)e^{\mathbf{q}.\mathbf{N}_i})^2\delta(\omega-\omega_j) \tag{2.22}$$

The KPM is used once again to calculate the DSFs without exact diagonalization. With this method, DSFs can directly be computed as :

$$DSF_L(\omega,\mathbf{q})) = \sum_{b=0}^{B}\gamma_b\upsilon_b^L(\mathbf{q})T_b(\varepsilon) \tag{2.23}$$

$$DSF_T(\omega,\mathbf{q}) = \sum_{b=0}^{B}\gamma_b\upsilon_b^T(\mathbf{q})T_b(\varepsilon) \tag{2.24}$$

with γ_b and ε as previously defined, and :

$$\upsilon_b^L(\mathbf{q}) = \overline{\frac{1}{N}(\sum_{i=1}^{N}\mathbf{q}_n.\mathbf{u}_i{}^0e^{\mathbf{q}.\mathbf{N}_i})^2(\sum_{i=1}^{N}\mathbf{q}_n.\mathbf{u}_i{}^be^{\mathbf{q}.\mathbf{N}_i})^2} \tag{2.25}$$

$$\upsilon_b^T(\mathbf{q}) = \overline{\frac{1}{N}(\sum_{i=1}^{N}\mathbf{q}_n\times\mathbf{u}_i^0e^{\mathbf{q}.\mathbf{N}_i})^2.(\sum_{i=1}^{N}\mathbf{q}_n\times\mathbf{u}_i^be^{\mathbf{q}.\mathbf{N}_i})^2}, \tag{2.26}$$

2.3.4 Voronoi Decomposition

The decomposition of the displacement on longitudinal and transverse components compared to the wavevector is ill-defined for non-crystalline samples such as the Penrose tilling [**?**]. The displacement decomposition used herein is based on the Voronoi cells volume variation and was already applied to amorphous glassy samples in [**?**]. The Voronoi cell built around a node is the area containing the points closer to this node than every others. The Transverse displacements will be the displacements not modifying the Voronoi cells' volume and the Longitudinal are the displacements doing so. As in [**?**], we use the A matrix describing the relative volume variation of the voronoi cell centered on node i, due to the displacement d_j of node j (translation u_x, u_y and rotation θ) :

$$A_{i,j} = \frac{1}{V_i}\frac{\partial V_i}{\partial d_j} \tag{2.27}$$

This matrix can be easily obtained from the mesh of beam elements, the detailed method being described in [**?**]. With this definition we obtain the longitudinal and transverse components by :

$$\begin{aligned} \mathbf{d}_\eta &= \mathbf{P}_\eta d \ ; \ \eta = L, T \\ \mathbf{P}_L &= \mathbf{A}^t(\mathbf{A}\mathbf{A}^t)^{-1}\mathbf{A} \\ \mathbf{P}_T &= \mathbf{I} - \mathbf{A}^t(\mathbf{A}\mathbf{A}^t)^{-1}\mathbf{A} \end{aligned} \tag{2.28}$$

This new decomposition is then injected in the VDOS and the DSF calculation. The contribution to the VDOS of the Tchebychev moment (Eq. 2.17) for example, becomes :

$$\mu_b^\eta = \overline{\langle \mathbf{d}_0^r | \mathbf{P}_\eta | \mathbf{d}_b^r \rangle} \tag{2.29}$$

with $\eta = L$ or $\eta = T$ for its respective longitudinal and transverse contributions to the VDOS.

2.4 Role of bending in periodic beam lattices

As a first example, the vibration of a periodic beam lattice is analyzed. The effect of the bending stiffness that is the only design parameter to be adjusted once the geometry of the lattice is fixed, is investigated. The ratio between the tensile stiffness and the bending stiffness is varied in order to observe the influence of the latter on the vibrational response. The idea behind such a study is that increasing local bending stiffness should enhance the energy separation between local rotational and compressional modes, and thus enlarges possible band gaps (see *e.g.* [**?**]).

2.4.1 Analytical solution for a periodic lattice

A infinite periodic lattice with a simple squared elementary pattern is considered (see Figure 2.1). As for wave propagation [**?**], the periodic structure of this lattice allows the

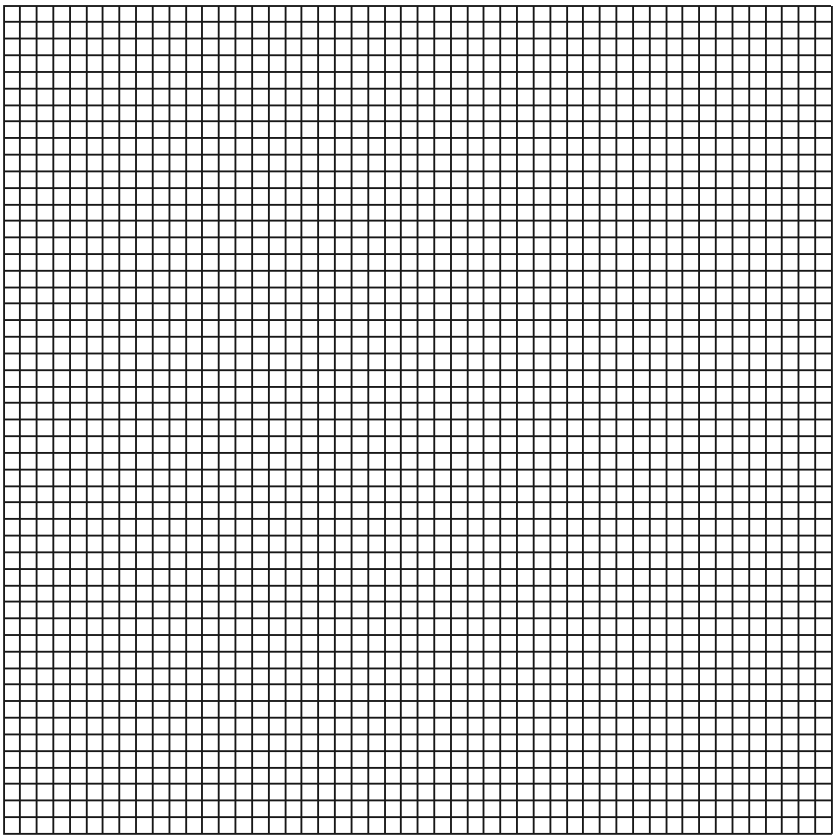

FIGURE 2.1 – 50 by 50 square beam lattice.

use of periodic boundary conditions to reduce the analysis to one elementary cell. Using those conditions and choosing the solutions of Equation (2.3) as :

$$\mathbf{d} = \mathbf{a}_d exp(i(\omega t + \mathbf{q}.\mathbf{r})), \tag{2.30}$$

equation 2.3 is solved analytically. This calculation is detailled in A. The values [ω,**q**] that verify $det(([K] - \omega^2 [M])) = 0$ are calculated using the *MAPLE* software.

Figures 2.2-a-b-c show the resulting analytical solution of the dispersion law (DSF) for three ratios $\frac{K_v}{K_u}$, namely 0.01, 0.5 and 2. For graphical representation, the dimensionless pulsation ω^{adim} defined as $\omega^{adim} = \omega.\sqrt{\frac{m}{K_u}}$, is used.

For the three cases analyzed herein, three surfaces (ω^{adim} as a function of q_x, q_y) are plotted : two acoustic solutions (in phase vibrations of the nodes : blue and red) and one optical (out of phase vibrations of the nodes : green). For $\frac{K_v}{K_u} = 0.01$ and $\frac{K_v}{K_u} = 0.5$, the green and red surfaces merge at $(\frac{\pi}{L}, \frac{\pi}{L})$ whereas for $\frac{K_v}{K_u} = 2$ the two surfaces are disconnected. This creates a frequency range in which no mode exists. This is called a band gap. It can be shown that the analytical solution used above degenerates for (q_x, q_y) reaching

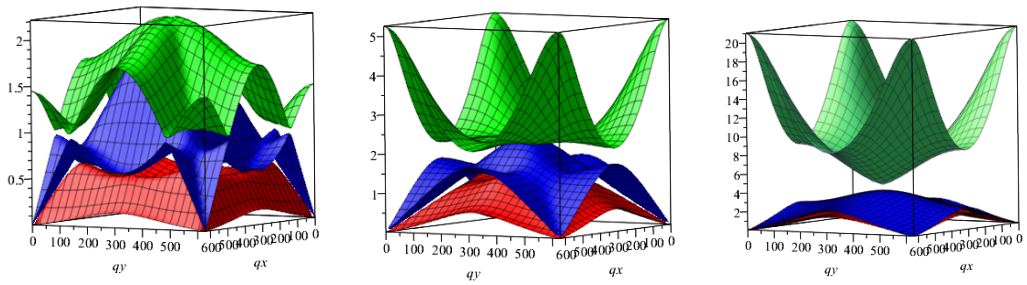

(a) (b) (c)

FIGURE 2.2 – Analytical dispersion relation $\omega_{adim}(q_x, q_y)$ for an infinite Square lattice for (a) $\frac{K_v}{K_u} = 0.01$ (b) $\frac{K_v}{K_u} = 0.5$ (c) $\frac{K_v}{K_u} = 2$.

$(\frac{\pi}{L}, \frac{\pi}{L})$ giving a double solution and a single one :

$$\{\sqrt{\frac{210(K_v + K_u)}{43m}}, \sqrt{\frac{10K_v}{m}}\} \tag{2.31}$$

Using the expression of those solutions, the size of the band gap depending on $\frac{K_v}{K_u}$ is :

$$\Delta\omega^{adim} = \sqrt{\frac{m}{Ku}}\left(\sqrt{\frac{10K_v}{m}} - \sqrt{\frac{210(K_v + K_u)}{43m}}\right)^{+} \tag{2.32}$$

It is obtained that below a given ratio $\frac{K_v}{K_u}$, no band gap is obtained whereas above a critical value of 0.9545, the size of the band gap increases as $\sqrt{\frac{K_v}{K_u}}$ as illustrated in Figure 2.3.

As shown in Figures 2.2-b and 2.2-c, the high-frequency modes in the periodic beam lattice are mainly transverse. Increasing K_v independently of K_u thus raises mainly the frequency of optical transverse modes (upper band in the dispersion relation), creating a band gap. Note that $\frac{Kv}{Ku}$ ratio higher than 0.05 (slenderness approximately lower than 5) can't be geometrically obtained for square section beams while respecting the slenderness requirements for the Euler-Bernoulli beam model, thus making impossible to obtain band gaps for these specific stiffness values. It may however be possible to create a band gap by adjusting the mass distribution of the beams or just with a different periodic structure. The goal of this article is indeed to show evidence of tendencies that could be even amplified with a more accurate description of the interactions beyond the Euler-Bernouilli approximation, and to adapt new tools to the study of the vibrations in non-periodic beam structures. The three typical ratios of $K_v/K_u = 0.01, 0.5$ and 2 will thus be kept all-along the article for comparison purposes.

2.4.2 Numerical calculations

To further analyze the vibrational behaviour of the square lattice, the PR and VDOS have been computed from a numerical solution obtained for a 5×5 to 50×50 cells lattice

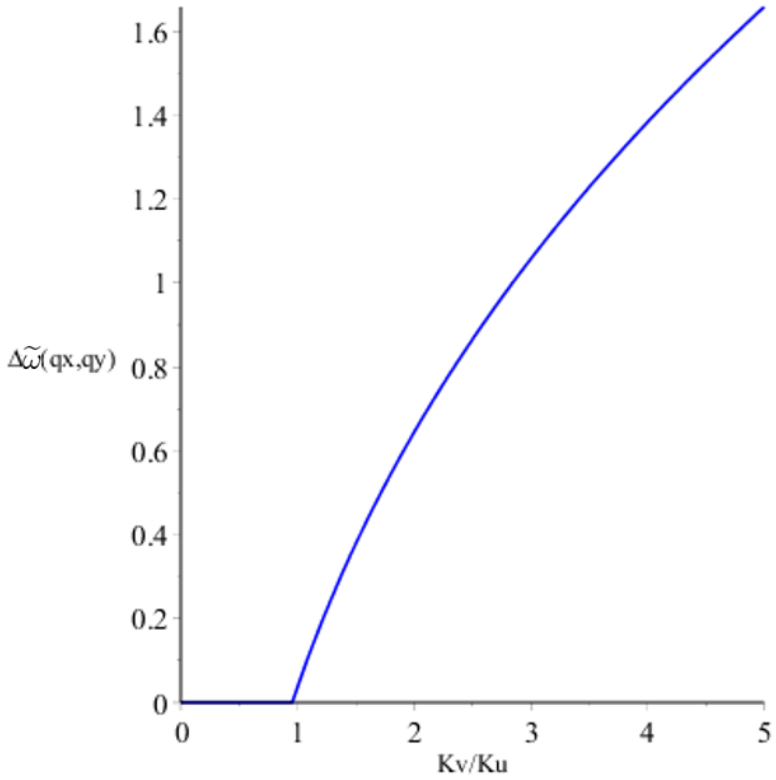

FIGURE 2.3 – Analytical band gap for an infinite square lattice in function of $\frac{K_v}{K_u}$.

as presented in Figure 2.1. For the 50×50 lattice, the system has $N = 2601$ nodes for $3N(= 7803)$ DFs, including the boundary. Periodic boundary conditions are applied along the boundary of the analyzed domain. For these simulations, the parameters used were $L = 0.01$ m, $K_u = 3.5 \times 10^5$ kg.s^{-2} , $\rho = 1000$ kg.m^{-3}, $E = 1.4 \times 10^9$ Pa, $K_v = 2K_u$, $K_v = 0.5K_u$ and $K_v = 0.01K_u$.

For the three values of $\frac{K_v}{K_u}$, the VDOS and PR are computed following the methodology detailed above. The results are plotted in Figure 2.4 to check the influence of finite size effects, and in Figures 2.5, 2.6 and 2.7 for different values of K_v/K_u . In the latter, *i.e.* for $\frac{K_v}{K_u} = 2$, the creation of the band gap is clearly observed in the VDOS and in the PR. Indeed, for around $\omega^{adim} \approx 4$ that corresponds to our analytical value of ω^{adim} in the band gap, the VDOS vanishes and there is no defined value for the PR as no vibration mode exists for ω^{adim} within the band gap. Conversely, for $\frac{K_v}{K_u} = 0.5$ and $\frac{K_v}{K_u} = 0.01$, the VDOS does not vanish and there is no zone with undefined PR. However, for all three cases, the fluctuations of the VDOS are in close relation with the analytically obtained shape of the surfaces giving the three different roots ω^{adim} as plotted in Figures 2.2-a-b-c. Concerning the PR, most of the modes have a PR around 0.6 due to the fact that it is the PR of a spatial cosine to which all the nodes participate. This example shows how the VDOS and the PR can be used to interpret the vibrational behavior of the material and to detect

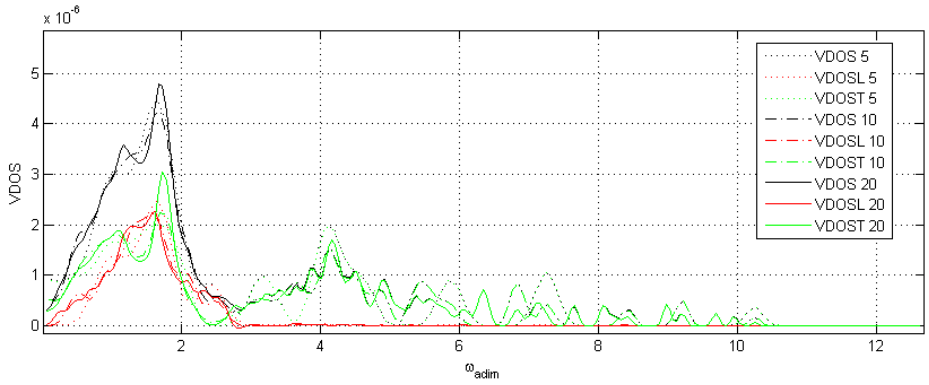

FIGURE 2.4 – VDOS for the 5×5, 10×10 and 20×20 square lattice with $\frac{K_v}{K_u} = 0.5$.

band gaps. As expected, it shows as well, that the additional flexural stiffness in the beam lattice model induces a new kind of high frequency optical modes, with mainly transverse character and with the related aperture of a band gap increasing with K_v in the vibrational response.

2.5 Quasi-periodic beam lattice

The methodology is now applied to analyze the behaviour of a quasi-periodic beam lattice. The complexity of quasi-periodic structures does not allow the calculation of analytical solutions as was done previously. Only numerical results are obtained. All the calculations are run on the 4^{th} approximant of a Penrose lattice shown on Figure.1.3. The system has $N = 8257$ nodes and $3N(= 24771)$ DFs. As previously, periodic boundary conditions are prescribed. The parameters of the model are the same as previously : $L = 0.01$ m, $K_u = 3.5 \times 10^5$ kg.s^{-2} , $\rho = 1000$ kg.m^{-3}, $E = 1.4 \times 10^9$ Pa. To understand the influence of the flexural component of the beam stiffness, the same three values of $\frac{K_v}{K_u}$ are still considered : 0.01, 0.5 and 2.

For the three values of $\frac{K_v}{K_u}$, the VDOS and PR are shown in Figures 2.8, 2.9 and 2.10. The VDOS of the quasi-periodic tilling considered in this section, share some similarities with the ones computed for the periodic square lattice : for the three values of $\frac{K_v}{K_u}$, there is first a bump in the low frequency range related to the accoustic branches. After a decrease, the VDOS increases again which gives an indication concerning the existence of optical branches (high frequency out-of-phase vibrations of the nodes with low group velocity). Concerning the PR, whereas for the square lattice there is no clear trend in the evolution of the PR, the quasi-periodic tilling analyzed herein behaves differently. It is observed that the PR follows fluctuations that seem (quite surprisingly) opposite to those of the VDOS for $\frac{K_v}{K_u} = 0.5$ and $\frac{K_v}{K_u} = 2$, but similar for $\frac{K_v}{K_u} = 0.01$ except around $\omega_{adim} = 0.6$. In these cases, a drop of the PR relates to a peak in the VDOS. Consequently, in the frequency ranges with a high density of modes, the latters have the tendency to show

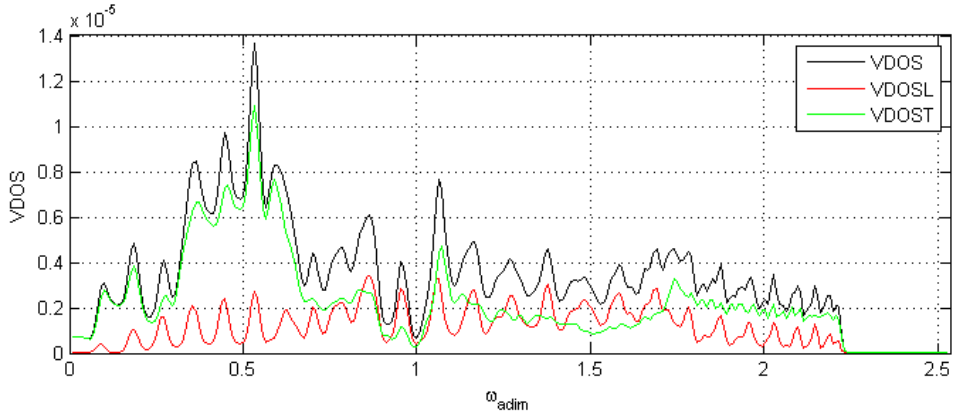

(a)

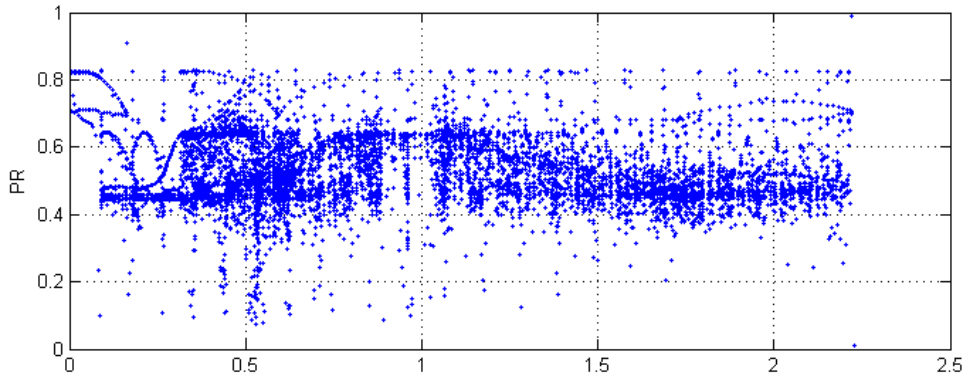

(b)

FIGURE 2.5 – (a) Complete, longitudinal and transverse VDOS and (b) PR for the 50×50 square lattice with $\frac{K_v}{K_u} = 0.01$.

localized patterns. Conversely, in the frequency ranges with a low density of modes, the latters show diffuse patterns : especially in the high frequency regime, quasi-crystalline structures do not give rise to localized modes, but more surprisingly to a $PR \approx 0.6$ close to that of extended plane waves. It can finally be noticed a higher concentration of modes around certain frequencies, notably in the high frequency range, which results in waviness of the VDOS. In order to apprehend how the Penrose lattice vibrates, it can be interesting to look at several modes on specific domain of the frequency range. Several modes are plotted for $\frac{K_v}{K_u} = 0.01$ (see Supplementary Material for all the modes).

Figures 2.11 and 2.12 show highly structured modes where the vibration is localized on a star shaped structure as in Figure 2.15. These modes, localized on *stars*, are involved repeatedly in the two regions where the PR decreases. These modes are localized on specific patterns of the lattice. Figure 2.14 shows that, in the second decaying region of the PR, another kind of localized modes appears as well : they involve a thin but extended

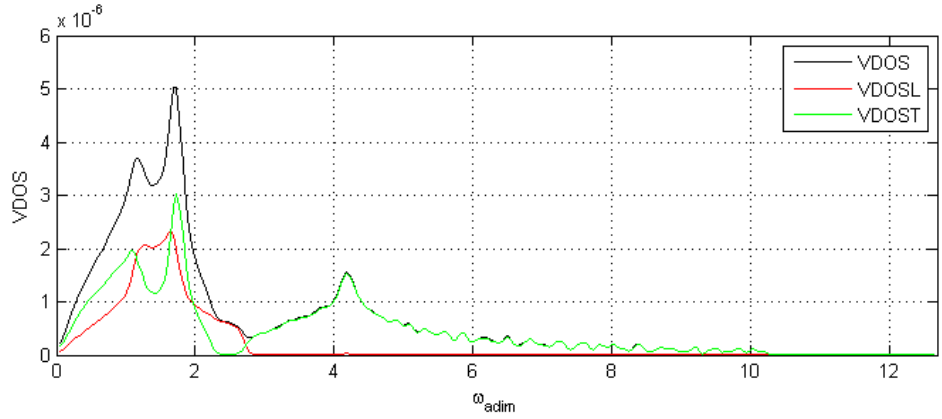

(a)

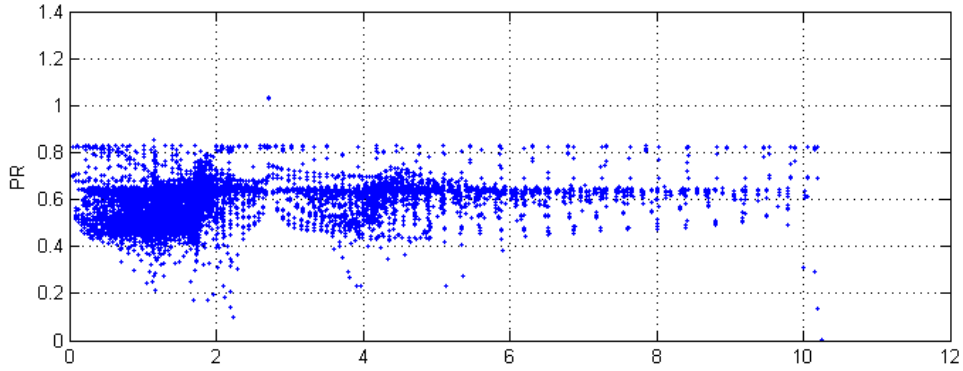

(b)

FIGURE 2.6 – (a) Complete, longitudinal and transverse VDOS and (b) PR for the 50×50 square lattice with $\frac{K_v}{K_u} = 0.5$.

crowned of vibrations. This kind of localization is very surprising and specific of quasi-crystals : it shows large scale vibrations in the high frequency regime. Finally, a complete set of structures with various sizes is excited along the modes and disordered patterns can also be found as in Figure 2.13 in a frenquency range where the PR is higher.

In order to test the hypothesis of isolated vibrations of specific patterns in the low frequency regime, that would be decorrelated from the overall environment, the *star* structure has been isolated and its own vibrational modes have been studied with fixed boundary conditions. In Figure 2.16 and 2.17 the VDOS of the *star* is superposed to the PR of the 4^{th} approximant for two ratios $\frac{K_v}{K_u}$. In both cases, the frequency range of the peak of the VDOS for the isolated star seems to correspond to the frequency for which this structure plays a predominant role. This might be the cause of the waviness of the VDOS : the vibrational modes concentrate around the frequencies that excite particular sub-structures. This response again is specific of quasi-crystals, since it shows evidences of the resonant

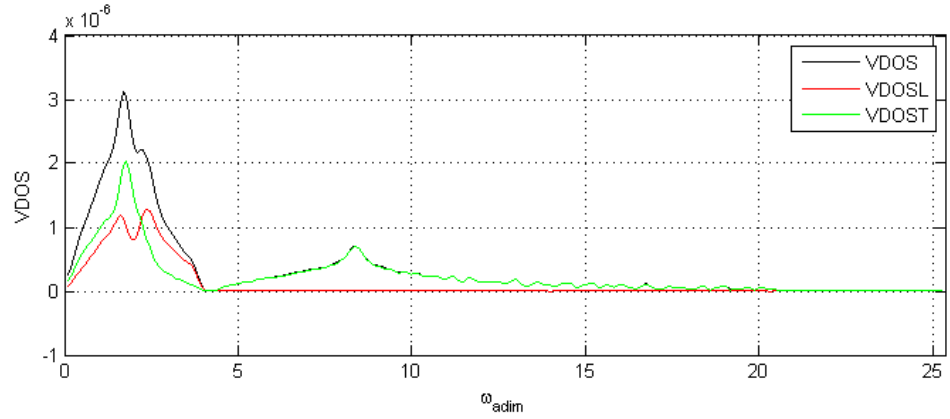

(a)

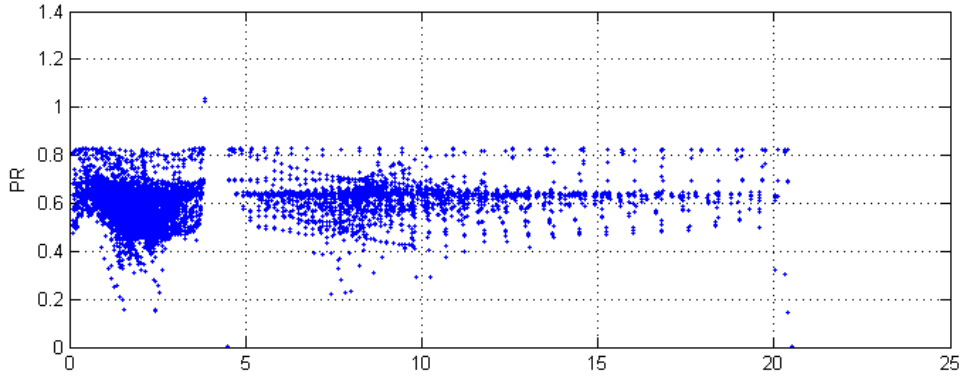

(b)

FIGURE 2.7 – (a) Complete, longitudinal and transverse VDOS and (b) PR for the 50×50 square lattice with $\frac{K_v}{K_u} = 2$.

vibrations of isolated structures, even in the low-frequency regime (isolated soft resonators). In this low-frequency range, extended vibrations are expected in crystals. These specific resonant vibrations however do not correlate with a band gap.

For $\frac{K_v}{K_u} = 2$, an additional gap is observed in the VDOS Figure 2.10 meaning that increasing the bending stiffness strongly impacts the vibrational behavior of the quasi-periodic lattice, namely by creating additional band gaps. The evolution of those gaps is also observed thanks to the DSF shown in Figures 2.18 and 2.19. The maxima of DSF intensity allow a quick visualization of the dispersion law, but in the case of a quasi-crystal, a given frequency w does not correspond to a single wave-vector q. Those figures exhibit classical dispersion relations for quasi-periodic structure as it can be found in [**?**, **?**, **?**] for 1D or 2D quasi-periodic lattices. We can observe for example pseudo Bernoulli zones overlapping and repeating at quasi-periodic periods. But an additional gap is visible in Fig. 2.19 for $K_v/K_u = 2$, as can be seen from the extinction of the DSF close to $\omega \approx$

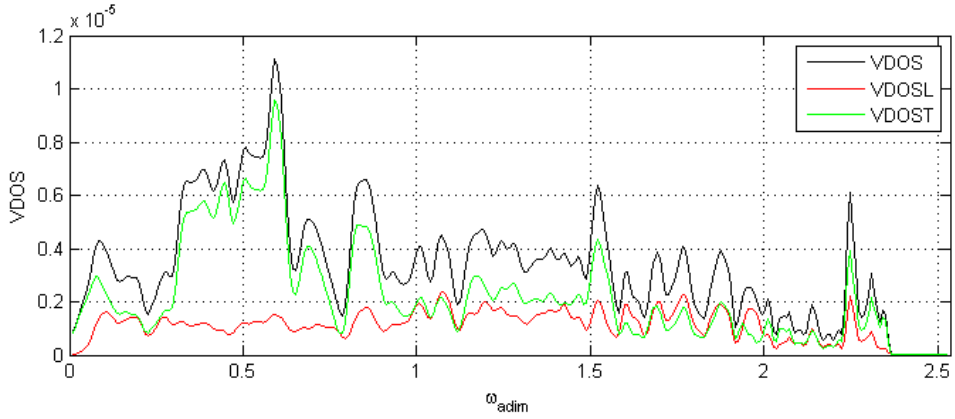

(a)

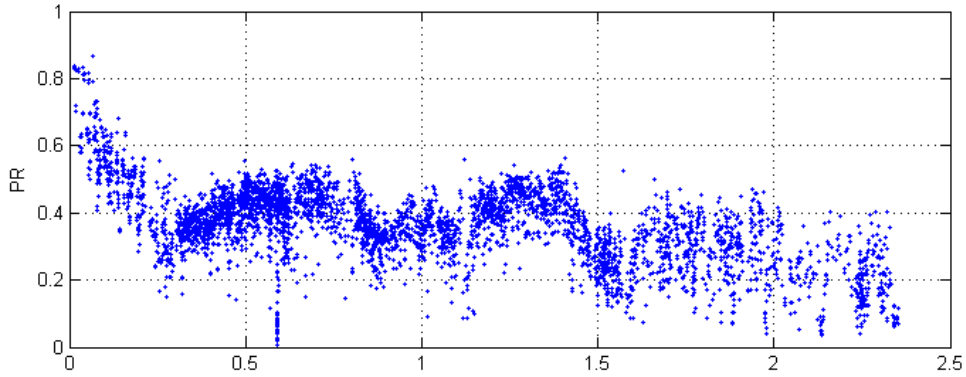

(b)

FIGURE 2.8 – (a) Complete, longitudinal and transverse VDOS and (b) PR for the 4th approximant of Penrose lattice with $\frac{K_v}{K_u} = 0.01$.

4. This large gap is visible in the dispersion law shown in Figure 2.19 especially for longitudinal modes.

2.6 Conclusion

The vibrational properties of periodic and quasi-periodic beam lattices were studied in this paper, as a function of the ratio between bending and tensile stiffness of the beams. The Vibrational Density of States, Participation Ratio and Dynamical Structure Factors for longitudinal as well as for transverse waves have been investigated for different ratios of bending over tensile stiffness. This ratio appears to be a driving parameter for large band gaps to occur and is related to an enhanced separation between in-phase tensile modes and out-of-phase bending vibrations. It is interesting to note that, contrary to the

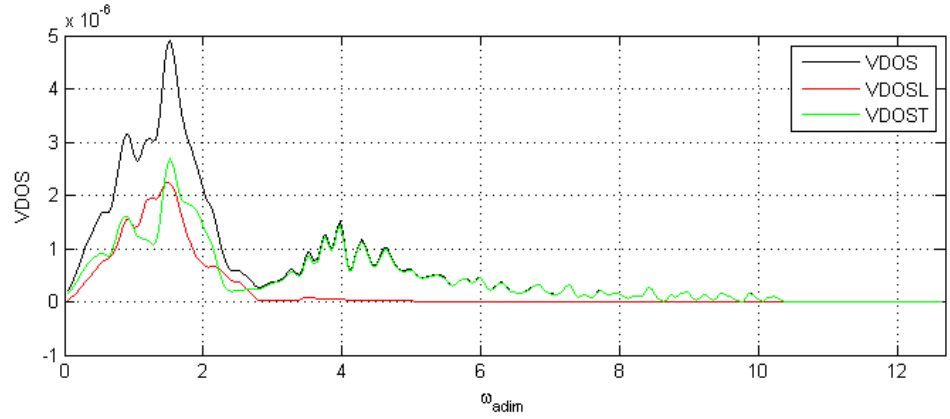

(a)

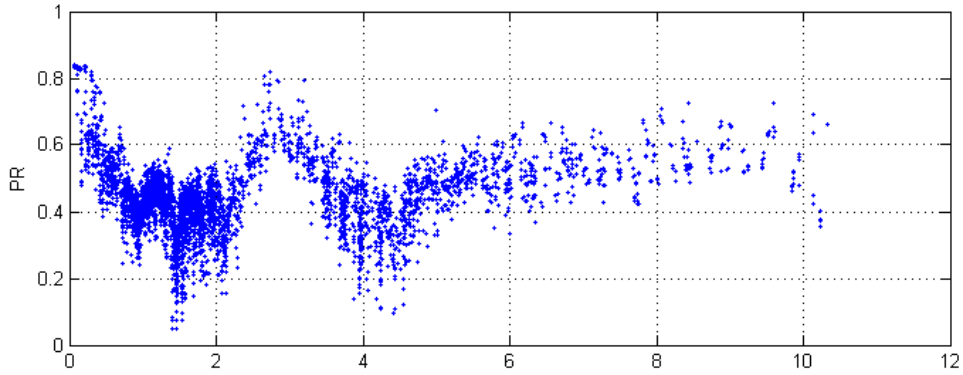

(b)

FIGURE 2.9 – (a) Complete, lngitudinal and transverse VDOS and (b) PR for the 4th approximant of Penrose lattice with $\frac{K_v}{K_u} = 0.5$.

periodic lattice which has anisotropic effective behavior for elasticity and for wave propagation, the Penrose beam structure, that has a higher level of material symmetry, is an apparent isotropic metamaterial. The creation of band gaps in the numerical simulations is the manifestation of a structural intrinsic property scaling with K_v/K_u. Then even if the band gaps are only reached here with unrealistic geometries in terms of beam slenderness assuming square cross section, it might be possible to obtain band gaps by adjusting other parameters of the structure (mass distribution, viscosity, etc) chosen with the same goal of frequency separation between in-phase tensile and out-of-phase bending modes. Finally, the position of the gap scales with $\sqrt{K_u/m} = \sqrt{E/\rho L^2}$ that depends on the size as well as on the material properties of the elementary beams.

Some low-frequency modes of the quasi-periodic lattice seems to be controlled by sub-structures of the lattice : indeed, the frequencies of these modes in the quasi-crystal correspond exactly to the frequency of the isolated local structure that appears repeatedly

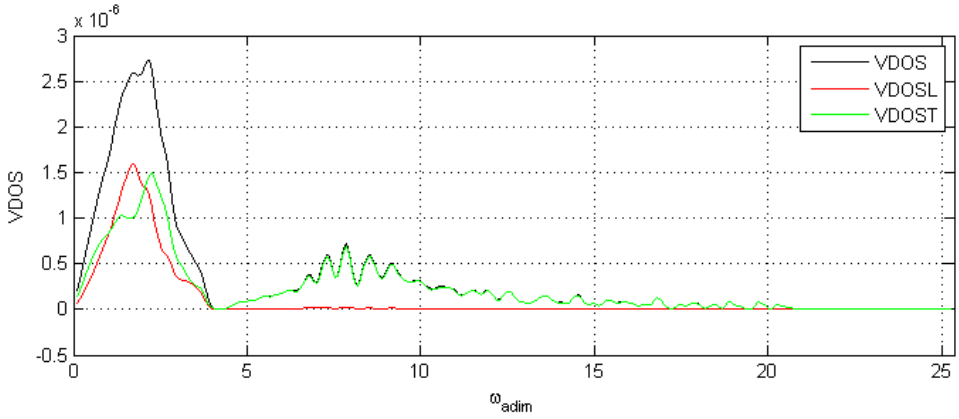

(a)

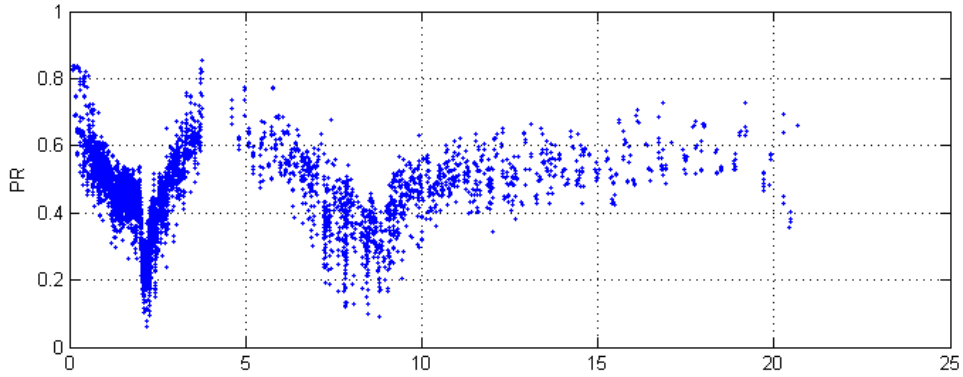

(b)

FIGURE 2.10 – (a) Complete, longitudinal and transverse VDOS and (b) PR for the 4th approximant of Penrose lattice with $\frac{K_v}{K_u} = 2$.

in the vibration modes. Conversely, high-frequency localized modes in the quasi-crystal involve large scale linear structures, suggesting the possibility to isolate large-scale and highly symmetric connected paths in the quasy-cristal. These resonant isolated structures are not sufficient to induce additional band gaps. A way to select the vibration modes by the type of structure they excite, eventually by reinfocing locally specific structures with additional masses, could allow revealing new patterns in PR, VDOS or DSF. For instance, it could be interesting to study more accurately and systematically the non-trivial hierarchy of sizes of the excited structures depending on the frequency of the modes they appear in, since it could have additional consequences as well on the transportation of wave packets with different wavelengths, and thus on acoustic signal processing.

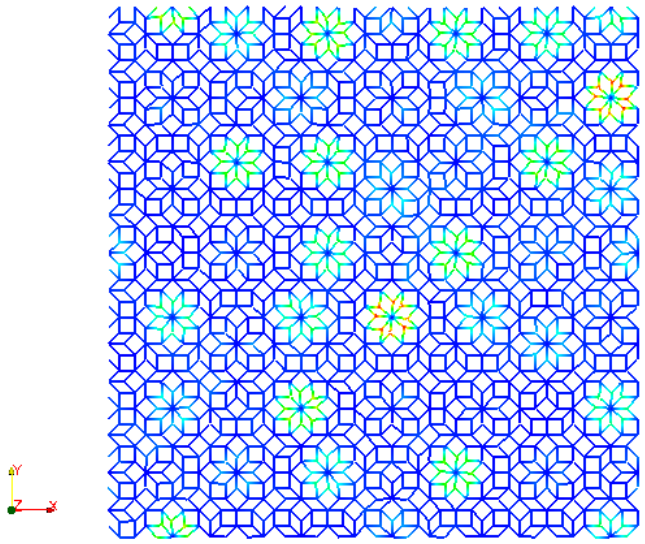

(a)

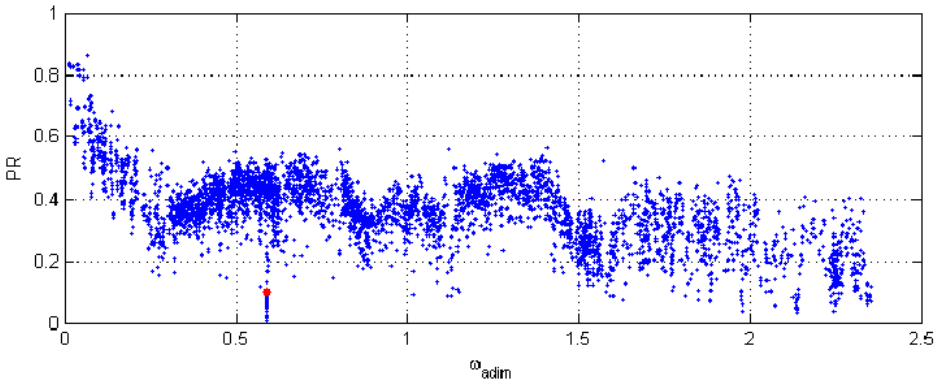

(b)

FIGURE 2.11 – (a) Deformed lattice and (b) PR (full PR in blue, corresponding mode in red) of the 1387^{th} mode for the 4^{th} approximant of Penrose lattice with $\frac{K_v}{K_u} = 0.01$.

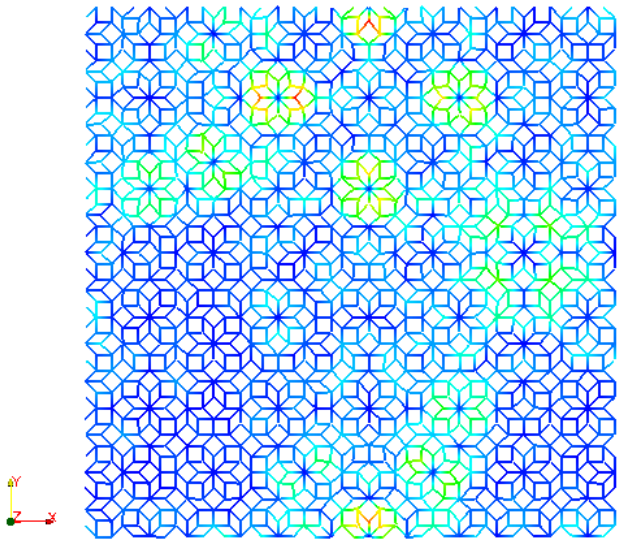

(a)

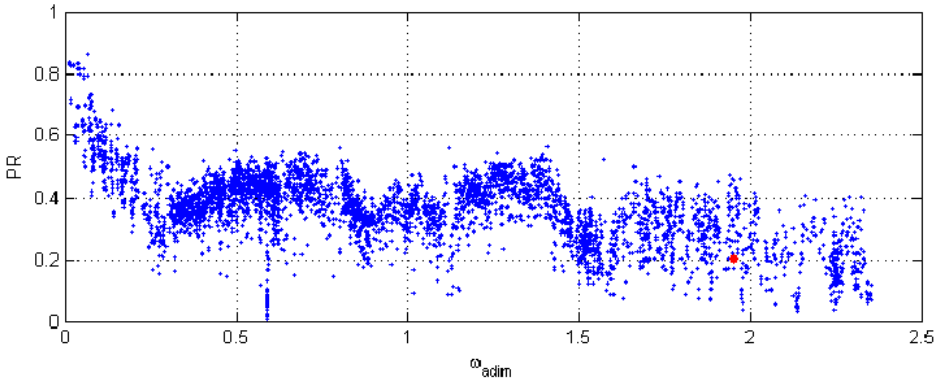

(b)

FIGURE 2.12 – (a) Deformed lattice and (b) PR (full PR in blue, corresponding mode in red) of the 3836^{th} mode for the 4^{th} approximant of Penrose lattice with $\frac{K_v}{K_u} = 0.01$.

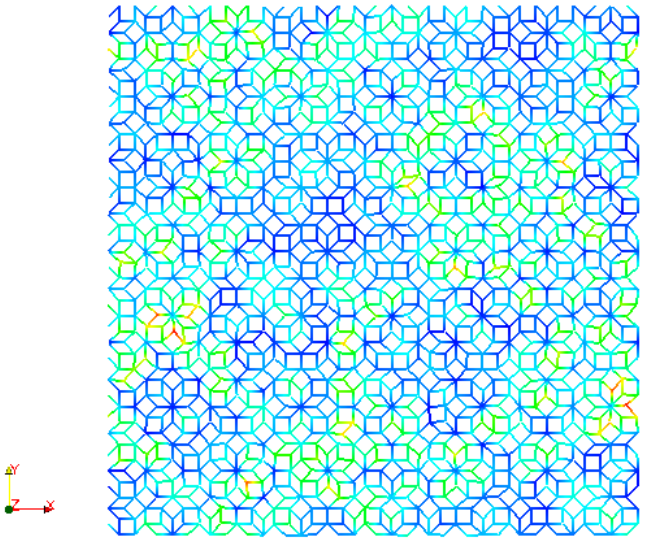

(a)

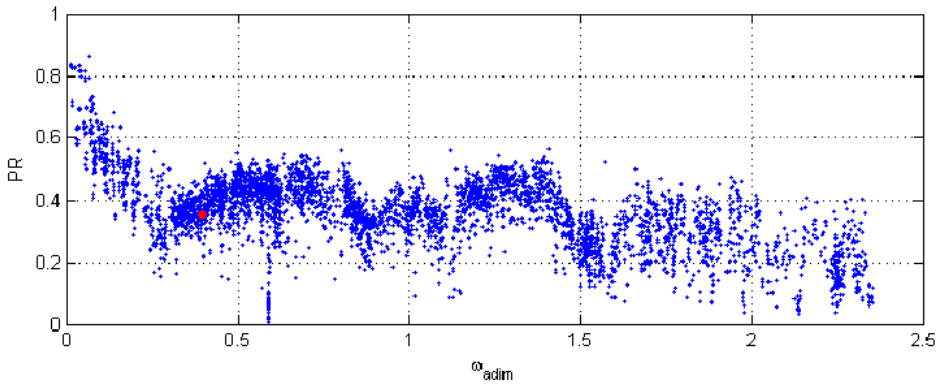

(b)

FIGURE 2.13 – (a) Deformed lattice and (b) PR (full PR in blue, corresponding mode in red) of the 693^{th} mode for the 4^{th} approximant of Penrose lattice with $\frac{K_v}{K_u} = 0.01$.

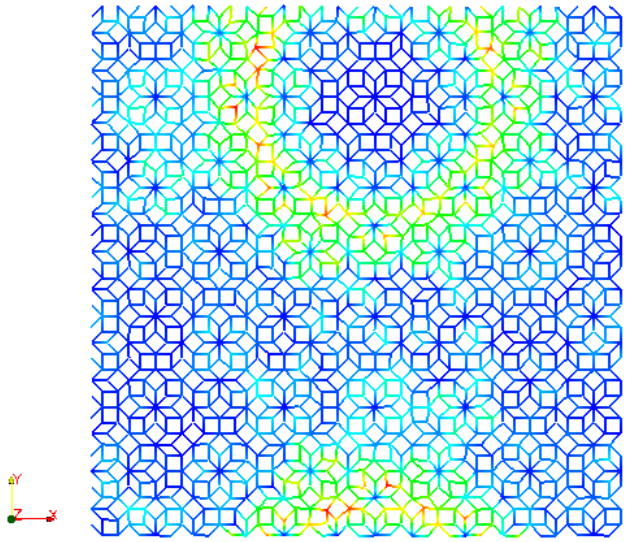

(a)

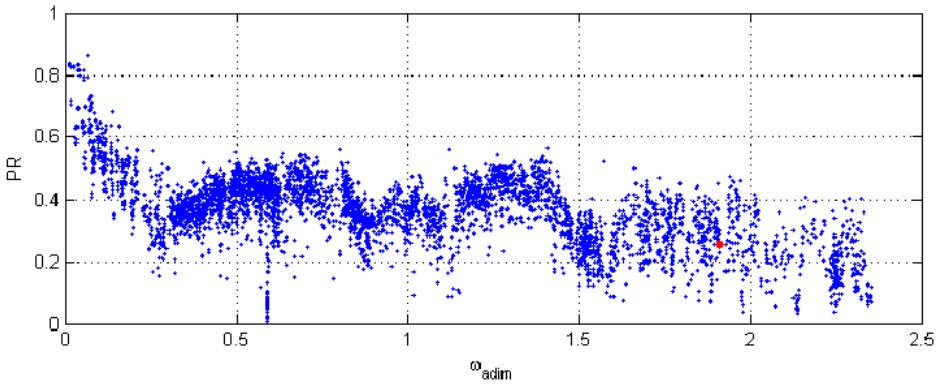

(b)

FIGURE 2.14 – (a) Deformed lattice and (b) PR (full PR in blue, corresponding mode in red) of the 3801^{th} mode for the 4^{th} approximant of Penrose lattice with $\frac{K_v}{K_u} = 0.01$.

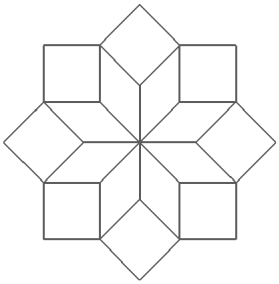

FIGURE 2.15 – Star structure.

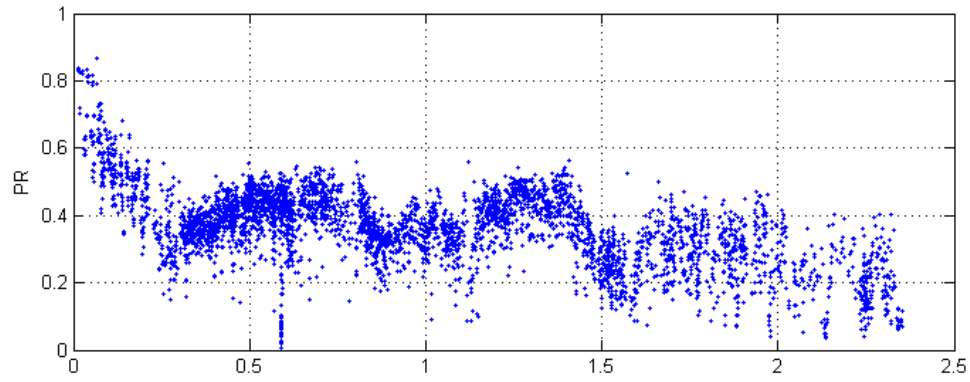

(a)

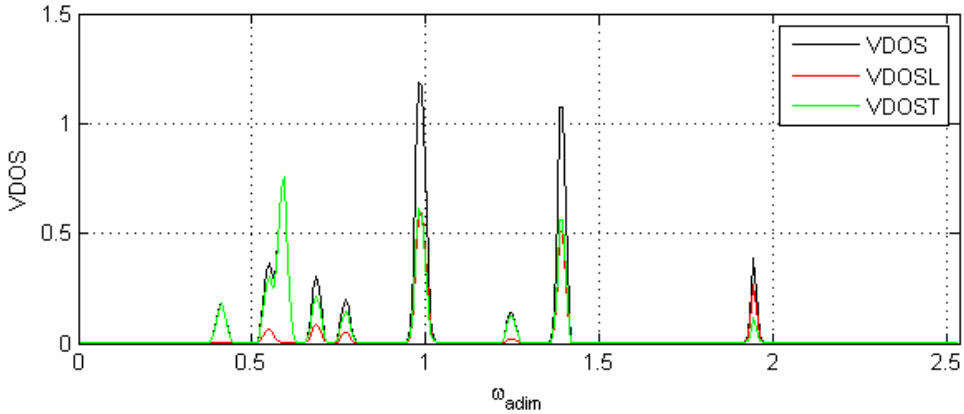

(b)

FIGURE 2.16 – (a) PR and (b) complete, longitudinal and transverse VDOS of the star for the 4^{th} approximant of Penrose lattice with $\frac{K_v}{K_u} = 0.01$.

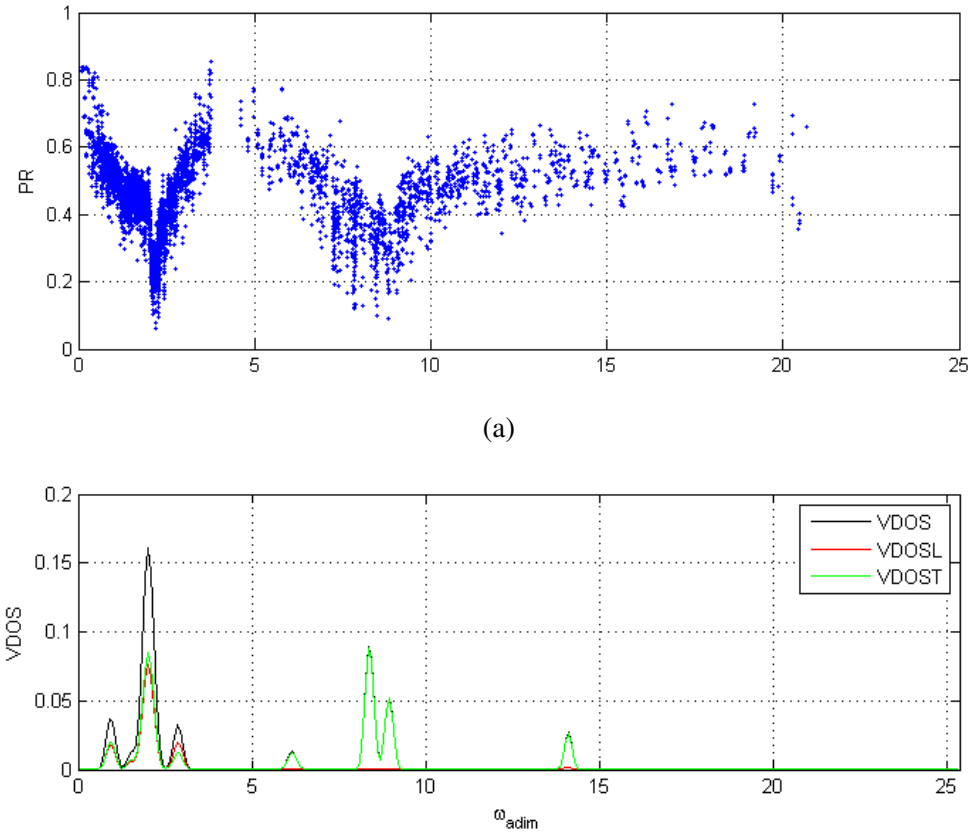

(a)

(b)

FIGURE 2.17 – (a) PR and (b) complete, longitudinal and transverse VDOS of the star for the 4^{th} approximant of Penrose lattice with $\frac{K_v}{K_u} = 2$.

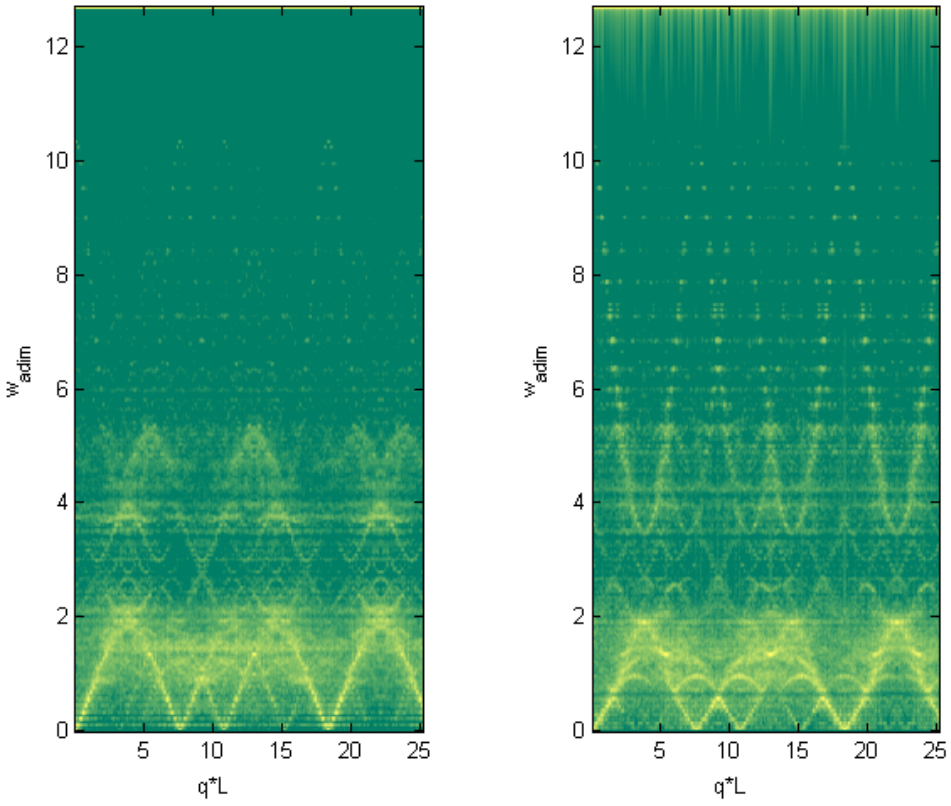

(a) (b)

FIGURE 2.18 – (a) Log of longitudinal DSF and (b) Log of transverse DSF for the 4^{th} approximant of Penrose lattice with $\frac{K_v}{K_u} = 0.5$.

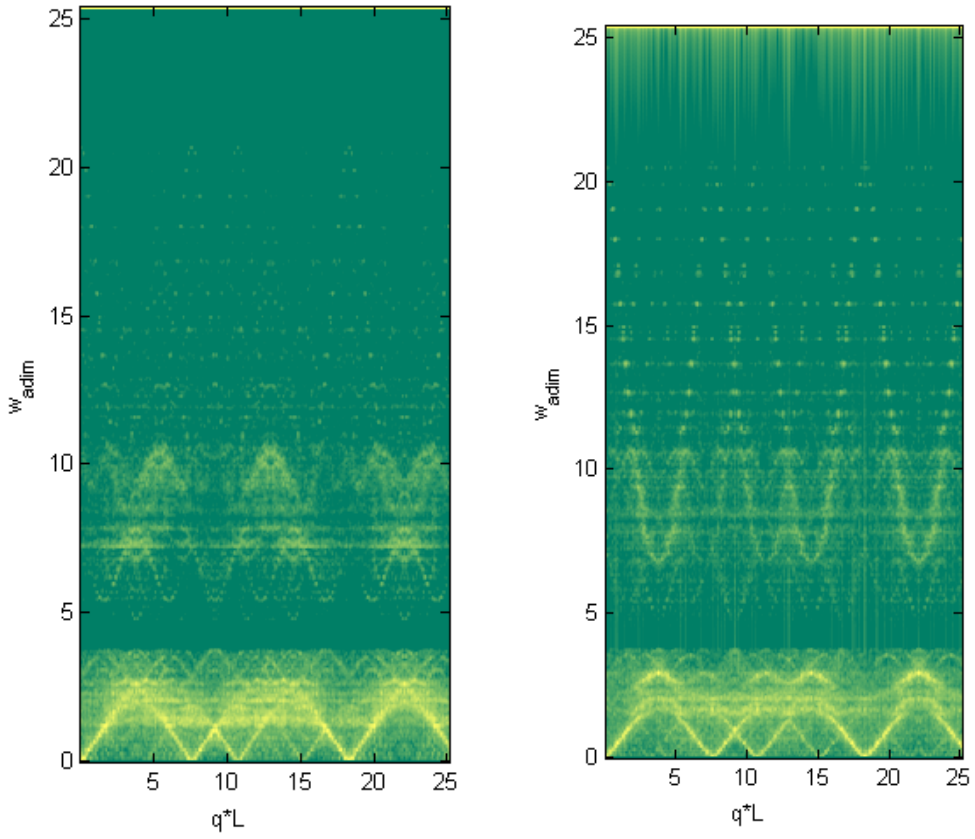

(a) (b)

FIGURE 2.19 – (a) Log of longitudinal DSF and (b) Log of transverse DSF for the 4^{th} approximant of Penrose lattice with $\frac{K_v}{K_u} = 2$.

Chapitre 3

Fracture

Contents

3.1 Introduction

In this chapter the fracture behavior of quasi-periodic beam lattices will be studied. Due to their peculiar symmetries allowed by their quasi-periodicity some quasi-periodic beam lattices might have a better resilience to crack propagation than periodic lattices due to the absence of weak plane. In order to test this assumption, numerical simulations will be performed. First in the quasi-static (QS) regime, the QS simulation will be validated on experiment performed on additive manufactured polymeric beam lattice. Then the ability of quasi-periodic lattices to dissipate energy by crack propagation will be compared to periodic lattice. Then the same system properties will be studied in the dynamical regime for crack propagation. Fpr that, new numerical simulation will be done. It will be shown that the slenderness of the beam plays a dominant role in the dissipation behavior of beam lattices.

3.2 Quasi-static Fracture

First a Quasi static model for crack propagation in beam lattices is used in order to study the failure behavior of periodic and quasi-periodic latices.

3.2.1 Model

The model used for Quasi static (QS) fracture simulation is the previously discussed FE Euler Bernoulli beam with the addition of a criterion on the brittle fracture of the beam. The criterion for beam failure is based on the element-average strain energy. It allows for weighting the contribution of tension force and bending moment with their actual energy contribution.The energy density of each beam can easily be calculated by :

$$\Phi = \frac{1}{AL}\mathbf{q_e}\mathbf{K}_e\mathbf{q_e} \tag{3.1}$$

Where L is the beam's length, A its cross section area, $\mathbf{q_e}$ the vector of DOFs and $\mathbf{K}_e$ the previously defined elementary stiffness matrix. The maximum value that can be sustained by a beam before it fails is a material parameter, namely Φ_r. Quasi-static simulations are performed and failure is accounted for using the following steps :

1. Elastic simulation of the lattice under a unit prescribed external load (load factor $\lambda = 1$)
2. detection of the beam i_{max} having the higher averaged strain energy Φ_{max}
3. the load factor is adjusted so that Φ_{max} equals Φ_r : $\lambda = \dfrac{\Phi_r}{\Phi_{max}}$
4. the amplitudes of the displacement and external loads computed in step 1 are scaled by λ
5. the results are saved and beam i_{max} is removed from the lattice

6. go to step 1 while the lattice can handle external loading ($\Phi_{max} > 0$)

This simple step by step model allows quick calculation of quasi-static fracture propagation through the lattice meta-material. It is assumed that the behavior of the beams is purely brittle and the global response is adjusted through the load factor in terms of applied displacement and force. In the case when the mechanical response of the specimen is not stable under monotonic loading, snap back (decreasing displacement and force) can be obtained. This is the main difference between the numerical simulations and the experiments in which this instability results in a dynamical response of the specimen (because the displacement can only increases, the specimen "jumps", with no control on the applied loading, from a stable configuration to the one having the closest but higher prescribed displacement). However, as there is no initial kinetic energy in the system, it is expected that dynamical effects have a very limited influence on the results. The algorithm proposed above to drive the simulation is thus a reliable approximation of the actual loading conditions applied to the specimen.

3.2.2 Quasi-static Fracture Simulation

In order to see the influence of the different parameters on the fracture propagation in the QP meta-material several simulations can be performed. The behavior of 2D lattice materials is investigated. Three types of lattices are selected :

1. quasi-periodic Kite & Dart Penrose tilling [**?**]
2. periodic approximate of the octogonal lattice [**?**]
3. periodic hexagonal lattice

Once the absolute size of a specimen is fixed, the remaining parameters to design such materials are : the *unit* cell size or beam length, the beam height and the constitutive material.

With the stiffness matrix previously defined one can noticed that the young modulus E can be factorize thus modifying the young modulus will linearly modify the problem, it will not lead to fundamentally different behavior. That is why the Young modulus will not be changed in the simulations. An important parameter as shown in the previous chapters is the slenderness of the beams. In the following simulation the influence of the slenderness on the energy dissipation by fracture propagation will be exhibited. All implementations are done under Matlab, and resulting meshes are viewed with Paraview.

3.2.2.1 Results

First the result of the QS simulation can be compared to experimental fracture profile. Experiments have been performed on samples obtained by additive manufacturing. They are made from photo-sensitive ABS-type polymer powder. The bulk material obtained from this process is isotropic. Its elastic behavior is defined by a Young's modulus of 1.4 GPa and a Poisson's ratio of 0.4. The sample design is the same as in [**?**] with a centered pre-crack oriented at 30^o with respect to the direction perpendicular to the loading

axis. The lattice structure is embedded by zones completely filled with the material. These zones are caught by the grips of the loading device to apply the remote displacement. The speed of the grips is 0.1 mm/min. This design allows for loading a central square part of 90 mm size with a classical tensile device under macroscopic uniaxial tension. Due to the crack angle of 30^o with respect to the loading axis, the crack tips are submitted to a mixed mode solicitation. The slenderness of beams is 6.7.

The samples are loaded until failure. Due to the high amount of elastic energy stored in the specimen, failure is unstable, meaning that once the first beam breaks the crack propagates dynamically and the sample completely fails.

To simulate the experiments, the two components of the displacement are fixed for all the nodes within a narrow band (its width being the average beam length) along the left edge. For the nodes within a narrow band along the right edge, the vertical displacement is fixed while the horizontal displacement is assigned a unit value that is adjusted in step 4. The rotation degrees of freedom are left free. The figure 3.1 shows the comparison between experimental result (on the left) with the QS simulation (on the right), the figure clearly shows a great agreement between experimental and QS simulation. Although this experiment is used to validate the QS fracture model the crack propagation is unstable which would require a dynamic simulation.

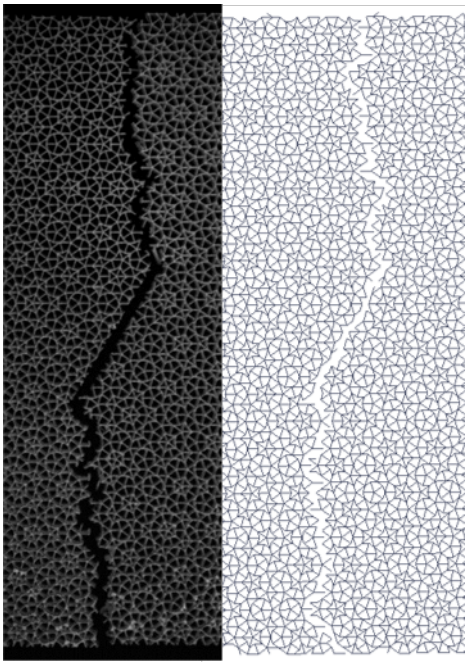

FIGURE 3.1 – Experimental and quasi-static simulation comparison

In the figure.3.2 the fracture profile for several slenderness is shown. It can be shown that the slender the beam, the wavier the crack path thus the more energy dissipation. One clearly observes interactions between the crack and the structure of the material. It seems that specific structures the lattice induce a deviation of the crack. This can be clearly seen in Fig. 3.2(b) where such structures have been circled in red.

They could be named extra-tough structure as this effect is obtained systematically. Moreover these substructures closely look like the ones identified in the vibrational response of the meta material. The deviation of the crack path induced by these specific features of the lattice makes the actual crack length longer than if the cracks were straight, resulting in a higher effective failure energy.

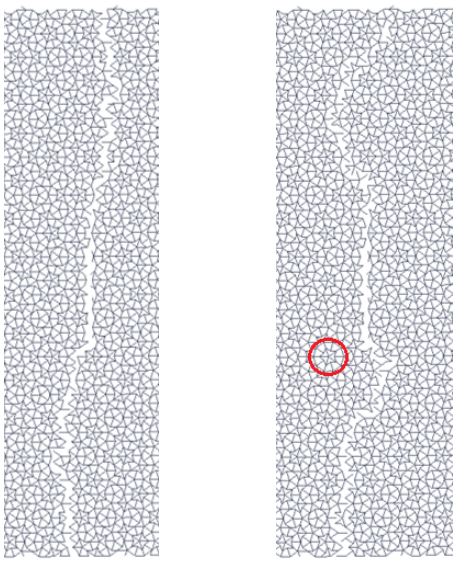

(a) (b)

FIGURE 3.2 – QS Fracture profil for a slenderness of 2.5(a) and 10(b)

From the simulations, not only the crack path is obtained but also the macroscopic response (force (F) *v.s* displacement (U)) that gives an insight in the effective behavior of the lattice. Using numerical simulations, it is also easy to perform a parametric study as function of the lattice parameters. The analysis is restricted herein to the beam slenderness. The influence of slenderness is analyzed in terms of crack path but also in terms of dissipated energy using the macroscopic force *v.s.* displacement response. The macroscopic response of specimens are normalized by the force and displacement at the onset of failure (F_o and $U(F_o)$). The results for the Kite & Dart Penrose lattice are illustrated in Fig. 3.3.

The response of the lattices is also compared to that obtained for a continuum material in the configuration tested above. It is clearly obtained that the response of the lattice deviates from that of a continuum showing the intrinsic ability of the quasi-periodic Penrose tilling to resist to defects. Further, it seems that increasing slenderness the lattice has the ability to dissipate more and more energy. For a quantitative analysis, twice the area covered by the normalized force*v.s.* displacement curves is computed. That corresponds to the ratio R between the dissipated energy and the stored energy before failure occurs. If the macroscopic response is purely brittle then $R = 1$. If $R < 1$ then the initial energy in the system is higher than what the material is able to dissipate, the macroscopic response is unstable and the remaining energy returns to the loading device. If $R > 1$ then the failure

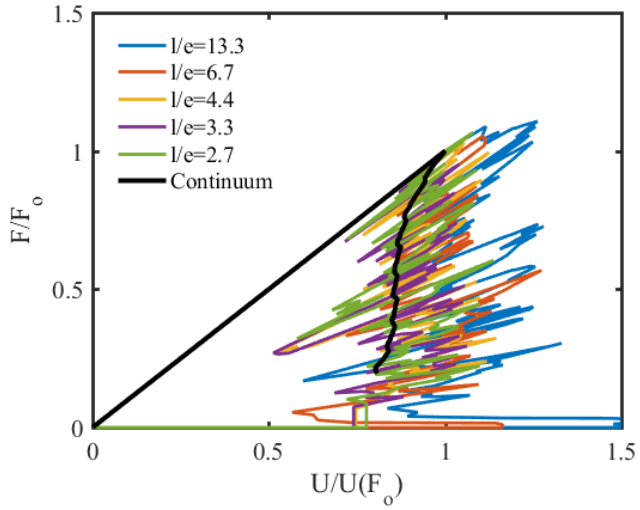

FIGURE 3.3 – Scaled load (F/F_o) *v.s.* displacement ($U/U(F_o)$) response of the Penrose tilling for different beam slenderness l/e.

process needs more energy than what was initially available in the system. The macroscopic response is thus stable and more energy is required to achieved complete failure. R is an indicator of the ability of the lattice to dissipate energy during failure.

The results are summarized in Figure.3.4 . It is confirmed that decreasing e increases the ability of the lattice to dissipate energy. Concerning the Kite & Dart Penrose tilling, for e=0.2 mm (l/e$\simeq$6.7), R is lower than 1 what confirms that the macroscopic response is unstable as in the corresponding experiment (shown in Fig.3.1). For this lattice, a comparison of the crack path for two values of e is given in Fig.3.2. When e is smaller the flexural stiffness of the beam is much lower than the tensile stiffness, thus allowing the beams to curve. This higher activation of the flexural deformation modes induces a rougher crack path, the crack being modified by locally tough patterns (highlighted in red in Figure.3.4) : instead of following the orientation prescribed by the macroscopic loading (as it is the case for e=0.5 mm, the crack follows the orientation having the lower failure energy in the vicinity of the crack tip. Due to these deviations of the crack, the effective crack length is higher and the energy intrinsically dissipated by the lattice is higher. For a comprehensive analysis, small insets are included in Figure.3.4 to show the repartition of the element average of the strain energy density for different lattices and slenderness. These results are obtained by loading the lattice under uniaxial tension without initial crack. For the hexagonal lattice, it is clear how increasing the slenderness leads to a transition between a tension dominated deformation mode to a bending dominated mode. For low slenderness, promoting tension modes, the beams aligned with the loading hold most of the strain energy density. Conversely, for higher slenderness, promoting flexural modes, most of the strain energy density is hold by beams not aligned with the loading. This transition is also evidenced for the octogonal lattice with well orga-

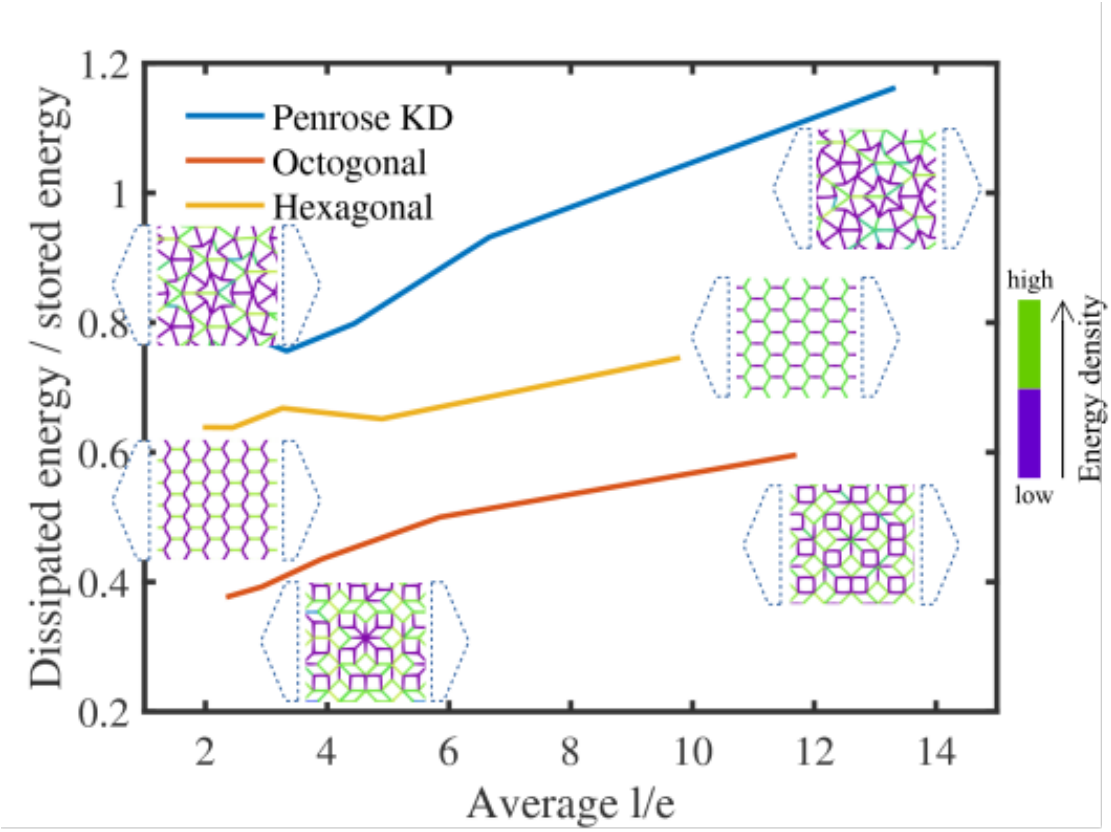

FIGURE 3.4 – Evolution of the dissipated energy normalized with the elastic energy stored at failure initiation for different lattices with varying beam slenderness. The distribution of the element average of the strain energy density for a uniaxial tensile test along the horizontal axis is illustrated from different lattices and slenderness. Green beams hold high energy density whereas purple beams have low energy density.

nized deforming structures whereas the Kite & Dart Penrose lattice produces disordered arrangements of the strain energy density. A remarkable dependence of R with respect to the average slenderness of the lattice is obtained in Fig. 3.4. In this Figure, the distribution of the element average of the strain energy density for uniaxial tension along the horizontal axis is plotted for different lattices and slenderness. Green beams hold high energy density whereas purple beams have low energy density. For example, it is clearly observed that for low slenderness, promoting tension modes, in the hexagonal lattice, the beams aligned with the loading hold most of the strain energy density. Conversely, for higher slenderness, promoting flexural modes, most of the strain energy density is hold by beam not aligned with the loading. It is obtained that hexagonal and octogonal lattices have well organized energy distribution patterns but that the Kite & Dart Penrose lattice produce disordered arrangement of the strain energy. Concerning the evolution of R as a function of the beams' slenderness, a linear trend is easily fitted on the curves plotted in

Fig. 3.4 for the three materials. It is obtained that the slope is 4 times higher for the Kite & Dart lattice than for the two others. One could argue that the structured deformation patterns (see Fig.3.4) obtained for the hexagonal and octogonal lattices are one reason for the lower increase of the energy dissipation capability of these lattices. Conversely, deformation patterns for the Kite & Dart Penrose lattice are disordered what is less favorable for the propagation of defects. The order of material symmetry is certainly at the origin of this difference between the Kite & Dart Penrose that has a 5-fold symmetry whereas the hexagonal and octogonal lattice have a 6-fold respectively 8-fold symmetry. Further, in the case of a periodic lattice, weak orientations exist [**?**], giving rise to directionality effects what intrinsically weaken this kind of architecture. As the octogonal lattice used herein is a periodic approximate of the quasi-periodic lattice, it may also be affected by the existence of weak orientations.

3.2.2.2 Conclusion and Discussion

It is concluded, from the previously seen results, that periodicity and high order symmetry affects the ability of a lattice to dissipate energy during the propagation of a crack. The higher performances of the Kite & Dart lattice, could be a consequence of disordered deformation patterns and of the activation of bending deformation modes when slenderness is increasing.

However, the study of unstable crack propagation with a quasi-static simulation does not ensure correct results. It is why a dynamic simulation is needed and will be presented in the following section.

3.3 Dynamical Problem

As previously discussed most of the cracks in the previous section are unstable propagation thus to better simulate the failure a dynamical simulation is required. The previous solution is not viable to calculate the dynamic propagation of fracture because it is not time dependent. A temporal scheme needs to be selected in order to solve temporal discretization of the FE dynamical problem.

3.3.1 Beam Breaking

At each time step the strain energy density of each beam is calculated. The beam is broken if, while having positive strain, the strain energy density of a beam exceeds the limit value (e_r) but still remain under $e_r.(1+\varepsilon_r)$, with ε_r a chosen maximum error to the breaking limit. In order to have the maximum energy density in the right range at the end of a time step a variable time step length is required and the way to achieve it will be explain in the next section. The broken beam is not fully removed from the calculation as it would lead to mass loss in the model. When the beam needs to be broken the node having the higher positive stress is selected and the links to other elements at this node

is removed. In practice this leads to the duplication of the node. All kinematic quantities from the previous node are transferred to the new one.

3.3.2 Temporal scheme

As the mesh is updated at the end of a step where a breaking occurs only one time step scheme can be used, thus a Newmark temporal scheme is used. In order to shorten the simulation time and to better capture the instant of the breaking a implicit variable time step scheme has been used.

$$\begin{aligned} q_{n+1} &= q_n + dt.\dot{q}_n + \tfrac{dt^2}{2}.\ddot{q}_n + \tfrac{dt^3}{6}(6\beta\frac{\ddot{q}_{n+1}-\ddot{q}_n}{dt}) \\ \dot{q}_{n+1} &= \dot{q}_n + dt.\ddot{q}_n + \tfrac{dt^2}{2}.(2\gamma\frac{\ddot{q}_{n+1}-\ddot{q}_n}{dt}) \end{aligned} \tag{3.2}$$

n being the index of the time step. In order to have a implicit temporal scheme, $\gamma = \frac{1}{2}$ and $\beta = \frac{1}{4}$. It have been shown that such a scheme is unconditionally stable and induces no numerical dissipation [**?**].

At the end of each time step the next time step size dt required to reach the maximum energy density is estimated assuming a linear evolution of the energy, then the new time step is calculated. If the maximum strain energy density is bellow e_r the procedure is repeated. If the maximum strain energy density exceeds $e_r.(1+\varepsilon_r)$, the time step is rejected and recalculated with a smaller dt, a linear evolution is once again assumed to estimate the new dt. If the maximum strain energy density is between e_r and $e_r.(1+\varepsilon_r)$ then the time step is valid and the element is broken. A upper limit dt_{up} is added when the strain energy is higher than a threshold $e_{threshold}$ in order to avoid too big time step. Indeed when the breaking limit is close to be reached a too big time step might lead to miss a break. The upper limit is not imposed before the energy threshold in order to limit simulation time especially for quasi static loadings. A lower time step limit dt_{low} is added to in order to avoid infinite decrease of the dt when overshooting the $e_r(1+\varepsilon_r)$. When the estimated new dt is smaller than the limit the time step is assumed valid even if the strain energy density exceed the allowed error.

In order to better comparatively visualize results of several simulations, the results meshes and quantities are exported as vtk format to be viewed in ParaView. The time step are not all exported in order to save disk space. The dt is sometimes adapted to allow exporting results at a fixed time step for better visualization of crack propagation.

The algorithm of the dynamic fracture simulation is summarized in the figure.3.5.

3.3.3 Dynamic Fracture Simulation

For the simulation the different parameters are :
$dt_{low} = 10^{-16}s$, $e_{threshold} = 0.95$, $\varepsilon_r = 0.05$. dt_{up} is set to a factor of dt_c, with dt_c being the critical value for an explicit temporal scheme :

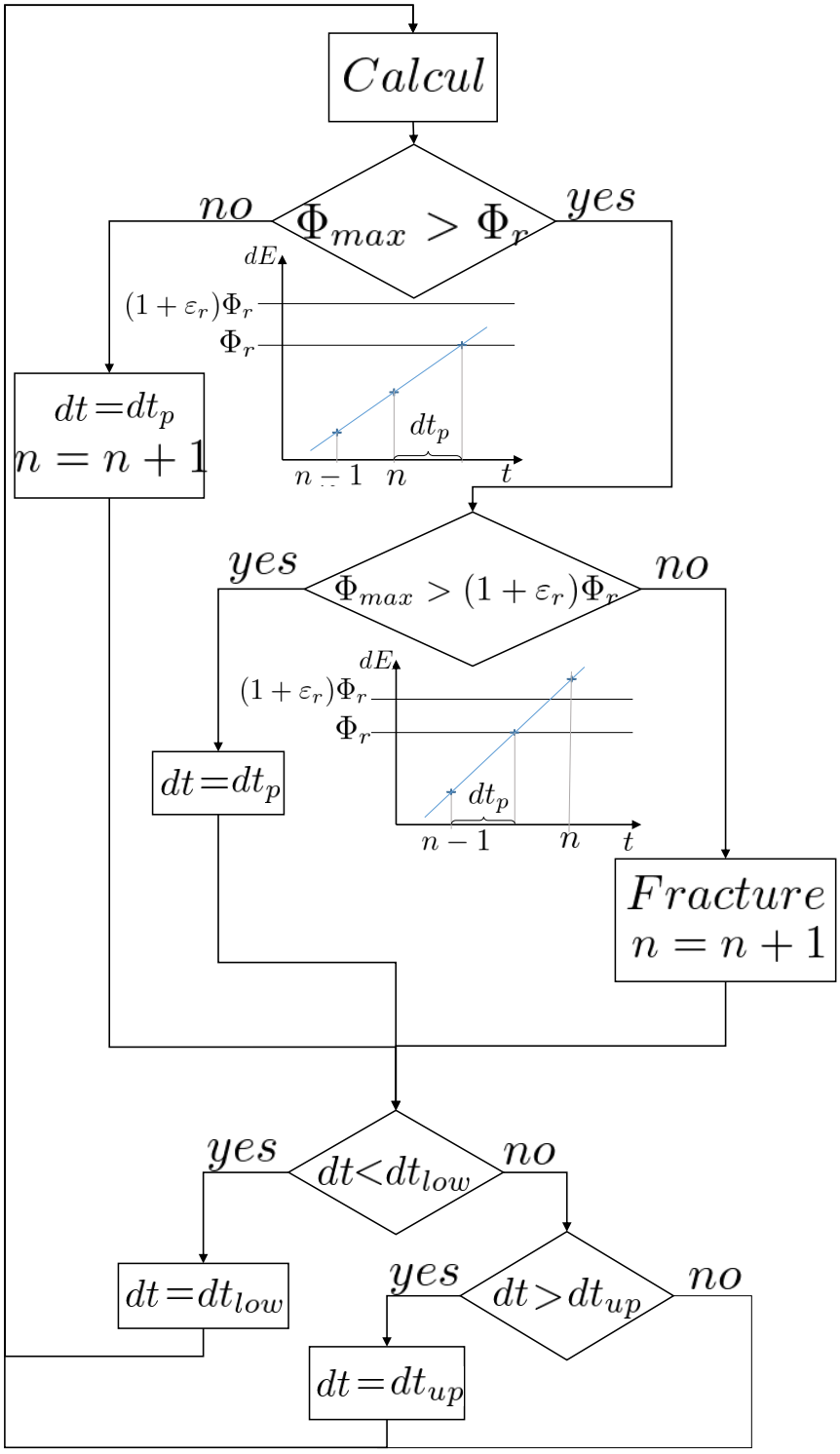

FIGURE 3.5 – Dynamic simulation algorithm

$dt_c = \frac{2}{max(\omega)}$ with ω the solutions of $det(\mathbf{K}_e - \omega^2 \mathbf{M}_e) = 0$

As previously all implementations are done with Matlab and resulting meshes are viewed with ParaView. Two sets of simulations will be discussed in the following. First dynamical simulation on the same sample as the one used in the previous quasi-static simulation where the boundary conditions are the same with an imposed speed $V = 0.1mm.min^{-1}$.
In order to study the cracking behavior of QP beam lattices under dynamic loading a set of dynamic crack opening simulations are performed. The sample is a square of side D with a pre-crack at the bottom of length l_a (as can be seen in figure.3.6). The boundary conditions are only applied on a narrow band at the lower right part to the sample (of width one beam length). A constant speed of $2.2m.s^{-1}$ is applied to the displacement dofs normal to the pre-crack in order to open it, while the other dofs are left free. This simulation should approximate an low-speed impact experiment where a bulk of material at the bottom right of the sample is hit by an impactor.

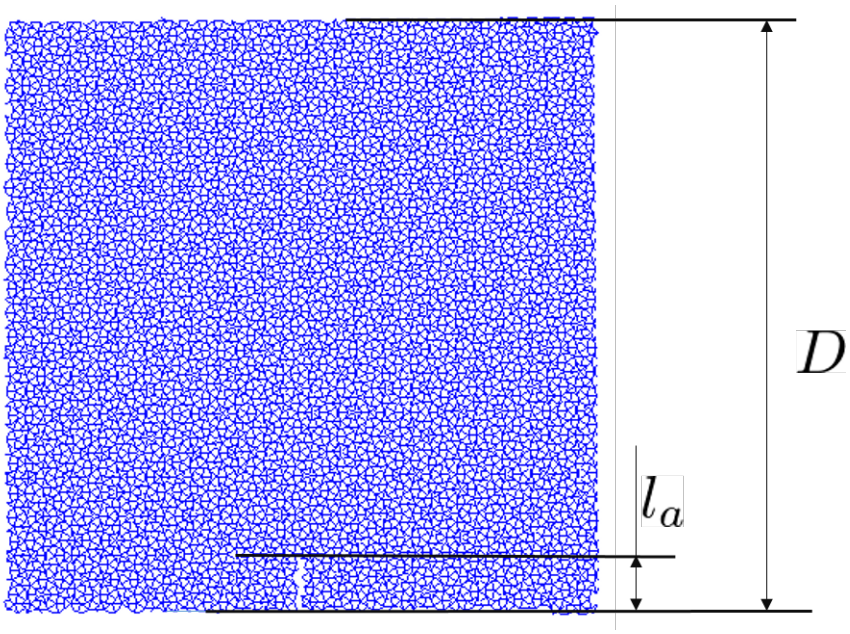

FIGURE 3.6 – Dynamic crack opening sample exampled.

3.3.3.1 Results

The first aim of the dynamic fracture simulation is to be able to reproduce the crack path of the unstable crack propagation. In figure.3.7 the dynamic simulation is compared to the same experimental results as in figure.3.1 with the experimental result on the left and the simulation on the right, where the broken beams have been removed for an easier visualization. The simulation shows a great agreement to the experimental result.

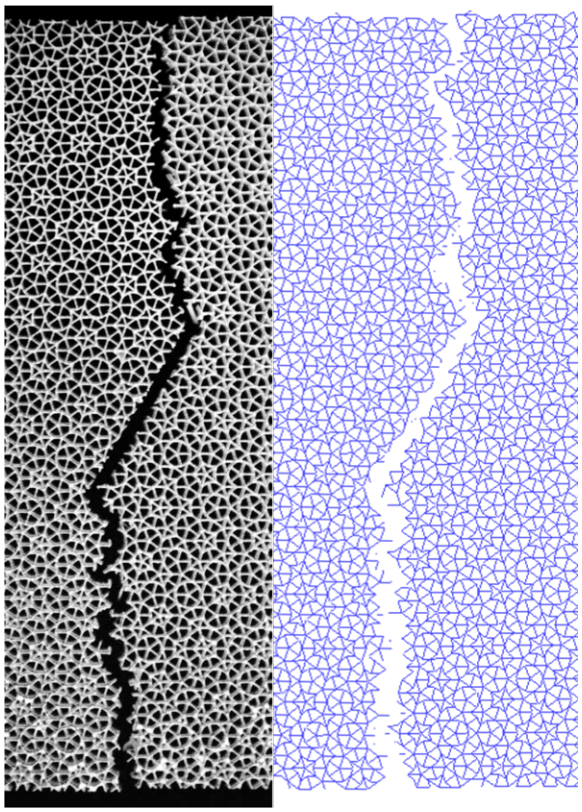

FIGURE 3.7 – Experimental and dynamic simulation comparison

A second aim is to see if the previous fracture behavior is conserved under dynamic simulations. In figure3.8 are presented two crack path resulting of dynamic simulation of the quasi-static test for two different slenderness. The previously disscused behaviour of sub structures is still visible and increasing the slenderness gives more wavier crack path, thus more dissipation.

In figure.3.9 the ratio R between energy needed to fully break the sample over the energy needed to break a fully brittle sample is plotted with the slenderness in abscissa. In practice R is the energy prensent in the sample after full failure divided by the energy when the crack initiates which would lead to a complete failure of a fully brittle material. It can be seen that the global increase of R with the increase of the slenderness is preserved. Once can observed a dip at $L/e = 6.25$ thus the linear evolution previously observed for quasi static simulations is not preserved for these simulations.

In figure.3.10 the results of dynamic crack opening for different slenderness at constant cross section area are shown. It seems that the substructure previously identified still plays a role for dynamic crack propagation by inducing deviations but the impact of the slenderness on the waviness of the crack path is less clear.

In order to better validate the dissipation behavior of the dynamic crack propagation the same calculation has been done with several parameters. Four different dt_{up} have been used ($4dt_c, 2dt_c$, $1dt_c$ and $0.5dt_c$) in order to compare the R ratio. The crack paths are

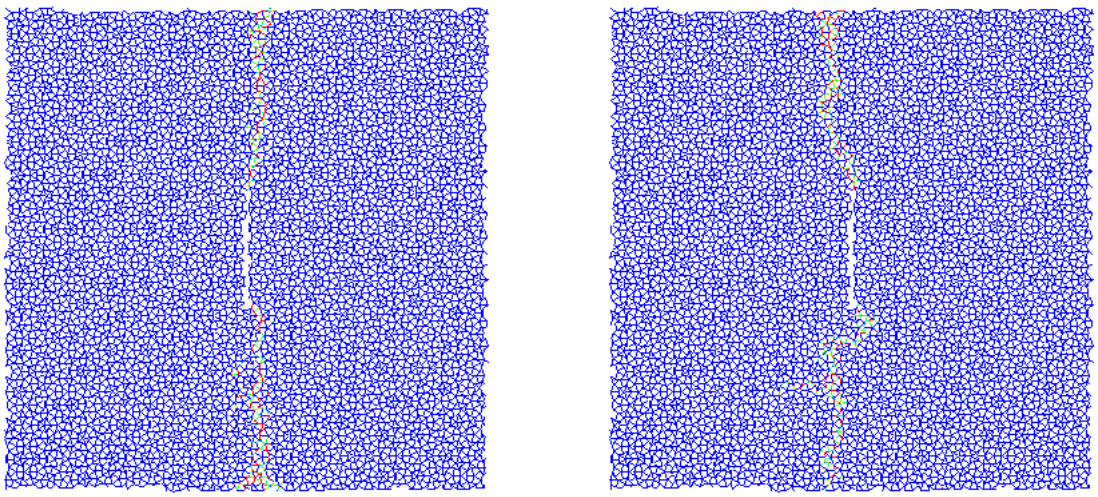

FIGURE 3.8 – Crack path for dynamic simulation of quasi static loading for a slenderness of 5 (left) and 10(right).

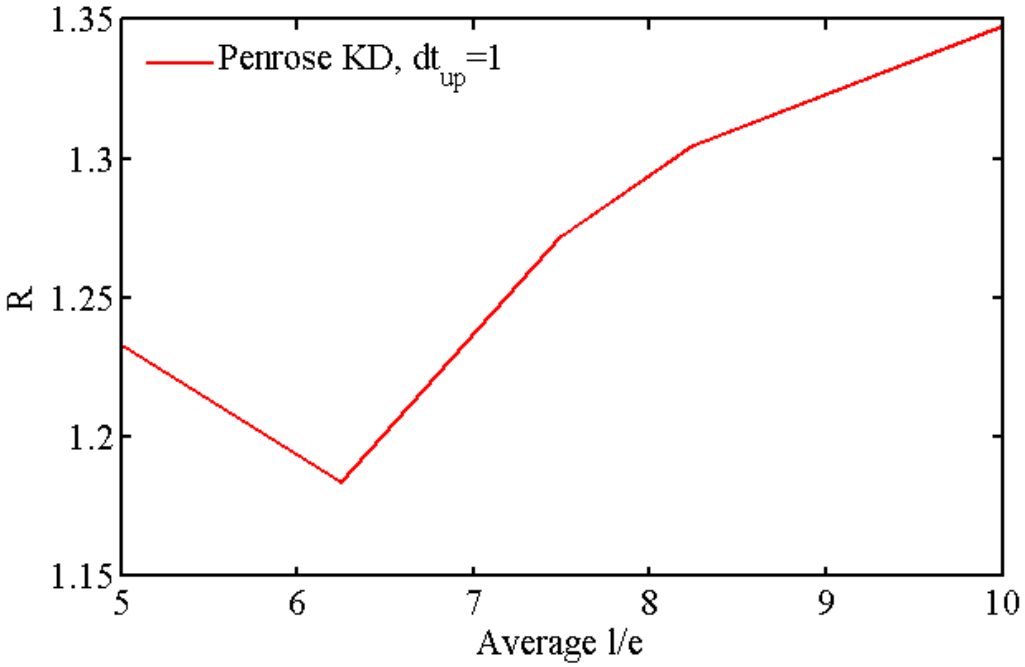

FIGURE 3.9 – evolution of R against slenderness of dynamic simulation of quasi static loading over slenderness.

shown in figure.3.11 for a slenderness of 5 with several dt_{up}. It can be seen that the crack path depend of dt_{up} but it is hard to conclude on the evolution of R from the crack path. In

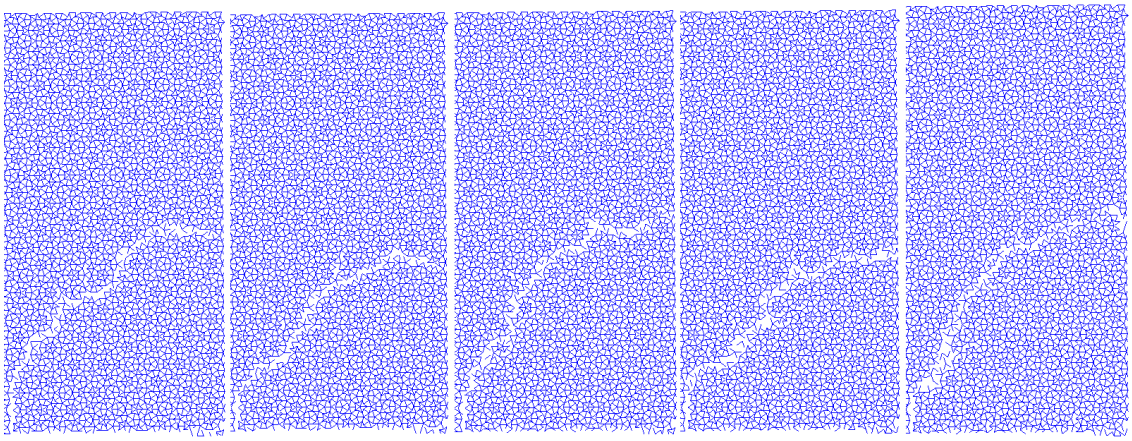

FIGURE 3.10 – crack path simulation for l/e (from left to right) $5, 6.25$, 7.75 , 8.25 and 10.

figure.3.12 the ratio R is plotted against slenderness for different dt_{up}. By the figure.3.12 one can observe that the previously described dissipation behavior is not present. There is a plateau form 5 to 8.25 then an abrupt growth of R. The variation of R with dt_{up} can also be noticed and the decrease of dt_{up} does not always lead to a monotonic convergence. Non the less the variation of R induced by the variation of dt_{up} is less important than the rise due to the variation of slenderness. Therefor the evolution of R with the slenderness is supposed valid.

This shows that the upper limit of the time step length influence the result of the dynamic crack propagation and that too high upper limit might lead to false prediction of crack path and energy dissipation due to the complex dynamic phenomenons that need to be grasp to correctly describe the crack dynamic propagation, too big time step would lead to miss some interactions.

At last the evolution of the R ration depending on the slenderness of beams can be compared between the previously introduced Qp lattices. In figure.3.13 is shown the evolution of R with the slenderness for Octogonal and kite & Dart Penrose lattices. It can be seen that although the two lattices evolve closely for small slenderness the Kite & Dart lattice present higher performance for higher slenderness.

3.4 Discussion and conclusion

A dynamic crack propagation model in Euler beam lattices with adaptive time scale and strain energy fracture criterion have been developed and validated against

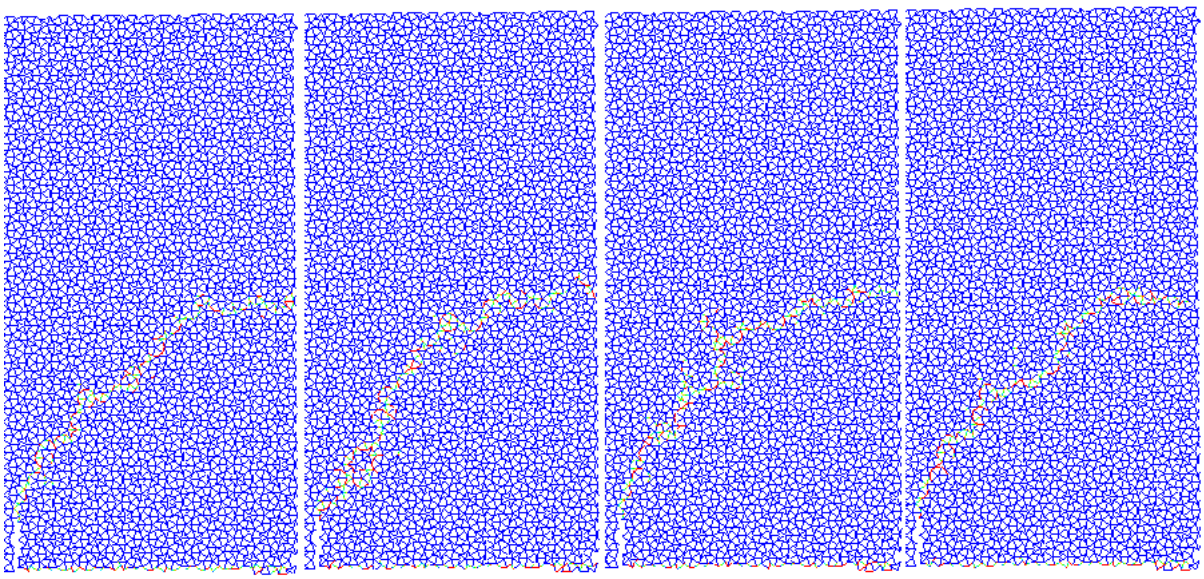

FIGURE 3.11 – crack path simulation for dt_{up} (from right to left) $4dt_c, 2dt_c$, $1dt_c$ and $0.5dt_c$ for slenderness of 5.

experiment. This model allow the simulation of several breaking configurations in order to investigate the influence of the slenderness, which seams to be a preponderant parameter of the crack resistance of beam lattices.

It seams that the quasi static loading preserved the dissipation behavior of Penrose Kyte & Dart lattices while the dynamic loading exhibit an plateau then an abrupt rise for a slenderness of 10. The influence of the calculus parameters on the dissipation behavior makes it hard to be certain of the presented results.

A buckling criterion for the break of a beam under compression loading could increase the reliability of the model. Especially regarding the slenderness used. The presence of bending in addition to compression imply to rigorously analyze the problem as it might not allow to use a simple Euler buckling criterion.

The different influence of slenderness over the stiffness matrix and the mass matrix might be a cause of the different dissipation behavior of dynamic crack propagation whereas in QS simulation the mass does not play a role. The interaction between crack propagation and mechanical wave propagation in the sample might also play a role but the great complexity of wave propagation in dynamic simulation would need special tools in order be analyzed.

The dynamic crack opening configuration might not be the best configuration to exhibit the crack propagation behavior of the beam lattices as it is hard to performed

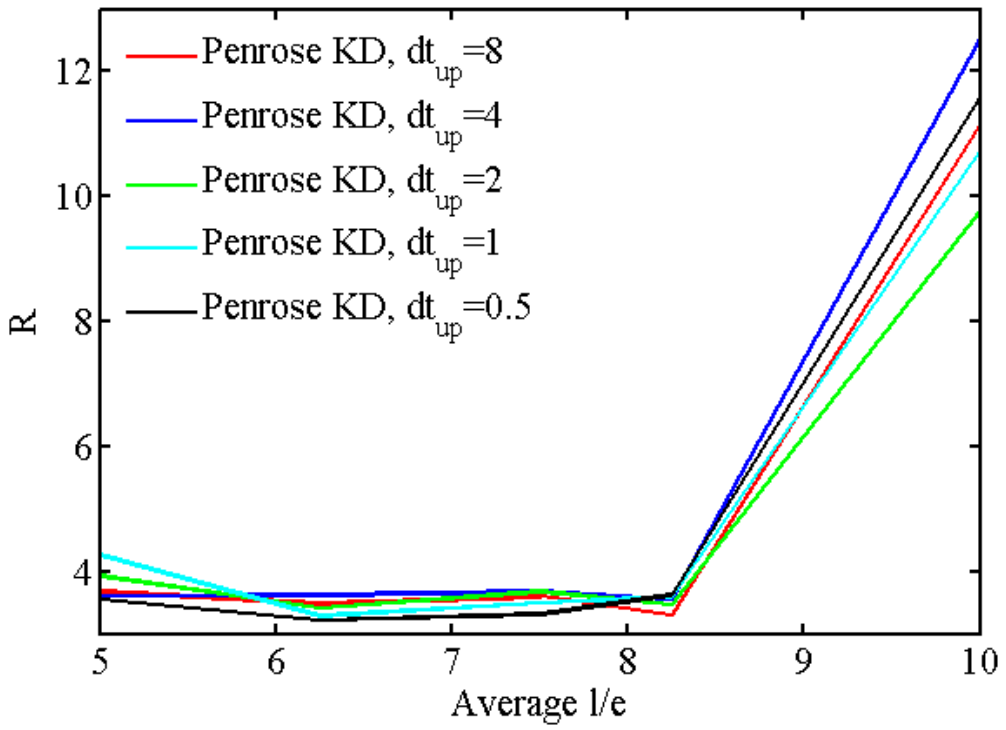

FIGURE 3.12 – evolution of R against slenderness for several dt_{up} for dynamic crack opening simulations.

the same simulation of different samples. A sample too flexible (for example hexagonal lattice) will not break and a too stiff one will break at the point of imposed dofs. It would be needed a configuration where the dynamic loading would open the initial crack regardless of the macroscopic stiffness of the sample. Due to the slenderness used compression waves can not be used as it would experimentally lead to crushing of the sample, thus test like Kaltoff or compression wave reflection can not be performed.

In order to have smoother results it could be interesting to add a small visco-elastic property to the FE model or a cohesive behavior on beam rupture , this would lead to filtering of the high frequency due to the brittle fracture.

Dynamic experiments have to be done in order to better validate the simulations and to statute over the calculus parameters. The need to add visco-elasticity to the model or a cohesive model would also be validated or not by the analysis of experimental results.

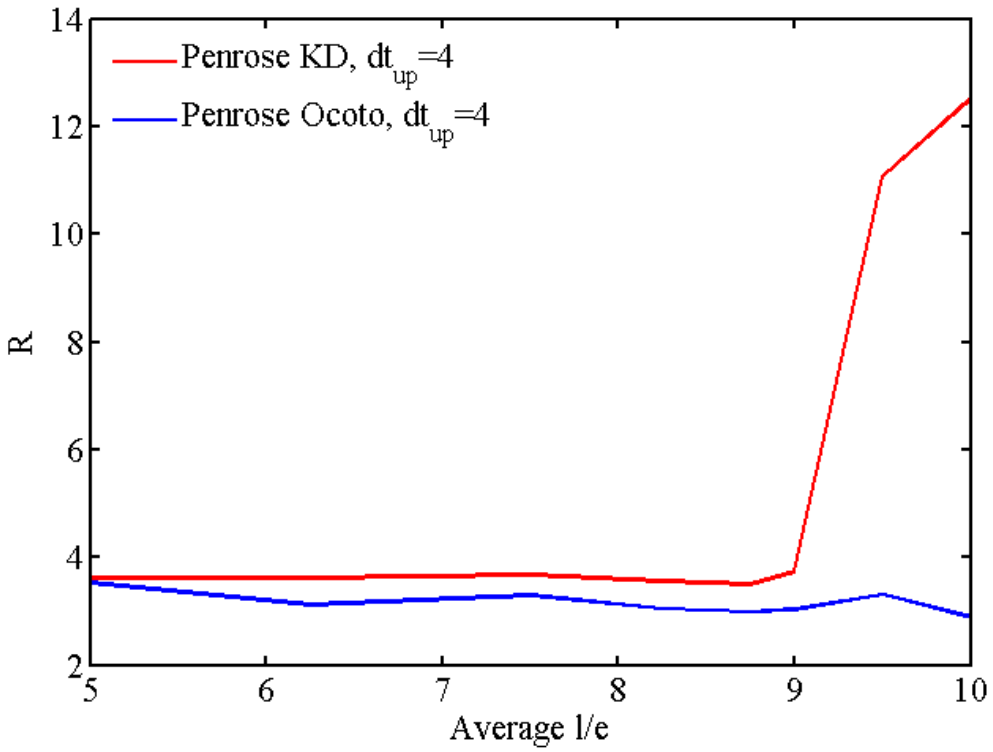

FIGURE 3.13 – evolution of R against slenderness for dynamic crack opening simulations of Octogonal and kite & Dart Penrose lattices.

Chapitre 4

Homogenization

Contents

4.1 Introduction

The interest in beam lattice materials has greatly increased since the development of additive manufacturing. Such manufacturing process allows the creation of materials having complex macroscopic properties due to their internal structure [**?**] [**?**]. In order to better understand, control and easily simulate the behaviour of beam lattices, it is often useful to create a continuous equivalent model. Classical homogenization methods allow to identify homogeneous medium easily for periodic structures [**?**] but without the abilities to take into account heterogeneities that have a preponderant role in stress concentrations, crack initiation and crack propagation [**?**] [**?**]. It has been shown that classical elasticity is not always able to exhibit the peculiar mechanical properties of architectured materials and that generalized continua are better candidates [**?**] [**?**]. Such continua introduce additional degrees of freedom (Cosserat, micomorphic media [**?**]...) or higher order gradient of the displacement field (second gradient materials ...). Coarse Graining methods allow the creation of an equivalent continuous material while keeping heterogeneity at the desired scale for any type of discrete structures (periodic, amorphous or quasi-periodic). This method has been applied at the atomic scale or for granular materials in order to identify a classical or Cosserat equivalent continuum [**?**, **?**].

The aim of this work is to transpose the coarse gaining method to finite element modelization in order to identify an equivalent Cosserat continuum for a 2D beam lattice at different scales. First the coarse graining principle is recalled and then applied to FE beam model. The CG strains, curvatures , stresses and torques are defined. These definitions are then used to identify a Cosserat equivalent media for a 2D square beam lattice and to obtain heterogeneous property fields for quasi-periodic lattices.

4.2 Principles of the Coarse Graining Method

We first focus on a discrete medium to summarize the main ideas of the Coarse Graining (CG) method. The CG method allows the definition of continuous quantities for a discrete medium while respecting mass and momentum conservation.

The microscopic mass density ρ^{mic} is defined as

$$\rho^{mic}(\mathbf{r}) = \sum_i m^i \delta(\mathbf{r} - \mathbf{r}_i) \tag{4.1}$$

where $\delta(\mathbf{r})$ is the Dirac delta function. The CG density can be defined as :

$$\rho_{cg}(\mathbf{r}) = \sum_i m^i \Phi^i(\mathbf{r}) \tag{4.2}$$

Where $\Phi^i(\mathbf{r})$ is the CG function that needs to be positive semi-definite and normalized (its integral over space is unity) to respect that the integral of the mass density over any volume equals the mass contained in this volume.

The CG momentum and CG density must verify the mass conservation equation

$$div(\mathbf{p^{cg}}) = -\dot{\rho_{cg}} \tag{4.3}$$

with $\dot{a}$ the time derivative of a and $\ddot{a}$ its double time derivative. The CG momentum at position $\mathbf{r}$ is the average momentum of nearby nodes weighted by the CG function. Thus the CG momentum can be expressed as :

$$p_\alpha^{cg}(\mathbf{r}) = \sum_i^N p_\alpha^i \Phi^i(\mathbf{r}) \tag{4.4}$$

where p_α^i is the momentum of the node i along the axis α.
In the case of internal rotation, one propose to define the CG angular momentum as :

$$J_\alpha^{cg}(\mathbf{r}) = \sum_i (J_\alpha^i + \sum_{\varphi\xi} \varepsilon_{\varphi\xi}(r_\varphi^i - r_\varphi) p_\xi^i) \Phi^i(\mathbf{r}) \tag{4.5}$$

where J_α^i is the angular momentum of the node i along the axis α. This equation corresponds to the transport of the kinematic torsor from the node to the coarse gaining point. In the following, α will often be omitted since the rotations are in-plane in the 2D beam lattice.

In the case of FE beam the nodal mass m^i, nodal momentum $\mathbf{p}^i$, angular momentum J^i and CG function $\Phi^i(\mathbf{r})$ needs to be redefined.

4.3 Finite Element Formulation and Nodal Quantities

For a mesh with N nodes, the vector of the degrees of freedom (dof) can be created : $\{q\} = \{q^1, q^2, ..., q^Q\}^t$ where $Q = (n+m)N$,N the number of nodes times, n the number of displacement degrees of freedom per nodes and m he number of rotation degrees of freedom per nodes. For example in a 2d beam model with nodal rotation $n = 2$ and $m = 1$

The Finite Element elastic problem is written with the following formulation (as previously defined in 1.3) :

$$\mathbf{Kq} + \mathbf{M\ddot{q}} = \mathbf{F} \tag{4.6}$$

In case of a free of load medium the previous equation(4.6) is equivalent for each node i to :

$$f_\alpha^i = \sum_{j=1}^N \sum_{\gamma=1}^{n+m} K_{\alpha\gamma}^{ij} q_\gamma^j = -\sum_{j=1}^N \sum_{\gamma=1}^{n+m} M_{\alpha\gamma}^{ij} \ddot{q}_\gamma^j \tag{4.7}$$

where we have introduced f_α^i, the opposite of the restauring force induced by the beams on the node i in the direction α. It can be noted that working with the assembled FE

matrices the interaction forces f_α^{ij} of node j on i, are no longer accessible. In order to obtain those forces, one needs to work with the elementary matrices $\mathbf{K}_e$ and $\mathbf{M}_e$:

$$\mathbf{f_e} = -\mathbf{K}_e \mathbf{q_e} \tag{4.8}$$

With $\mathbf{f_e} = \{\mathbf{f}^{ij}, \mathbf{f}^{ji}\}^t$ and $\mathbf{q_e} = \{\mathbf{q}^i, \mathbf{q}^j\}^t$. It can however be noted that :

$$f_\alpha^i = \sum_{j=1}^{N} f_\alpha^{ij} \; for \; \alpha = \{1, n\} \tag{4.9}$$

The momentum vector for each node i is defined as :

$$p_\alpha^i = \sum_{j=1}^{N} \sum_{\gamma=1}^{n+m} M_{\alpha\gamma}^{ij} \dot{q}_\gamma^j = \dot{w}_\alpha^i \; for \; \alpha = \{1, n\} \tag{4.10}$$

Where w_α^i is a notation introduced to be used latter, $w_\alpha^i = \sum_{j=1}^{N} \sum_{\gamma=1}^{n+m} M_{\alpha\gamma}^{ij} q_\gamma^j$. The rotation momentum for each node is defined as :

$$J_\alpha^i = \sum_{j=1}^{N} \sum_{\gamma=1}^{n+m} M_{\alpha\gamma}^{ij} \dot{q}_\gamma^j = \dot{\omega}_\alpha^i \; for \; \alpha = \{n+1, n+m\} \tag{4.11}$$

ω_α^i is again a notion to be used, $\omega_\alpha^i = \sum_{j=1}^{N} \sum_{\gamma=1}^{n+m} M_{\alpha\gamma}^{ij} q_\gamma^j$.

From the equilibrium equation written for the particular case of $\{q\}$ corresponding to 2D rigid body displacements, one has the following relations :

$$K_{\alpha\gamma}^{ii} = -\sum_{j \neq i}^{N} K_{\alpha\gamma}^{ij} \; for \; \gamma = \{1, n\} \tag{4.12}$$

$$K_{\alpha\gamma}^{ii} = -\sum_{j \neq i}^{N} \left(K_{\alpha\gamma}^{ij} + \sum_{\varphi\xi}^{n} \varepsilon_{\varphi\xi} K_{\alpha\xi}^{ij} r_\varphi^{ij} \right) for \; \gamma = \{n+1, m\} \tag{4.13}$$

With $r_\varphi^{ij} = r_\varphi^j - r_\varphi^i$. The stiffness matrix has a big symmetry :$K_{\alpha\gamma}^{ij} = K_{\gamma\alpha}^{ji}$, the small symmetries and anti-symmetries are summed up in the following table :

$i \neq j$	$\gamma = \{1, n\}$	$\gamma = \{n+1, n+m\}$
$\alpha = \{1, n\}$	$K_{\alpha\gamma}^{ij} = K_{\alpha\gamma}^{ji}$	$K_{\alpha\gamma}^{ij} = -K_{\alpha\gamma}^{ji}$
$\alpha = \{n+1, n+m\}$	$K_{\alpha\gamma}^{ij} = -K_{\alpha\gamma}^{ji}$	$K_{\alpha\gamma}^{ij} = K_{\alpha\gamma}^{ji}$

TABLE 4.1 – Table of stiffness matrix symmetries

These relations can be identified on the stiffness matrix of a reference element and are not impacted by the rotations. It is important to notice that these relations established in equation 4.13 and table 4.1 are only true in the case of a 2D problem with one out of plane rotation. A 3D problem with 3 rotations could however be treated with the same methodology to obtain the correct CG formulation.

4.3.1 Coarse Grained Momentum

The coarse grained impulsion and coarse grained density must verify the mass conservation equation : $div(\mathbf{p^{cg}}) = -\dot{\rho_{cg}}$. A solution is to choose the following definitions :

$$\Phi^i(\mathbf{r}) = \Phi(\mathbf{r} - \widehat{\mathbf{r}}^i) = \frac{1}{\sqrt{(2\pi)^n} l_{cg}^n} e^{-\frac{\|\mathbf{r} - \widehat{\mathbf{r}}^i\|^2}{2l_{cg}^2}} \tag{4.14}$$

with :

$$\widehat{r}_\alpha^i = \sum_j^N \sum_{\gamma=1}^{n+m} \frac{M_{\alpha\gamma}^{ij}}{m^i} (r_\gamma^j + q_\gamma^j) \tag{4.15}$$

$$m^i = \frac{1}{n} \sum_j^N \sum_{\alpha=1}^{n} \sum_{\beta=1}^{n} M_{\alpha\beta}^{ij} \tag{4.16}$$

$$\tag{4.17}$$

and l_{cg} the coarse graining length. Varying this length allows to have a CG function more or less wide an to define an continuum material at different scales. The main requirement of this definition is that $\frac{\partial \Phi^i}{\partial t} = \sum_j^N \sum_{\gamma=1}^{n+m} \frac{M_{\alpha\gamma}^{ij}}{m^i} \dot{q}_\gamma^j \frac{\partial \Phi^i}{\partial r_\alpha}$ in order to respect the conservation of mass (4.3) with the definition (4.2) for the mass density.

With these definitions, the integral of the coarse graining function over space is one as needed [**?**] and the conservation of mass is verified since :

$$-\frac{\partial \rho_{cg}}{\partial t} = -\frac{\partial \sum_i m^i \Phi^i(\mathbf{r})}{\partial t} = -\sum_\alpha m^i \frac{\partial \Phi^i}{\partial r_\alpha} \frac{\partial (r_\alpha - \widehat{r}_\alpha^i)}{\partial t} = \sum_\alpha m^i \sum_j^N \sum_{\gamma=1}^{n+m} \frac{M_{\alpha\gamma}^{ij}}{m^i} \dot{q}_\gamma^j \frac{\partial \Phi^i}{\partial r_\alpha} = div(\mathbf{p^{cg}}) \tag{4.18}$$

using (4.2), (4.14) and (4.10).

4.3.2 Coarse Grained Rotation Momentum

In order to maintain the coherence with the previous definition, the CG rotation momentum for a 2D FE problem with 1 rotation is defined as :

$$J_\alpha^{cg}(\mathbf{r}) = \sum_i (J_\alpha^i + \sum_{\varphi\xi}^{n} \varepsilon_{\varphi\xi} (r_\varphi^i - r_\varphi) p_\xi^i) \Phi^i(\mathbf{r}) \; for \; \alpha = \{n+1, n+m\} \tag{4.19}$$

and

$$I_{cg} = \sum_i (m^i \|\mathbf{r}^i - \mathbf{r}\|^2 + I^i) \Phi^i \; ; \; I^i = \frac{1}{m} \sum_j^N \sum_{\alpha=n+1}^{n+m} \sum_{\beta=n+1}^{n+m} M_{\alpha\beta}^{ij} \tag{4.20}$$

To get the equation in a 3D case one would need to redefine the arm lever of the impulsion in 3D. The definition of the previous CG density and rotation momentum for a FE mesh is also equivalent to the Goldhish formulation [**?**] if the mesh has concentrated mass and rotational inertia at the nodes, the mass matrix being diagonal in this case. For example, for a mesh where each node i has 2 displacements and one rotation as dofs, the mass matrix would be :

$$\mathbf{M} = \begin{bmatrix} \ddots & & & & & \\ & m^i & & & & \\ & & m^i & & & \\ & & & I^i & & \\ & & & & \ddots & \end{bmatrix} \tag{4.21}$$

4.4 Coarse Grained Displacements and Strains

From the CG momentum and density definitions the CG velocity can be defined and then the CG displacement can be obtained by time integration.

4.4.1 CG Displacements

As the CG medium satisfies mass conservation (4.3), the coarse grained velocity can be defined as :

$$v_\alpha^{cg} = \frac{p_\alpha^{cg}}{\rho_{cg}} \tag{4.22}$$

The displacement can then be calculated by time integration :

$$\begin{aligned} u_\alpha^{cg}(\mathbf{r},t) = \int_0^t v^{cg}(\mathbf{r},t')dt' = \int_0^t \frac{p_\alpha^{cg}}{\rho_{cg}} &= \int_0^t \sum_i^N \dot{w}_\alpha^i \frac{\Phi^i}{\rho_{cg}} dt' \\ &= \sum_i^N w_\alpha^i \frac{\Phi^i}{\rho_{cg}} - \int_0^t \sum_i^N w_\alpha^i \frac{\partial}{\partial t'}\left(\frac{\Phi^i}{\rho_{cg}}\right) dt' \\ &= u_\alpha^l - \int_0^t \sum_i^N \frac{w_\alpha^i}{\rho_{cg}^2}\left(\frac{\partial \Phi^i}{\partial t'}\rho_{cg} - \frac{\partial \rho_{cg}}{\partial t'}\Phi^i\right) dt' \end{aligned} \tag{4.23}$$

Where the integrated term is of second order, thus :

$$u_\alpha^{cg} \simeq u_\alpha^l = \sum_i^N w_\alpha^i \frac{\Phi^i}{\rho_{cg}} = \sum_{i=1}^N \sum_{j=1}^N \sum_{\gamma=1}^{n+m} M_{\alpha\gamma}^{ij} q_\gamma^j \frac{\Phi^i}{\rho_{cg}} \tag{4.24}$$

In Appendix.B.1 a more detailed description of this term is given. This formulation depending only on nodal information (Mass matrix and displacements) can be easily implemented in order to calculate the CG displacements at any point of the domain.

4.4.2 CG Strains

By a simple derivation over space the CG strains can be defined :

$$\begin{aligned}\frac{\partial u^{cg}_{\alpha}}{\partial r_{\beta}} &= \frac{\partial}{\partial r_{\beta}}\left(\frac{\sum_i^N \Phi^i.w^i_{\alpha}}{\sum_j^N m^j\Phi^j}\right) = \frac{1}{\rho^2_{cg}}\sum_{ij}^{N}\left(w^i_{\alpha}m^j\frac{\partial\Phi^i}{\partial r_{\beta}}\Phi^j - w^i_{\alpha}m^j\frac{\partial\Phi^j}{\partial r_{\beta}}\Phi^i\right)\\ &= \frac{1}{\rho^2_{cg}}\sum_{ij}^{N}\left(w^i_{\alpha}m^j\frac{\partial\Phi^i}{\partial r_{\beta}}\Phi^j - w^j_{\alpha}m^i\frac{\partial\Phi^i}{\partial r_{\beta}}\Phi^j\right) = \frac{1}{\rho^2_{cg}}\sum_{ij}^{N}\left(w^i_{\alpha}m^j - w^j_{\alpha}m^i\right)\frac{\partial\Phi^i}{\partial r_{\beta}}\Phi^j\end{aligned} \tag{4.25}$$

4.4.3 CG Rotations

With the absence of mass conservation equivalent for angular momentum the CG angle is can be choosen as :

$$\theta^{cg}_{\alpha} = \frac{\sum_i \omega^i_{\alpha}\Phi_i}{I^{cg}} \tag{4.26}$$

It can be tempting to have used the same method as before : from the definition of the CG angular momentum and rotation inertia, the definition of the CG angular velocity can be obtained and then the rotation by time integration.

$$\begin{aligned}J^{cg}_{\alpha} = I^{cg}.\Omega^{cg}_{\alpha} &= \sum_i (J^i_{\alpha} + \sum_{\varphi\xi}^{n}\varepsilon_{\varphi\xi}(r^i_{\varphi} - r_{\varphi})p^i_{\xi}).\Phi^i(\mathbf{r})\\ \Omega^{cg}_{\alpha} &= \sum_i (J^i_{\alpha} + \sum_{\varphi\xi}^{n}\varepsilon_{\varphi\xi}(r^i_{\varphi} - r_{\varphi})p^i_{\xi})\frac{\Phi^i(\mathbf{r})}{I^{cg}}\end{aligned} \tag{4.27}$$

$$\begin{aligned}\theta^{cg}_{\alpha} = \int_0^t \Omega^{cg}_{\alpha}(t')dt' &= \int_0^t \sum_i (J^i_{\alpha} + \sum_{\varphi\xi}^{n}\varepsilon_{\varphi\xi}(r^i_{\varphi} - r_{\varphi})p^i_{\xi})\frac{\Phi^i(\mathbf{r})}{I^{cg}}dt'\\ &= \int_0^t \sum_i^N (\dot{\omega}^i_{\alpha} + \sum_{\varphi\xi}^{n}\varepsilon_{\varphi\xi}(r^i_{\varphi} - r_{\varphi})\dot{w}^i_{\xi})\frac{\Phi_i(\mathbf{r})}{I^{cg}}dt'\\ = \sum_i^N (\omega^i_{\alpha} + \sum_{\varphi\xi}^{n}\varepsilon_{\varphi\xi}(r^i_{\varphi} - r_{\varphi})w^i_{\xi})\frac{\Phi^i(\mathbf{r})}{I^{cg}} &- \int_0^t \sum_i^N \left(\omega^i_{\alpha}.\frac{\partial}{\partial t'}\left(\frac{\Phi^i}{I_{cg}}\right) + \sum_{\varphi\xi}^{n}\varepsilon_{\varphi\xi}w^i_{\xi}.\frac{\partial}{\partial t'}\left(\frac{(r^i_{\varphi} - r_{\varphi})\Phi^i}{I_{cg}}\right)\right)dt'\end{aligned} \tag{4.28}$$

As before, the integrated term is of second order and the details can be found in Appendix.B.2. Thus,

$$\theta_\alpha^{cg} \simeq \theta_\alpha^l = \sum_i (\omega_\alpha^i + \sum_{\varphi\xi}^n \varepsilon_{\varphi\xi}(r_\varphi^i - r_\varphi) w_\xi^i) \frac{\Phi_i(\mathbf{r})}{I^{cg}} \tag{4.29}$$

This method gives however non consistent results. Indeed if the curvatures are calculated by taking the spacial derivatives, one obtains :

$$\begin{aligned} k_{\alpha\beta}^{cg} = \frac{1}{I_{cg}^2} . \sum_{ij} \Big[(\sum_\xi^n -\varepsilon_{\beta\xi} w_\xi^i . (m^j . \|\mathbf{r}^j - \mathbf{r}\|^2 + I^j) + 2 . (\omega_\alpha^i + \sum_{\varphi\xi}^n \varepsilon_{\varphi\xi}(r_\varphi^i - r_\varphi) w_\xi^i) . m^j . (r_\beta^j - r_\beta)) . \Phi_i . \Phi_j \\ + \Big((\omega_\alpha^i + \sum_{\varphi\xi}^n \varepsilon_{\varphi\xi}(r_\varphi^i - r_\varphi) w_\xi^i) . (m^j . \|\mathbf{r}^j - \mathbf{r}\|^2 + I^j) - (\omega_\alpha^j + \sum_{\varphi\xi}^n \varepsilon_{\varphi\xi}(r_\varphi^j - r_\varphi) w_\xi^j) . (m^i . \|\mathbf{r}^i - \mathbf{r}\|^2 + I^i) \Big) \frac{\partial \Phi_i}{\partial r_\beta} \Phi_j . \Big] \end{aligned} \tag{4.30}$$

Due to the term including a lever arm in the unproper angle definition (4.29) a term directly proportional to the displacement arise in the curvature expression (i.e $-\varepsilon_{\beta\xi} w_\xi^i . (m^j . \|\mathbf{r}^j - \mathbf{r}\|^2 + I^j)$). Simulations thus give curvatures proportional to the displacement in the case of purely tensile loading on a square lattice, this is non consistent with what is expected of such lattice.

4.4.4 CG Curvature

A simple space derivative of θ^{cg} allows to calculate the curvatures from (4.26) :

$$\begin{aligned} k_{\alpha\beta}^{cg} = \frac{\partial \theta_\alpha^{cg}}{\partial r_\beta} = \frac{\partial}{\partial r_\beta} \left(\frac{\sum_i \omega_\alpha^i \Phi_i}{I^{cg}} \right) = \frac{1}{I_{cg}^2} \sum_{ij}^N \left(\omega^i m^j \frac{\partial \Phi^i}{\partial r_\beta} \Phi^j - \omega_\alpha^i m^j \frac{\partial \Phi^j}{\partial r_\beta} \Phi^i \right) \\ = \frac{1}{I_{cg}^2} \sum_{ij}^N \left(\omega^i m^j \frac{\partial \Phi^i}{\partial r_\beta} \Phi^j - \omega^j m^i \frac{\partial \Phi^i}{\partial r_\beta} \Phi^j \right) = \frac{1}{I_{cg}^2} \sum_{ij}^N \left(\omega^i m^j - \omega^j m^i \right) \frac{\partial \Phi^i}{\partial r_\beta} \Phi^j \end{aligned} \tag{4.31}$$

4.5 Coarse Grained Stresses and Torques

4.5.1 CG Stresses

The CG Stresses can be identified from the dynamic equilibrium of a Cosserat medium. The dynamic equilibrium is written as :

$$\frac{\partial p_\alpha^{cg}}{\partial t} = \sum_\beta \frac{\partial}{\partial r_\beta} \left(\sigma_{\alpha\beta} - \rho_{cg} V_\alpha^{cg} V_\beta^{cg} \right) \tag{4.32}$$

$$\frac{\partial p_\alpha^{cg}}{\partial t} = \frac{\partial \sum_i^N p_\alpha^i.\Phi^i}{\partial t} = \sum_i^N \left(p_\alpha^i \frac{\partial \Phi^i}{\partial t} + \dot{p}_\alpha^i \Phi^i \right) = \sum_i^N \left(\dot{p}_\alpha^i \Phi^i - p_\alpha^i \sum_\beta^n \frac{\dot{w}_\beta^i}{m^i} \frac{\partial \Phi^i}{\partial r_\beta} \right)$$
$$= -\Big(\underbrace{\sum_i^N f_\alpha^i \Phi^i}_{A_\alpha} + \underbrace{\sum_i^N p_\alpha^i \sum_\beta^n \frac{p_\beta^i}{m^i} \frac{\partial \Phi^i}{\partial r_\beta}}_{B_\alpha} \Big) \tag{4.33}$$

The calculus can be done using the FE matrix or the interactions forces. Both methods will be detailed in this section and the formulas using each are given. Depending on the easiest quantities available, one can choose to work with one or the other.

The details of the calculations for A_α and B_α are presented in appendix.B.3. The dynamical stress can finally be identified as :

$$\sigma_{\alpha\beta} = \left(\sum_{ij \neq i}^N \sum_{\gamma=1}^{n+m} K_{\alpha\gamma}^{ij} q_\gamma^j \widehat{r}_\beta^{ji} \int_0^1 \Phi(\mathbf{r} - \widehat{\mathbf{r}}^i + s\widehat{\mathbf{r}}^{ji}) ds - \sum_{ij}^N \sum_{\gamma=n+1}^{n+m} K_{\alpha\gamma}^{ij} q_\gamma^j g_\beta^j \right) - \sum_i^N m^i \tilde{v}_\alpha^i \tilde{v}_\beta^i \Phi^i \tag{4.34}$$

Where $g_\beta^i = \frac{r_\beta - \widehat{r}_\beta^i}{\|r_\beta - \widehat{r}_\beta^i\|^2} \frac{-1}{2.\pi} . e^{\frac{-\|r_\beta - \widehat{r}_\beta^i\|^2}{2l_{cg}^2}}$ and $\widehat{\mathbf{r}}^{ji} = \widehat{\mathbf{r}}^i - \widehat{\mathbf{r}}^j$. The method to obtain g_β^i is detailed in section B.3.

$\tilde{v}_\beta^i = \frac{p_\beta^i}{m^i} - v_\beta^{cg}$ is the fluctuation of nodal velocities to the CG velocities therefore $-\sum_i^N m^i \tilde{v}_\alpha^i \tilde{v}_\beta^i \Phi^i$ is the fluctuating kinetic part of the stress. The formula is very similar to the equation obtained by Goldirsch[**?**] in the case of granular materials.

Using the interaction forces the following formula is obtained :

$$\sigma_{\alpha\beta} = -\frac{1}{2} \sum_{ij}^N \sum_{\gamma=1}^{n+m} f_\alpha^{ij} \widehat{r}_\beta^{ji} \int_0^1 \Phi(\mathbf{r} - \widehat{\mathbf{r}}^i + s\widehat{\mathbf{r}}^{ji}) ds - \sum_i^N m^i \tilde{v}_\alpha^i \tilde{v}_\beta^i \Phi^i \tag{4.35}$$

Using this formulation one can calculate the expression of the anti-symmetric part of the stress :

$$\sum_{\alpha\beta} \varepsilon_{\alpha\beta} \sigma_{\alpha\beta} = -\frac{1}{2} \sum_{ij}^N \sum_{\gamma=1}^{n+m} \widehat{\mathbf{r}}^{ji} \times \mathbf{f}^{ij} \int_0^1 \Phi(\mathbf{r} - \widehat{\mathbf{r}}^i + s\widehat{\mathbf{r}}^{ji}) ds \tag{4.36}$$

Thus in the case of tangential forces between nodes i and j the stress will be non symmetric. This further implies the use of a Cosserat medium to approximate the beam lattices.

4.5.2 CG Torques

The coarse grained torques are identified from the momentum dynamic equilibrium. In the following the α indicating the axis will be omitted due to the fact that there is only one rotation in 2D. In the planar Cosserat formalism, the rotational momentum dynamic equilibrium is written as :

$$\frac{\partial J^{cg}}{\partial t} = \sum_{\beta}^{n} \frac{\partial}{\partial r_\beta}\left(m_\beta - V_\beta^{cg} J^{cg}\right) - \sum_{\beta\gamma}^{n} \varepsilon_{\beta\gamma}\sigma_{\beta\gamma} \tag{4.37}$$

$$\begin{aligned}
\frac{\partial J^{cg}}{\partial t} &= \frac{\partial}{\partial t}\left(\sum_{i}^{N}\left(\sum_{\varphi\xi}^{n}\varepsilon_{\varphi\xi}(r_\varphi^i - r_\varphi)p_\xi^i + J^i\right)\Phi^i\right) \\
&= \sum_{i}^{N}\frac{\partial}{\partial t}\left(\sum_{\varphi\xi}^{n}\varepsilon_{\varphi\xi}\left((r_\varphi^i - r_\varphi)p_\xi^i + J^i\right)\Phi^i + \sum_{i}^{N}\sum_{\varphi\xi}^{n}\varepsilon_{\varphi\xi}\left((r_\varphi^i - r_\varphi)p_\xi^i + J^i\right)\frac{\partial \Phi^i}{\partial t}\right. \\
&= \sum_{i}^{N}\sum_{\varphi\xi}^{n}\varepsilon_{\varphi\xi}\left((r_\varphi^i - r_\varphi)\dot{p}_\xi^i + \dot{J}^i\right)\Phi^i - \sum_{i}^{N}\sum_{\beta}^{n}\sum_{\varphi\xi}^{n}\varepsilon_{\varphi\xi}\left((r_\varphi^i - r_\varphi)p_\xi^i + J^i\right)\frac{p_\beta^i}{m^i}\frac{\partial \Phi^i}{\partial r_\beta} \\
&= \sum_{i}^{N}\sum_{\varphi\xi}^{n}\varepsilon_{\varphi\xi}\left((r_\varphi^i - r_\varphi)\dot{p}_\xi^i + \dot{J}^i\right)\Phi^i - \sum_{i}^{N}\sum_{\beta}^{n}\sum_{\varphi\xi}^{n}\varepsilon_{\varphi\xi}\left((r_\varphi^i - r_\varphi)p_\xi^i + J^i\right)\frac{p_\beta^i}{m^i}\frac{\partial \Phi^i}{\partial r_\beta} \\
&= -\Bigg(\underbrace{\sum_{ij}^{N}\sum_{\varphi\xi}^{n}\sum_{\gamma=1}^{n+m}\varepsilon_{\varphi\xi}(r_\varphi^i - r_\varphi)K_{\xi\gamma}^{ij}q_\gamma^j\Phi^i}_{C_n} + \underbrace{\sum_{ij}^{N}\sum_{\gamma=1}^{n+m}K_{\theta\gamma}^{ij}q_\gamma^j\Phi^i}_{C_\theta}\Bigg) \\
&\quad \underbrace{-\sum_{i}^{N}\sum_{\beta}^{n}\sum_{\varphi\xi}^{n}(\varepsilon_{\varphi\xi}(r_\varphi^i - r_\varphi)p_\xi^i + J^i)\frac{p_\beta^i}{m^i}\frac{\partial \Phi^i}{\partial r_\beta}}_{D}
\end{aligned} \tag{4.38}$$

Here $K_{\theta\gamma}^{ij}$ indicate $K_{\alpha\gamma}^{ij}$ for $\alpha = n+m$, corresponding to the rotation axis.

The details of the calculations for C_α , C_θ and D are presented in appendix.B.4. Then one can identify the torques as :

$$\begin{aligned}
m_\beta = &\sum_{ij\neq i}^{N}\sum_{\varphi\xi}^{n}\sum_{\gamma=1}^{n+m}\left(\varepsilon_{\varphi\xi}(r_\varphi^i - r_\varphi)K_{\xi\gamma}^{ij}q_\gamma^j + K_{\theta\gamma}^{ij}q_\gamma^j\right).\widehat{r}_\beta^{ji}\int_0^1 \Phi(\mathbf{r} - \widehat{\mathbf{r}}^i + s\widehat{\mathbf{r}}^{ji})ds \\
&-\sum_{ij}^{N}\sum_{\varphi\xi}^{n}\sum_{\gamma=n+1}^{n+m}\varepsilon_{\varphi\xi}(r_\varphi^j - r_\varphi)K_{\xi\gamma}^{ij}q_\gamma^j g_\beta^j - \sum_{i}^{N}\sum_{\varphi\xi}^{n}\left(\varepsilon_{\varphi\xi}(r_\varphi^i - r_\varphi)p_\xi^i + J^i\right)\tilde{v}_\beta^i\Phi^i
\end{aligned} \tag{4.39}$$

With $-\sum_i^N \sum_{\varphi\xi}^n \left(\varepsilon_{\varphi\xi}(r_\varphi^i - r_\varphi)p_\xi^i + J^i\right)\tilde{v}_\beta^i \Phi^i$ being the kinetic part of the torque. Here again the formula is close to the one in [**?**].

Using the interactions forces the following formula is obtained :

$$m_\beta = -\frac{1}{2}\sum_{ij}^{N}\sum_{\varphi\xi}^{n}\sum_{\gamma=1}^{n+m}\left(\varepsilon_{\varphi\xi}(r_\varphi^i - r_\varphi)f_\xi^{ij} + f_\theta^{ij}\right)\widehat{r}_\beta^{ji}\int_0^1 \Phi(\mathbf{r} - \widehat{\mathbf{r}}^i + s\widehat{\mathbf{r}}^{ji})ds$$
$$-\sum_i^N\sum_{\varphi\xi}^n\left(\varepsilon_{\varphi\xi}(r_\varphi^i - r_\varphi)p_\xi^i + J^i\right)\tilde{v}_\beta^i\Phi^i \tag{4.40}$$

4.6 Cosserat Equivalent Continuum

Knowing strains and stresses for each point of the CG medium the elastic moduli of the Cosserat medium can be identified at each point. It is assumed that the elasticity tensor is of cubic symmetry (as defined in 4.41). This hypothesis is first taken for the study of the square lattice, and the octogonal Penrose lattice as they present a 4-fold symmetry. The kyte & dart pernrose lattice with it's 5-fold symmetry should lead to isotropic CG medium that is a particular case of cubic symmetry. We note :

$$\mathbf{D} = \begin{bmatrix} D1 & D2 & 0 & 0 & 0 & 0 \\ & D1 & 0 & 0 & 0 & 0 \\ & & D3 & D4 & 0 & 0 \\ & Sym & & D3 & 0 & 0 \\ & & & & D5 & 0 \\ & & & & & D5 \end{bmatrix} \tag{4.41}$$

At each CG point, the following equation must be verified :

$$\widehat{\boldsymbol{\sigma}} = \mathbf{D}\widehat{\boldsymbol{e}} \tag{4.42}$$

where $\widehat{\boldsymbol{\sigma}} = (\sigma_{xx}, \sigma_{yy}, \sigma_{xy}, \sigma_{yx}, m_x, m_y)^t$ and $\widehat{\boldsymbol{e}} = (e_{xx}, e_{yy}, e_{xy}, e_{yx}, k_x, k_y)^t$ In order to activate all moduli five simulations are performed. The simulations used are 1 imposed traction in each direction (e_{xx} and e_{yy}), 2 imposed shears (e_{xy} and e_{xy}) and 2 imposed curvatures (k_x and k_y). The previous equation can be rewritten as :

$$\widehat{\boldsymbol{\sigma}} = \widehat{\mathbf{D}}\overline{\overline{\widehat{\boldsymbol{e}}}} \tag{4.43}$$

Where $\widehat{\mathbf{D}} = [D1\ D2\ D3\ D4\ D5]^t$ and $\overline{\overline{\widehat{\boldsymbol{e}}}}$ is a 6x6 (6 equations for each of the 6 simulations) by 5 tensor. Finally $\widehat{\mathbf{D}}$ is obtained at each point using the build in Matlab function :

$$\widehat{\mathbf{D}} = pinv(\overline{\overline{\widehat{\boldsymbol{e}}}})\widehat{\boldsymbol{\sigma}} \tag{4.44}$$

As the $\overline{\overline{\widehat{\boldsymbol{e}}}}$ matrix is not square, $pinv()$ calculates its Moore–Penrose pseudo-inverse that gives the least square solution of the linear system.

4.6.1 Application to a square beam lattice

In order to illustrate the use of the previously defined CG method, it will be applied to a periodic beam lattice of square cells as presented in figure.4.1. All calculus are made in Matlab using an home made FE code for the simulations and an implementation of the previously defined CG formulas. To model the beam lattice all beams are of length L and are discretized by one Euler-Bernoulli beam element with two nodes. Each nodes have 3 dof, two translations (u_x^i,u_y^i) and one rotation (θ). The FE model of a 1000x1000 cells square lattice is created and the displacement of the nodes are calculated for several loading scenarios. Then the different CG quantities can be calculated on one fifth of the mesh to be able to calculate the CG quantities at the border.

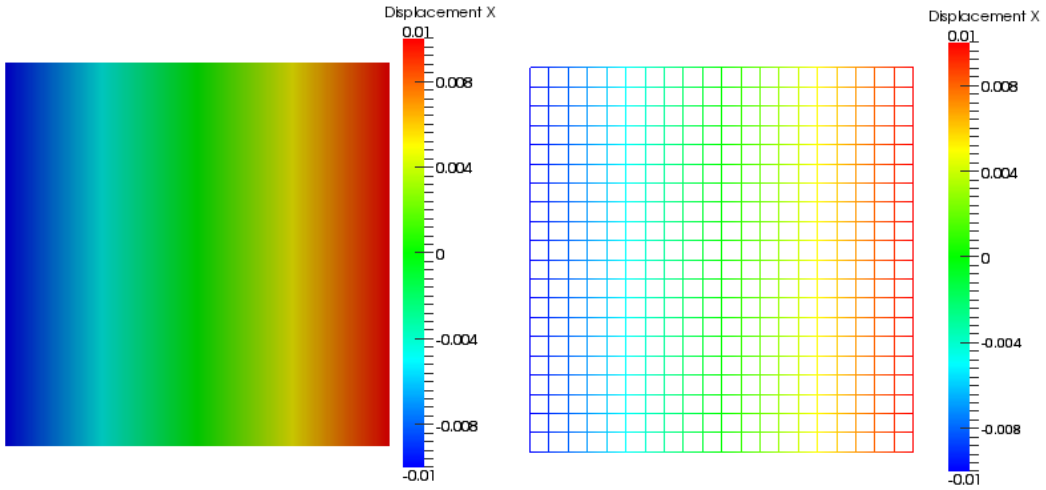

FIGURE 4.1 – Displacement X CG(left) at $l_{cg} = L$ and the corresponding 20x20 square lattice under imposed traction along X

The elastic properties can be calculated for several coarse graining lengths. In figures4.2, 4.4 and 4.5 is presented the evolution of the mean of the elastic moduli as a function of the coarse graining length l_{cg}, their standard deviation is also plotted in the graphs .

In figure.4.2 one can notice the convergence of $D1$ as a function of l_{cg}, In figure.4.4 $\frac{D3+D4}{2}$ corresponds to μ in eq.1.66 and $\frac{D3-D4}{2}$ to μ_c. The elastic moduli closely correspond to what can be found in the literature for $\lambda+2\mu$ and μ. μ_c on the other hand seems to differ from homogenization methods [**?**].

In figure.4.5 the bending modulus increases with the CG size while the curvature converges to the imposed one. Thus the strain energy calculated by CG is increasing with the CG size. This is questioning for the CG torques calculations. One explanation could be the presence of a divergence free torque field deriving from a curl. In fact this filed could be added or subtracted from the torques without impacting the volumic torques balance equation as it only depends on $div(\mathbf{m})$. An other problem identified with this expression

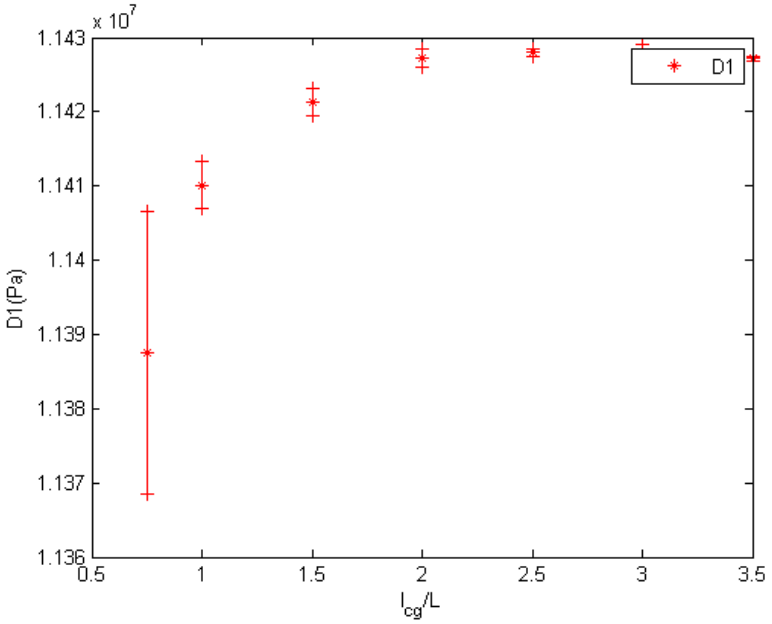

FIGURE 4.2 – Evolution of the mean of D1 depending on the coarse graining length for the square lattice and standard deviation.

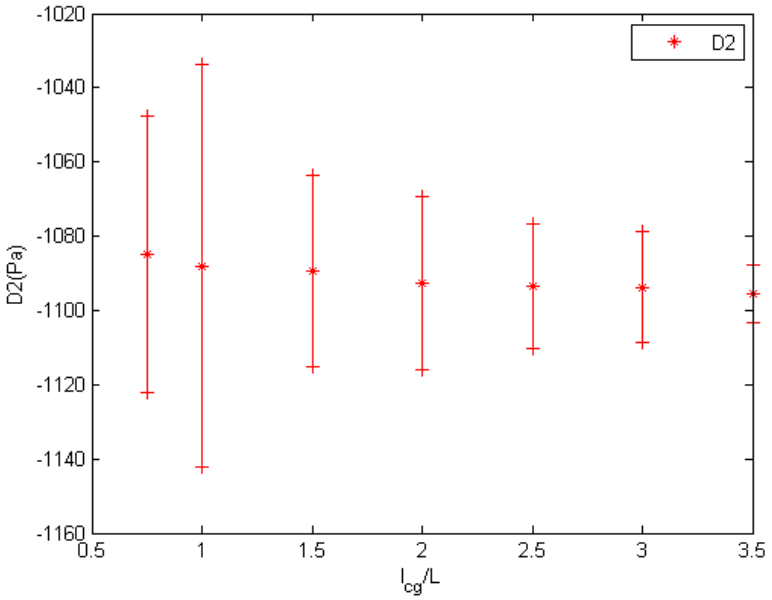

FIGURE 4.3 – Evolution of the mean of D2 depending on the coarse graining length for the square lattice and standard deviation.

of the CG torques is the non compatibility between CG and FE loads at the border of the CG area.

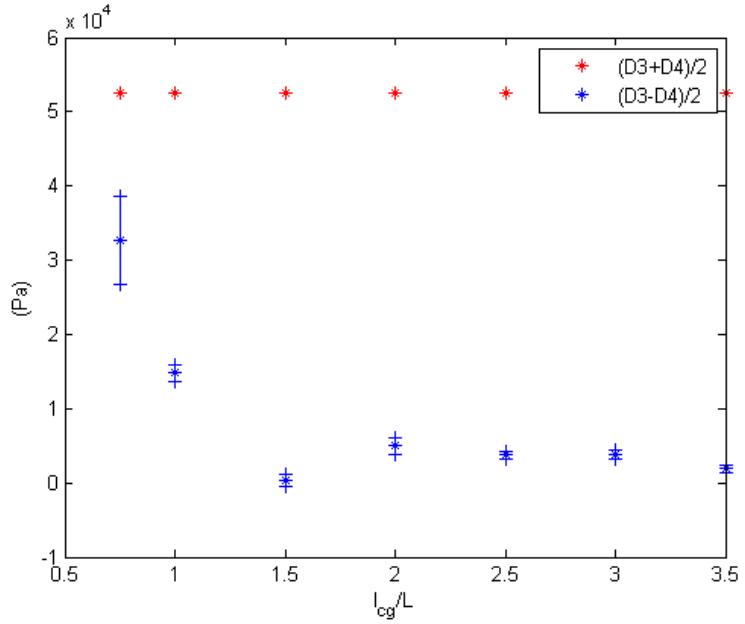

FIGURE 4.4 – Evolution of the mean of D3 and D4 depending on the coarse graining length for the square lattice and standard deviation.

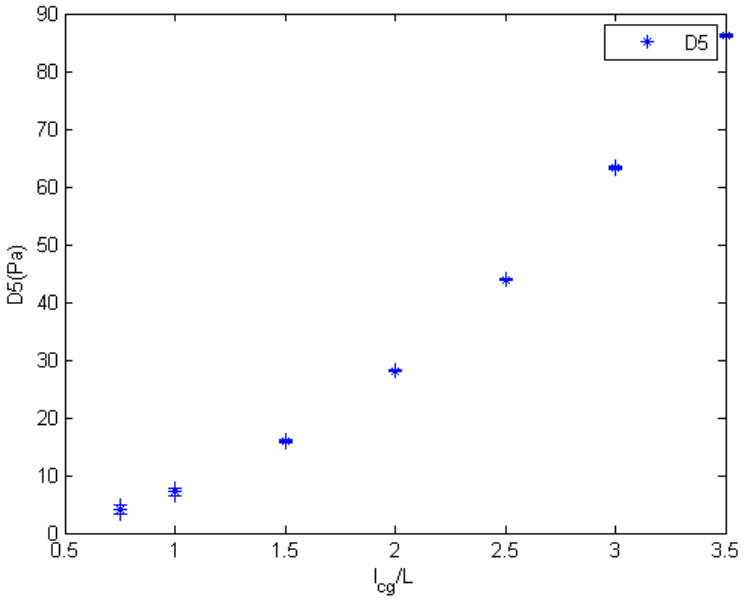

FIGURE 4.5 – Evolution of the mean of D5 depending on the coarse graining length for the square lattice and standard deviation.

4.6.2 Cosserat Coarse Grained Strain Energy :

As the CG strain energy increases with the CG length while it should converge, the divergent term will be identified form the CG strain energy expression. The energy should be conserved between the micro and the GC, The micro strain energy can be identified to isolate the problematic term.

$$
\begin{aligned}
2E_{strain} &= \int_\Omega \sum_{\alpha=1}^{2} \Big(\sum_{\beta=1}^{2} \sigma_{\alpha\beta} e_{\alpha\beta} + m_\alpha k_\alpha \Big) && (4.45)\\
&= \int_\Omega \sum_{\alpha=1}^{2} \Big(\sum_{\beta=1}^{2} \sigma_{\alpha\beta} \big(\frac{\partial u_\alpha}{\partial r_\beta} + \varepsilon_{\alpha\beta}\theta \big) + m_\alpha \frac{\partial \theta}{\partial r_\alpha} \Big) && (4.46)\\
&= \int_{\partial\Omega} \sum_{\alpha=1}^{2} \big(\sum_{\beta=1}^{2} \sigma_{\alpha\beta} u_\alpha + m_\alpha \theta \big)\mathbf{n} - \int_\Omega \sum_{\alpha=1}^{2} \Big(\sum_{\beta=1}^{2} \big(\frac{\partial \sigma_{\alpha\beta}}{\partial r_\beta} u_\alpha - \varepsilon_{\alpha\beta}\sigma_{\alpha\beta}\theta \big) \\
&\quad + \frac{\partial m_\alpha}{\partial r_\alpha}\theta \Big) && (4.47)\\
&= -\int_\Omega \sum_{\alpha=1}^{2} \Big(\sum_{\beta=1}^{2} \big(\frac{\partial \sigma_{\alpha\beta}}{\partial r_\beta} u_\alpha - \varepsilon_{\alpha\beta}\sigma_{\alpha\beta}\theta \big) + \frac{\partial m_\alpha}{\partial r_\alpha}\theta \Big) && (4.48)
\end{aligned}
$$

if we take the case of zero external work.
And from the previous identification of CG stresses and torques we have :

$$\frac{\partial \sigma_{\alpha\beta}}{\partial r_\beta} = -\sum_{ij} \sum_{\gamma=1}^{3} K^{ij}_{\alpha\gamma} q^j_\gamma \Phi^i \tag{4.49}$$

$$\frac{\partial m_\alpha}{\partial r_\alpha} = -\Big(\sum_{ij} \sum_{\gamma=1}^{3} \varepsilon_{\phi\xi} (r^i_\phi - r_\phi) K^{ij}_{\xi\gamma} q^j_\gamma \Phi^i + \sum_{ij} \sum_{\gamma=1}^{3} K^{ij}_{\theta\gamma} q^j_\gamma \Phi^i \Big) + \varepsilon_{\phi\xi}\sigma_{\phi\xi} \tag{4.50}$$

And thus :

$$
\begin{aligned}
2E_{strain} &= -\int_\Omega \sum_{\alpha=1}^{2} \Big(\sum_{\beta=1}^{2} \big(\frac{\partial \sigma_{\alpha\beta}}{\partial r_\beta} u_\alpha - \varepsilon_{\alpha\beta}\sigma_{\alpha\beta}\theta \big) + \frac{\partial m_\alpha}{\partial r_\alpha}\theta \Big) && (4.51)\\
&= \int_\Omega \sum_{ij} \sum_{\alpha=1}^{2} \sum_{\gamma=1}^{3} \Big(K^{ij}_{\alpha\gamma} q^j_\gamma \Phi^i u_\alpha + \varepsilon_{\phi\xi} (r^i_\phi - r_\phi) K^{ij}_{\xi\gamma} q^j_\gamma \Phi^i \theta + K^{ij}_{\theta\gamma} q^j_\gamma \Phi^i \theta \Big) && (4.52)
\end{aligned}
$$

It can be chosen :

$$u_\alpha = q^i_\alpha + \tilde{u}^i_\alpha \quad ; \quad \alpha = \{1,2\} \tag{4.53}$$

$$\theta = \theta^i + \tilde{\theta}^i \tag{4.54}$$

with $\tilde{u}^i$ and $\tilde{\theta}^i$ the fluctuations of the nodal dofs relatively to the CG dofs.

$$2E_{strain} = \int_\Omega \sum_{ij} \sum_{\alpha=1}^{2} \sum_{\gamma=1}^{3} \left(K^{ij}_{\alpha\gamma} q^j_\gamma \Phi^i u_\alpha + \varepsilon_{\phi\xi}(r^i_\phi - r_\phi) K^{ij}_{\xi\gamma} q^j_\gamma \Phi^i \theta + K^{ij}_{\theta\gamma} q^j_\gamma \Phi^i \theta \right) \quad (4.55)$$

$$= \int_\Omega \sum_{ij} \sum_{\alpha=1}^{2} \sum_{\gamma=1}^{3} \left(K^{ij}_{\alpha\gamma} q^j_\gamma \Phi^i (q^i_\alpha + \tilde{u}^i_\alpha) + \varepsilon_{\phi\xi}(r^i_\phi - r_\phi) K^{ij}_{\xi\gamma} q^j_\gamma \Phi^i (\theta^i + \tilde{\theta}^i) \right.$$
$$\left. + K^{ij}_{\theta\gamma} q^j_\gamma \Phi^i (\theta^i + \tilde{\theta}^i) \right) \quad (4.56)$$

$$= \int_\Omega \sum_{ij} \sum_{\alpha=1}^{3} \sum_{\gamma=1}^{3} \left(q^i_\alpha K^{ij}_{\alpha\gamma} q^j_\gamma \Phi^i + \varepsilon_{\phi\xi}(r^i_\phi - r_\phi) K^{ij}_{\xi\gamma} q^j_\gamma \Phi^i (\theta^i + \tilde{\theta}^i) \right.$$
$$\left. + \tilde{q}^i_\alpha K^{ij}_{\alpha\gamma} q^j_\gamma \Phi^i \right) \quad (4.57)$$

The CG of the microscopic energy can be identified as :$\sum_{ij} \sum_{\alpha=1}^{3} \sum_{\gamma=1}^{3} q^i_\alpha K^{ij}_{\alpha\gamma} q^j_\gamma$. A term corresponding to heat creation due to the fluctuation of the nodal dofs relatively to the coarse grained dofs $\sum_{ij} \sum_{\alpha=1}^{3} \sum_{\gamma=1}^{3} \tilde{q}^i_\alpha K^{ij}_{\alpha\gamma} q^j_\gamma \Phi^i$. A last term that was suspected to produce the increase of the energy with the increase of the CG length is : $\int_\Omega \sum_{ij} \sum_{\alpha=1}^{3} \sum_{\gamma=1}^{3} \varepsilon_{\phi\xi}(r^i_\phi - r_\phi) K^{ij}_{\xi\gamma} q^j_\gamma \Phi^i (\theta^i + \tilde{\theta}^i)$

It can be showed that this term is null :

$$\int_\Omega \sum_{ij} \sum_{\alpha=1}^{3} \sum_{\gamma=1}^{3} \varepsilon_{\phi\xi}(r^i_\phi - r_\phi) K^{ij}_{\xi\gamma} q^j_\gamma \Phi^i (\theta^i + \tilde{\theta}^i) d\mathbf{r} \quad (4.58)$$

$$= \int_\Omega \varepsilon_{\phi\xi} \sum_i G_\phi(\mathbf{r} - \mathbf{r}^i) H_\xi(\mathbf{r}^i) d\mathbf{r} \quad (4.59)$$

With $G_\phi(\mathbf{r} - \mathbf{r}^i) = (r_\phi - \widehat{r}^i_\phi + \widehat{r}^i_\phi - r^i_\phi)\Phi(\mathbf{r} - \widehat{\mathbf{r}}^i) \simeq (r_\phi - \widehat{r}^i_\phi)\Phi(\mathbf{r} - \widehat{\mathbf{r}}^i)$ if $\mathbf{r}^i - \widehat{\mathbf{r}}^i$ is neglected and $H_\xi(\mathbf{r}) = \sum_{\tilde{i}j} \delta(\mathbf{r} - \widehat{\mathbf{r}}^{\tilde{i}}) K^{\tilde{i}j}_{\xi\gamma} q^j_\gamma (\theta^{\tilde{i}} + \tilde{\theta}^{\tilde{i}})$. Noting $*$ the convolution product one can obtain :

$$\int_\Omega \varepsilon_{\phi\xi} \sum_i G_\phi(\mathbf{r} - \widehat{\mathbf{r}}^i) H_\xi(\widehat{\mathbf{r}}^i) d\mathbf{r} = \int_\Omega \varepsilon_{\phi\xi} G_\phi(\mathbf{r}) * H_\xi(\mathbf{r}) d\mathbf{r} = \int_\Omega \Gamma(\mathbf{r}) d\mathbf{r} \quad (4.60)$$

If we note $\Gamma(\mathbf{k})$ as being the Fourier transform of $\Gamma(\mathbf{r})$, then :

$$\Gamma(\mathbf{k}) = \int_{\mathbf{k}} \Gamma(\mathbf{r}) e^{2i\pi \mathbf{r}.\mathbf{k}} d\mathbf{r} \quad (4.61)$$

Thus :

$$\int_\Omega \Gamma(\mathbf{r}) d\mathbf{r} = \Gamma(\mathbf{k} = \mathbf{0}) \quad (4.62)$$

It can also be written that :

$$\Gamma(\mathbf{k}) = \varepsilon_{\phi\xi} G_\phi(\mathbf{k}) H_\xi(\mathbf{k}) \tag{4.63}$$

With $G_\phi(\mathbf{k})$ and $H_\xi(\mathbf{k})$ the respective Fourier transform of $G_\phi(\mathbf{r})$ and $H_\xi(\mathbf{r})$ More over :

$$G_\phi(\mathbf{k}) = \int_\Omega G_\phi(\mathbf{r}) e^{2i\pi \mathbf{r}.\mathbf{k}} d\mathbf{r} \tag{4.64}$$

$$= \int_\Omega r_\phi \Phi(\mathbf{r}) e^{2i\pi \mathbf{r}.\mathbf{k}} d\mathbf{r} \tag{4.65}$$

$$= \frac{-1}{2i\pi} \int_\Omega \frac{\partial}{\partial k_\phi} (\Phi(\mathbf{r}) e^{2i\pi \mathbf{r}.\mathbf{k}}) d\mathbf{r} \tag{4.66}$$

$$= \frac{-1}{2i\pi} \frac{\partial}{\partial k_\phi} (\Phi(\mathbf{k})) \tag{4.67}$$

And because :

$$\Phi(\mathbf{k}) = \int_\Omega e^{-\frac{\| \mathbf{r} \|^2}{2 l_{cg}^2}} e^{2i\pi \mathbf{r}.\mathbf{k}} d\mathbf{r} = e^{-\frac{l_{cg}^2 \| \mathbf{k} \|^2}{2}} \tag{4.68}$$

Then :

$$G_\phi(\mathbf{k}) = \frac{-l_{cg}^2}{i\pi} k_\phi \Phi(\mathbf{k}) \tag{4.69}$$

And finally :

$$\Gamma(\mathbf{k}) = \varepsilon_{\phi\xi} \frac{-1}{2i\pi} k_\phi \Phi(\mathbf{k}) H_\xi(\mathbf{k}) \tag{4.70}$$

$$\Gamma(\mathbf{k} = \mathbf{0}) = 0 \tag{4.71}$$

We conclude that the diverging term is indeed a boundary condition term.

4.6.3 Modifying the CG Torques

The term at the origin of the increase of the torques as been identified in the torque expression as $\sum_{ij\neq i}^{N} \sum_{\varphi\xi}^{n} \sum_{\gamma=1}^{n+m} \varepsilon_{\varphi\xi} (r_\varphi^i - r_\varphi) K_{\xi\gamma}^{ij} q_\gamma^j \widehat{r}_\beta^{ji} \int_0^1 \Phi(\mathbf{r} - \widehat{\mathbf{r}}^i + s\widehat{\mathbf{r}}^{ji}) ds$, it can be tempting to suppress it but as it is not divergence free, it would unbalance the volumic torque balance equation. Removing it would lead to the inability to identify the anti-symmetric part of the stress in the torque balance expression. However removing the problematic term in the torque expression leads to converging torques with the CG size, modulus corresponding to the literature and equilibrium between the CG and FE border loads. The figure.4.6 shows the evolution of the bending modulus with the CG length.

An other solution to modify the torques in order to have a converging solution with the CG length is to identify the difference between the CG border Torques and the corresponding FE torques. The CG torque is then fitted to suppress the difference. The difference

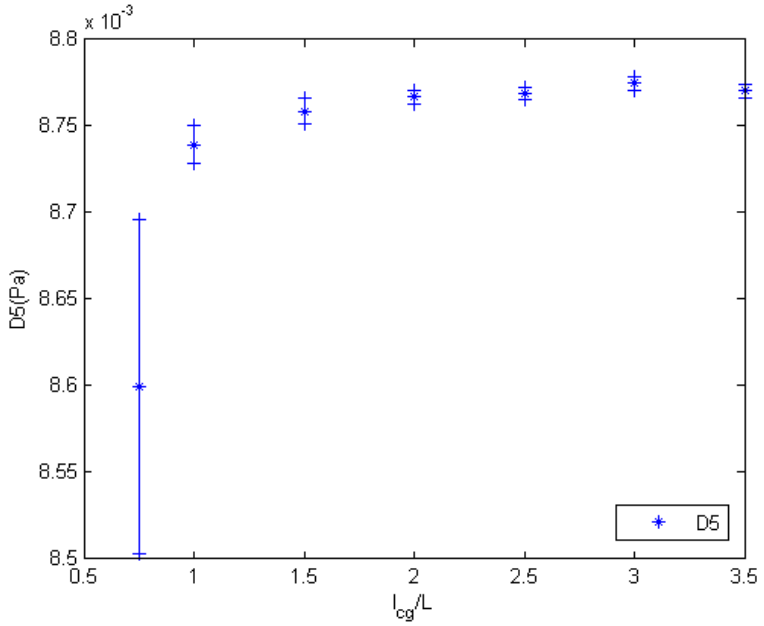

FIGURE 4.6 – Evolution of the mean of D5 and standard deviation obtained with the modified torque with subtracted lever arm depending on the coarse graining length for the square lattice.

can be simply subtracted in the volume as it's divergence remain null. In the case of the square lattice it can be done easily in the case where each CG point correspond to a FE node. The difference can be calculated a each point and subtracted in the volume. For example in the case of Mx the difference can be calculated at each point of the right border of the CG area then subtracted at each point of the corresponding line. The resulting evolution of $D5$ elastic modulus for fitted torques on a square lattice is shown in figure.4.7a. This method gives converging elastic modulus with the CG length but gives results 2 order of magnitude higher than the ones found in literature.

It has also been tried to identify a field resulting form a curl using a finite difference method to respect the volumic torques balance equation and respecting the transmitted forces and torques in resultants at the boundary of the observed domain. If the correction of torques is searched as a curl of a field of scalar φ then the volumic balance of torques is preserved :

$$div(\mathbf{m}+\mathbf{curl}(\varphi)) = \varepsilon_{\alpha\beta}\sigma_{\alpha\beta} \tag{4.72}$$

$$div(\mathbf{m}) = \varepsilon_{\alpha\beta}\sigma_{\alpha\beta} \tag{4.73}$$

The system of equations is :

$$\widehat{\tilde{\boldsymbol{\sigma}}} = \widehat{\mathbf{D}}\widehat{\boldsymbol{e}} \tag{4.74}$$

$$\sum_{bcY^+} m_x + \frac{\partial\varphi}{\partial r_y} = \sum_{bcX^+} M_{ef} D^{cg} \tag{4.75}$$

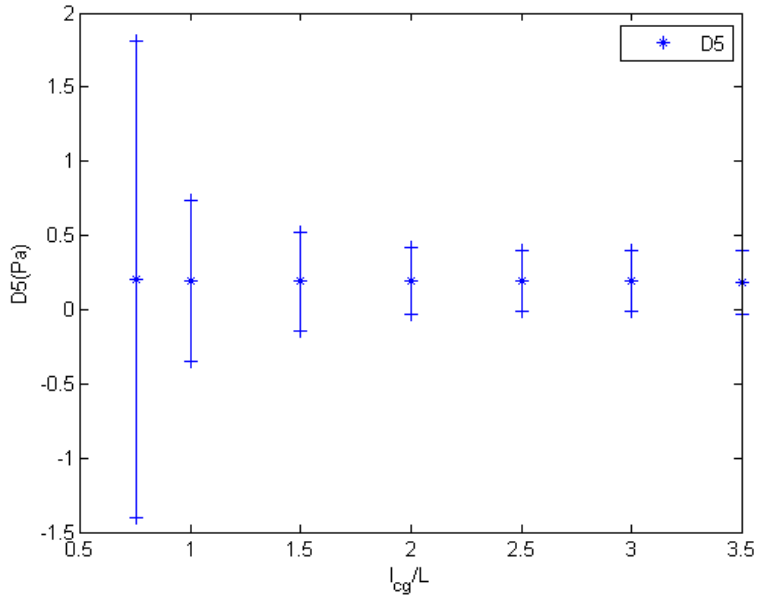

(a) Evolution of $D5$ elastic modulus for fitted torques on a square lattice.

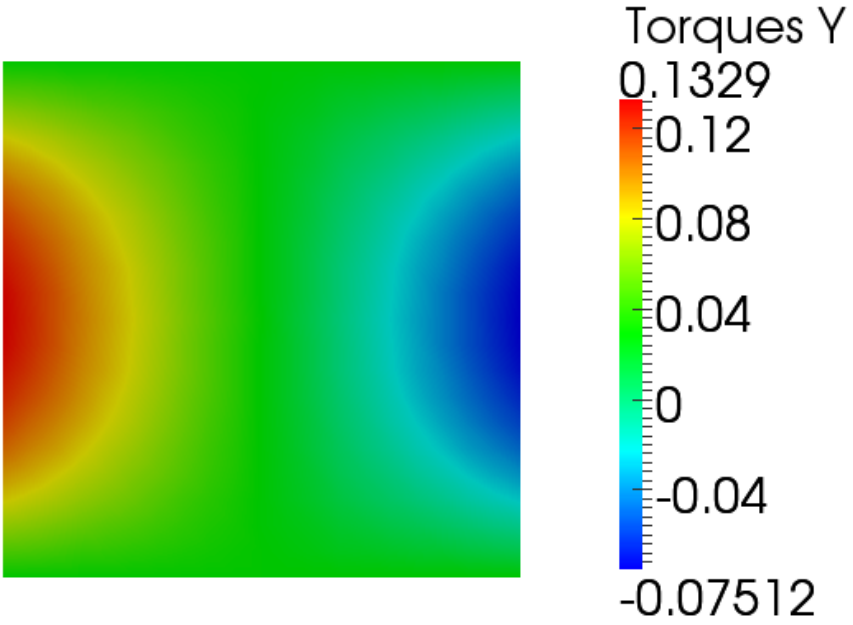

(b) Field of fitted torques m_y for a simulation where k_y is imposed at the border.

FIGURE 4.7 – Results of the fitting method to modify the CG torques.

$$\sum_{bcY^-} m_x + \frac{\partial \varphi}{\partial r_y} = \sum_{bcY^-} M_{ef} D^{cg} \tag{4.76}$$

$$\sum_{bcX^+} m_y - \frac{\partial \varphi}{\partial r_x} = \sum_{bcX^+} M_{ef} D^{cg} \tag{4.77}$$

$$\sum_{bcX^-} m_y - \frac{\partial \varphi}{\partial r_x} = \sum_{bcX^-} M_{ef} D^{cg} \tag{4.78}$$

with the modified stress vector :$\widehat{\tilde{\boldsymbol{\sigma}}} = \{\sigma_{xx}, \sigma_{yy}, \sigma_{xy}, \sigma_{yx}, m_x + \frac{\partial \varphi}{\partial r_y}, m_y - \frac{\partial \varphi}{\partial r_x}\}$. Here $\sum_{bcY^+}$ is used to denote the sum over all the nodes sitting on the border Y^+ of the CG domain and D^{cg} is the length of the side of the CG domain.

The system can be written as :

$$\mathbf{A}.\widehat{\tilde{\boldsymbol{\sigma}}} + \mathbf{B}.\boldsymbol{\varphi} = \mathbf{C}.\widehat{D} + \mathbf{M_{ef}} \tag{4.79}$$

with $\boldsymbol{\varphi}$ a vector containing the values of φ for each CG point and $\mathbf{M_{ef}}$ containing the resulting Finite element momentum on the borders. The spatial derivatives are calculated using centered finite difference method in the bulk and forward and backward difference on the borders. A field of modified m_y for a simulation where $k_y = 1$ is imposed on the border is shown in figure.4.8b.This method gives elastic moduli close to the one found in literature but the resulting torques field are non uniform when it is expected to be.

4.6.4 Application to QP beam lattice

In order to demonstrate the real advantage of this CG method to obtain continuous medium properties of FE model it will be applied to quasi-periodic beam lattices. The two beam lattices presented here are the same as in the previous chapter i.e a penrose kite& dart and a octhohedric. The spatial dispersion of elastic moduli is shown in figure.4.9 for the octhohedric lattice. The evolution of the CG elastic muduli are presented in the figure.4.10.

The spatial dispersion elastic moduli is shown in figure.4.11 for the Kyte & Dart. The evolution of the CG elastic muduli are presented in the figure.4.12.

The CG method thus allows to obtain a continuous non homogeneous material. The influence of sub structures is preserved. It can be seen in figure.4.13 the evolution of D1 elastic modulus for different CG length in the Cosserat continuous of the kyte & dart Penrose lattice.

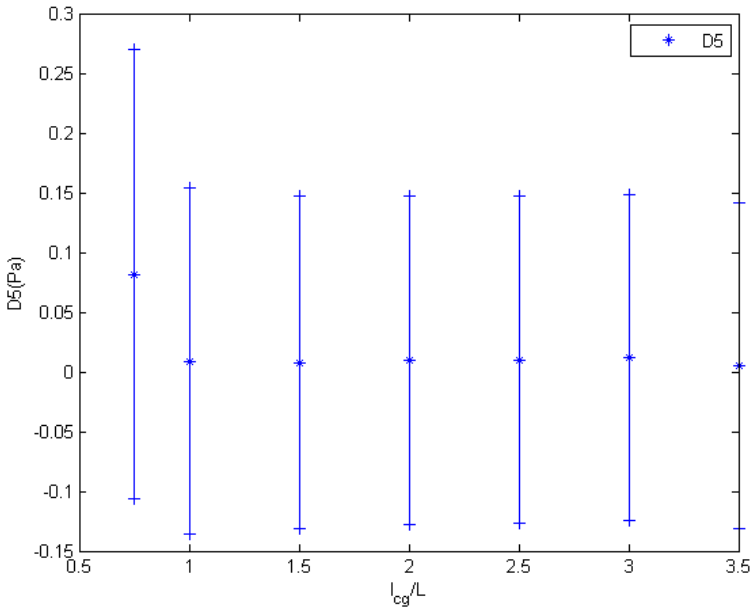

(a) Field of modified torques m_y with curl field for a simulation where k_y is imposed at the border.

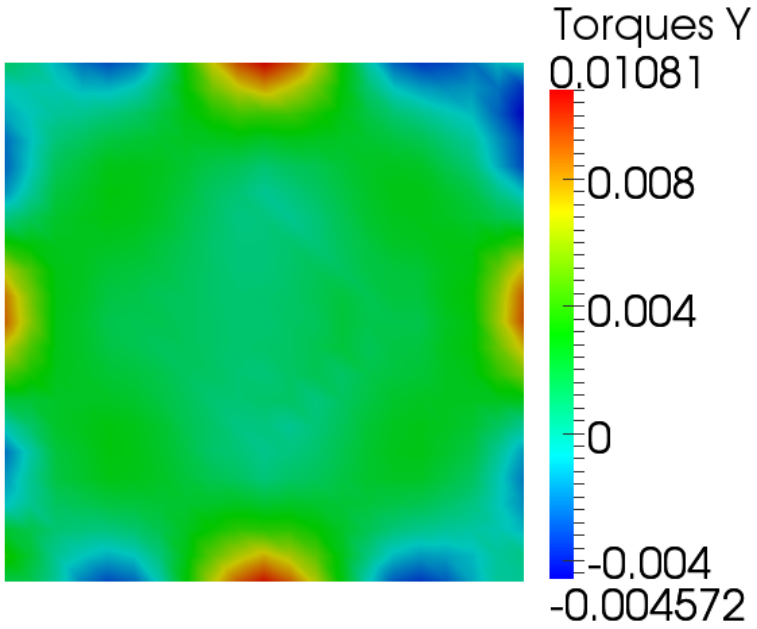

(b) Field of modified m_y with curl field for a simulation where k_y is imposed at the border.

FIGURE 4.8 – Results of the fitting method to modify the CG torques.

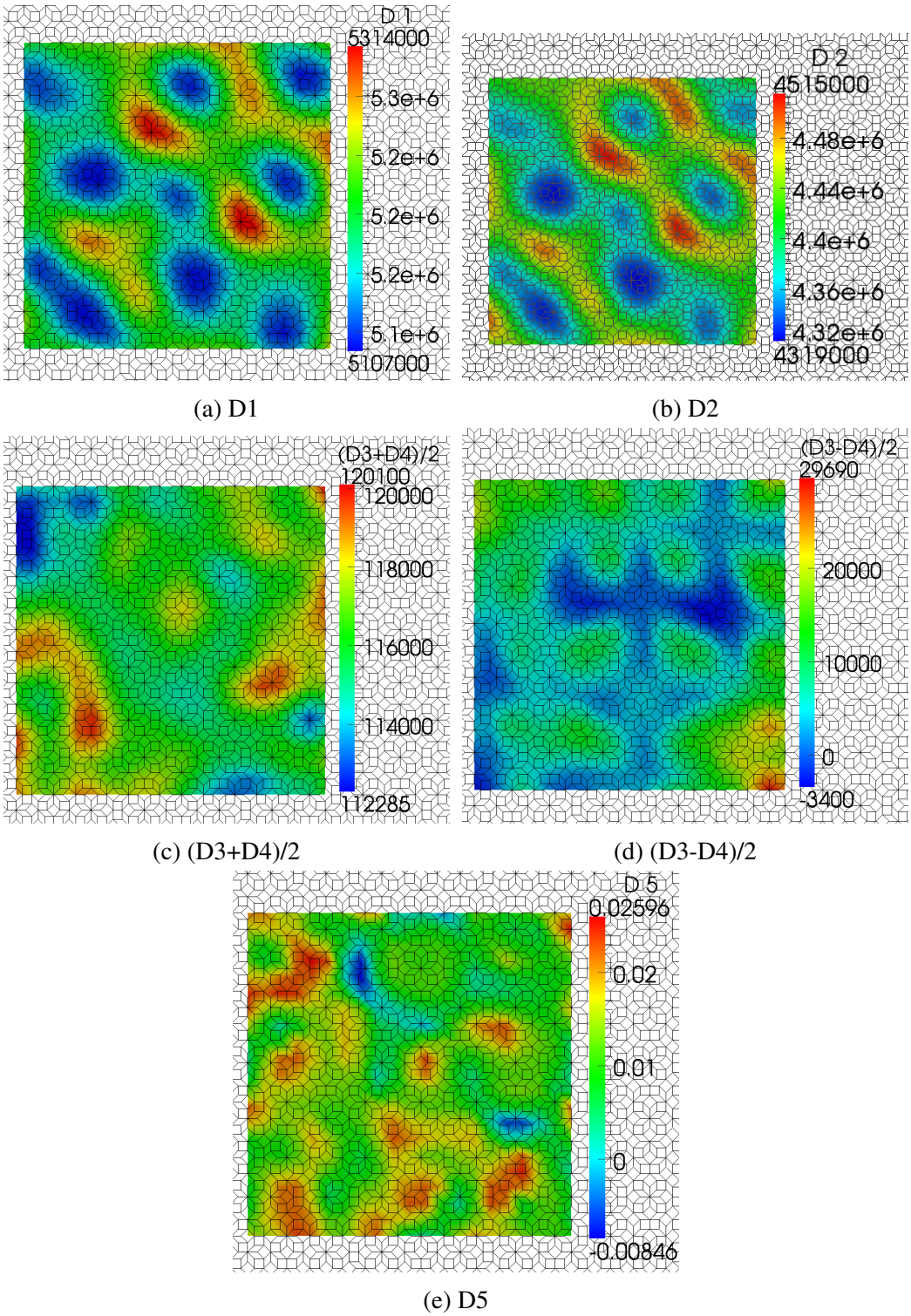

(a) D1 (b) D2

(c) (D3+D4)/2 (d) (D3-D4)/2

(e) D5

FIGURE 4.9 – Moduli of the CG of Octogonal mesh at $lg = 3L$ superposed to the FE lattice.

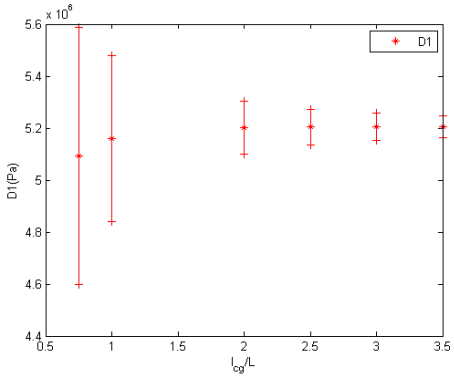

(a) Evolution of the mean of D1 and standard deviation depending on the coarse graining length for the Octogonal Penrose lattice.

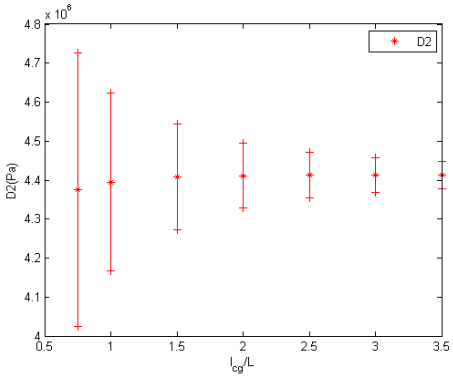

(b) Evolution of the mean of D2 and standard deviation depending on the coarse graining length for the Octogonal Penrose lattice.

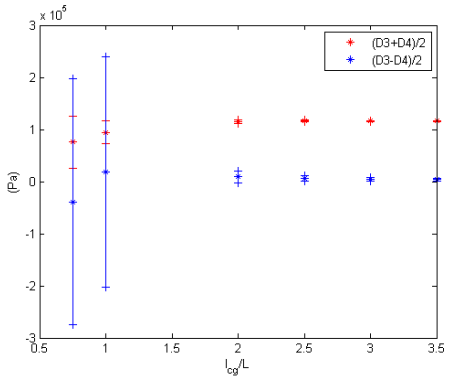

(c) Evolution of the mean of D3 and D4 and standard deviations depending on the coarse graining length for the Octogonal Penrose lattice.

FIGURE 4.10 – Evolution of the mean of elastic moduli depending on the coarse graining length for the Octogonal Penrose lattice.

4.7 Discussion and Conclusion

In this chapter an new CG strategy allowing for the identification of an equivalent heterogeneous continuous medium form FE beam lattice has been developed and applied to periodic and quasi periodic beam lattice. It has been shown to give consistent results in comparison to the literature for periodic beam lattices where classical homogenization has been applied. This method is especially useful for quasi periodic structures as most of classical homogenization method can only be applied on periodic configuration. This method also allows to look at the meta-material at different scales thus creating different continuous approximation depending of the description scale needed. It seems from the previous chapters that sub structures play a preponderant role in vibration

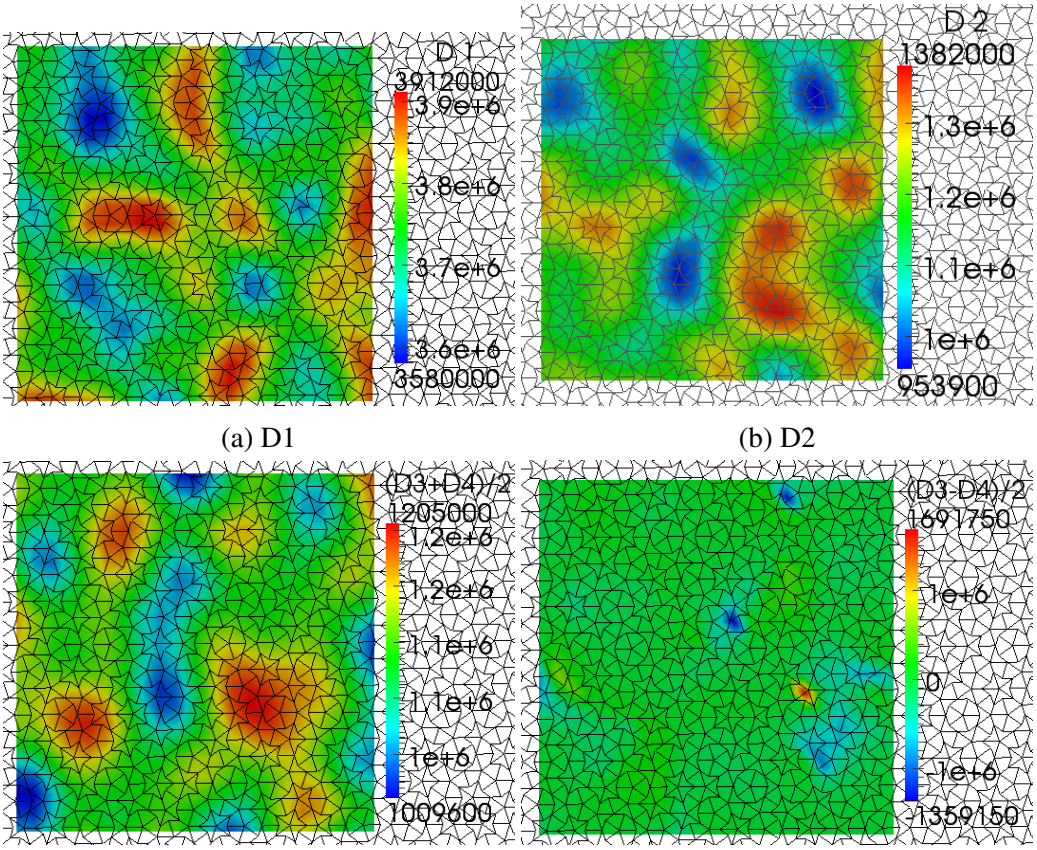

(a) D1 (b) D2

(c) (D3+D4)/2 (d) (D3-D4)/2

FIGURE 4.11 – Moduli of the CG of Octogonal mesh at $lg = 3L$ superposed to the FE lattice.

and crack propagation for such lattices, therefore a scale where these structures remain distinguishable is needed to account for influence while creating a continuous medium. Although the classical method to identify strain and stress has easily be transposed to FE (instead of discrete point wise models), the rotation and torques remain difficult to upscale.

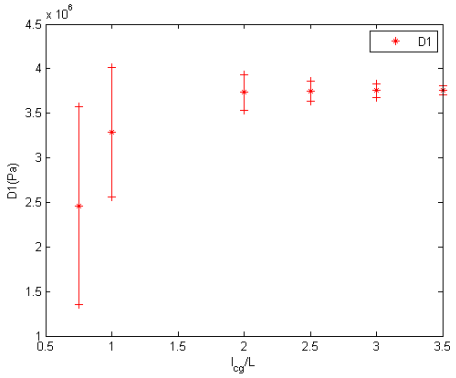

(a) Evolution of the mean of D1 and standard deviation depending on the coarse graining length for the KD lattice.

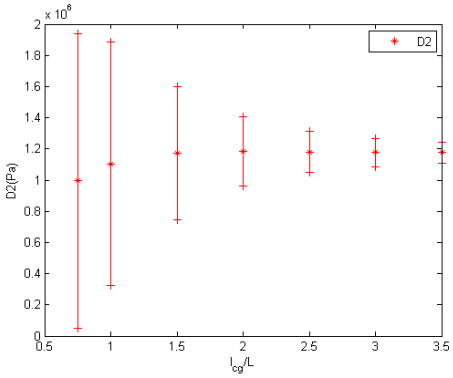

(b) Evolution of the mean of D2 and standard deviation depending on the coarse graining length for the KD lattice.

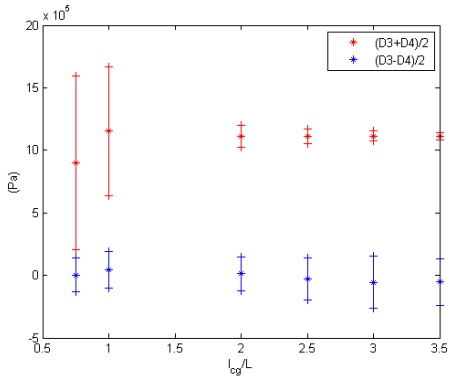

(c) Evolution of the mean of D3 and D4 and standard deviations depending on the coarse graining length for the KD lattice.

FIGURE 4.12 – Evolution of the mean of elastic moduli depending on the coarse graining length for the KD lattice.

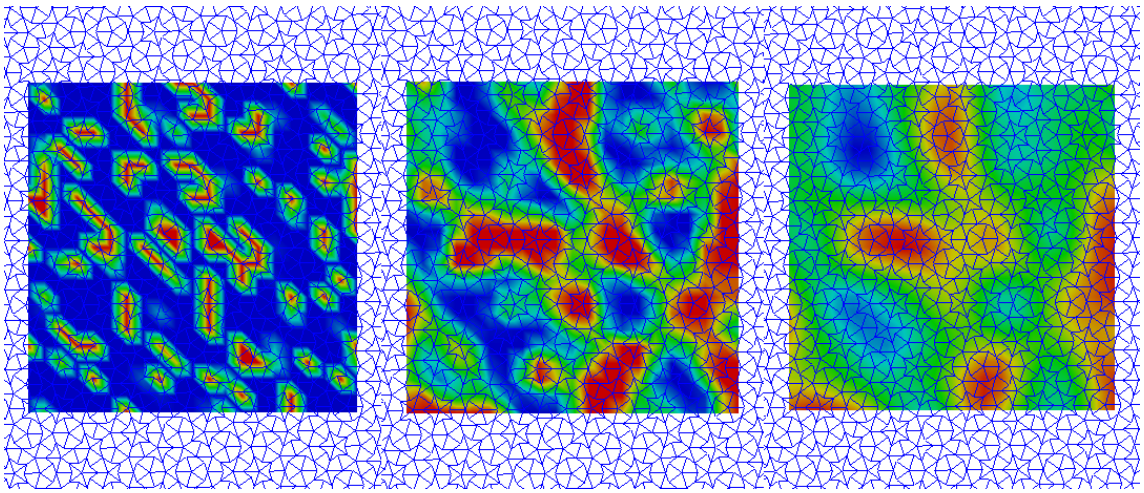

FIGURE 4.13 – spacial distribution of D1 in kyte & dart for different CG length (for left to right) $1L$, $2.5L$ and $3.5L$.

Summary and perspectives

Summary

Quasi periodic Euler Bernoulli beam lattices have been studied, their vibration and fracture propagation properties have been analyzed using numerical methods to deal with the specific problems that arise from their quasi periodic structure.

The KPM method has been applied to finite element model with success in order to reduce the calculation time needed to obtain VDOS and DSF of large QP beam lattices. The use of Voronoï decomposition allow to decompose the vibrationnal response along transverse and longitudinal waves. This method can be applied to any lattices but still require the use of periodic boundary conditions. This limits the range of application for the QP lattices to the ones that have periodic approximation. Quasi periodic beam lattices exhibit the peculiar vibration properties already seen in quasi crystals (i.e band gaps and mode localization on sub structures) while having more parameters that can be adjusted in order to obtain the desired properties and should be considered to create interesting new meta-materials at macroscopic scale.

A Static FE beam model has been developed and implemented in order to study the crack propagation in beam lattices. The simulations results seems in agreement with the experiments even if the experiments are unstable. From an analysis of the energy dissipation of the crack propagation in beam lattices it seems that Kyte & Dart QP lattices are good candidate to create new meta-materials that are able to dissipate more energy during crack propagation than their periodic counterparts.
A dynamic FE beam model with varying time step has been developed and implemented in order to study the crack propagation behavior of QP beam lattices. Dynamic crack opening simulations are performed to study the crack propagation under dynamic loading. the simulations allow the comparison of the crack behavior of several lattice and show that slender Kite & Dart have a good ability to resist to crack propagation. The model still needs to be better validated with dynamic experiments correctly instrumented to grasp the failure in action. With the increase use of cellular materials in many mechanical domain, Kite & Dart QP lattices could be needed in case where periodic lattices fails to resist to mechanical loads.

A coarse graining method has been developed to create equivalent continuous

medium while preserving the non homogeneity needed to correctly describe the complex behavior of QP lattices. Displacement, strains and stresses are identified for a Cosserat medium from the assembled stiffness and mass matrix of the FE beam lattices.This allows to identify the elastic moduli of the Cosserat approximation for several CG length. Rotation , curvatures and torques are also defined. The torques rose question as it seems impossible to respect energy conservation between scales and torques equilibrium with the same torque expression. All CG quantities depend on the CG length and converges to a finite values when this length increases. In order to get this result the torque expression had to be modified and no longer satisfies balance equations. More work is still required in order to fully solved the problem.

Perspectives

The methods presented in this thesis can be applied to study a wide range of beam lattices in different domains of interest. The codes developed can be modified to improve the models especially for the dynamic crack propagation.

The Coarse graining method can be adapted to be used on any FE model, even areal and volumic continuous or discrete models in order to perform scaling. It's main point of interest is the analysis of heterogeneous non periodic samples.

A direct continuation of the work done in this thesis could be the use of the coarse graining method over crack propagation simulations in QP lattices to follow the change of CG stresses and deformations in order to investigate a way to create a damage law that could be use in a continuum model. This model could be used to simulate crack propagation in the continuous medium equivalent to the quasi periodic beam lattice.

Dynamic experiments are to be performed at Ecole Centrale de Nantes with the use of high speed cameras and appropriate dynamic loading equipment in order to have better experimental results to validate the dynamic FE model.

Appendices

Annexe A

Periodic structure analytical solution

The dynamic equilibrium written on one node for the square lattice once the wave solution is assumed is :

$$\left(\begin{bmatrix} 2\frac{ES(1-\cos(qxL))}{L}+24\frac{EI(1-\cos(qyL))}{L^3} & 0 & \frac{-12iEI\sin(qyL)}{L^2} \\ 0 & 24\frac{EI(1-\cos(qxL))}{L^3}+2\frac{ES(1-\cos(qyL))}{L} & \frac{12iEI\sin(qxL)}{L^2} \\ \frac{12iEI\sin(qyL)}{L^2} & \frac{-12iEI\sin(qxL)}{L^2} & 4\frac{EI(4+\cos(qxL)+\cos(qyL))}{L} \end{bmatrix}\right.$$

$$\left. -\omega^2\begin{bmatrix} 1/3\rho SL(2+\cos(qxL))+\frac{26\rho SL}{35}+\frac{9\rho SL\cos(qyL)}{35} & 0 & \frac{13i}{210}L^2\rho S\sin(qyL) \\ 0 & 1/3\rho SL(2+\cos(qyL))+\frac{26\rho SL}{35}+\frac{9\rho SL\cos(qxL)}{35} & -\frac{13i}{210}L^2\rho S\sin(qxL) \\ -\frac{13i}{210}L^2\rho S\sin(qyL) & \frac{13i}{210}L^2\rho S\sin(qxL) & \frac{4L^3\rho S}{105}-\frac{\cos(qxL)L^3\rho S}{70}-\frac{\cos(qyL)L^3\rho S}{70} \end{bmatrix}\right)\{d\}=\{0\}$$

The solution of this problem can by analytically solved, thus giving the dispersion law.

Annexe B

Coarse Graining

B.1 CG Displacement

In order to Calculate the CG displacements from the CG velocities one must integrate the velocities versus the time.

$$\begin{aligned} u_\alpha^{cg}(\mathbf{r},t) = \int_0^t v^{cg}(\mathbf{r},t')dt' = \int_0^t \frac{p_\alpha^{cg}}{\rho_{cg}} &= \int_0^t \sum_i^N \dot{w}_\alpha^i \frac{\Phi^i}{\rho_{cg}} dt' \\ &= \sum_i^N w_\alpha^i \frac{\Phi^i}{\rho_{cg}} - \int_0^t \sum_i^N w_\alpha^i \frac{\partial}{\partial t'}\left(\frac{\Phi^i}{\rho_{cg}}\right) dt' \\ &= u_\alpha^l - \int_0^t \sum_i^N \frac{w_\alpha^i}{\rho_{cg}^2}\left(\frac{\partial \Phi^i}{\partial t'}\rho_{cg} - \frac{\partial \rho_{cg}}{\partial t'}\Phi^i\right) dt' \end{aligned} \tag{B.1}$$

The temporal derivative of the CG function Φ^i in Lagrangian coordinate is detailed :

Preliminary calculus :

In Lagrangian :

$$\begin{aligned} \frac{\partial \Phi^i}{\partial t'} = \sum_\beta \frac{\partial \Phi^i(\overrightarrow{d})}{\partial d_\beta} \cdot \frac{\partial d_\beta}{\partial t'} = \sum_\beta \frac{\partial \Phi(\overrightarrow{r} - \overrightarrow{r_m}^i)}{\partial r_\beta} \cdot \frac{\partial r_\beta}{\partial (r_\beta - r_{m\beta}^i)} \cdot \frac{\partial (r_\beta - r_{m\beta}^i)}{\partial t'} \\ = \sum_\beta \frac{\partial \Phi(\overrightarrow{r} - \overrightarrow{r_m}^i)}{\partial r_\beta} \cdot \frac{1}{\frac{\partial (r_\beta - r_{m\beta}^i)}{\partial r_\beta}} \cdot \frac{\partial (r_\beta - r_{m\beta}^i)}{\partial t'} = \sum_\beta \frac{\partial \Phi^i}{\partial r_\beta} \cdot (v_\beta^{cg} - \frac{\dot{w}_\beta^i}{m^i}) \end{aligned} \tag{B.2}$$

Using this result the following can be obtained :

$$u_\alpha^{cg}(\overrightarrow{r},t) = u_\alpha^l - \int_0^t \sum_{ij\beta} \frac{w_\alpha^i}{\rho_{cg}^2}\Big((v_\beta^{cg} - \frac{\dot{w}_\beta^i}{m^i})\frac{\partial\Phi^i}{\partial r_\beta}.\rho_{cg} - m^j.(v_\beta^{cg} - \frac{\dot{w}_\beta^j}{m^j})\frac{\partial\Phi^j}{\partial r_\beta}.\Phi^i\Big)dt' \tag{B.3}$$

with $u_\alpha^l =$

$$\begin{aligned}
&= u_\alpha^l - \int_0^t \frac{1}{\rho_{cg}^2}\sum_\beta\left(\sum_i w_\alpha^i.(v_\beta - v_{m\beta}^i)\frac{\partial\Phi^i}{\partial r_\beta}\rho_{cg} - \sum_j \rho_{cg}.u_\alpha^l.m^j.(v_\beta - v_{m\beta}^j)\frac{\partial\Phi^j}{\partial r_\beta}\right)dt' \\
&= u_\alpha^l - \int_0^t \frac{1}{\rho_{cg}}\sum_\beta\left(\sum_i w_\alpha^i.v_\beta\frac{\partial\Phi^i}{\partial r_\beta} - \sum_i w_\alpha^i.v_{m\beta}^i\frac{\partial\Phi^i}{\partial r_\beta} - \sum_j u_\alpha^l.m^j.v_\beta\frac{\partial\Phi^j}{\partial r_\beta} + \sum_j u_\alpha^l.m^j.v_{m\beta}^j\frac{\partial\Phi^j}{\partial r_\beta}\right)dt' \\
&= u_\alpha^l - \int_0^t \frac{1}{\rho_{cg}}\sum_\beta\left(v_\beta\frac{\partial\rho_{cg}.u_\alpha^l}{\partial r_\beta} - \sum_i M_u q_\alpha^i.v_{m\beta}^i\frac{\partial\Phi^i}{\partial r_\beta} - u_{l\alpha}.v_\beta.\frac{\partial\rho_{cg}}{\partial r_\beta} + u_\alpha^l\frac{\partial\rho_{cg}.v_\beta}{\partial r_\beta}\right)dt' \\
&= u_\alpha^l - \int_0^t \frac{1}{\rho_{cg}}\sum_\beta\left(v_\beta\left(\rho_{cg}.\frac{\partial u_\alpha^l}{\partial r_\beta} + \frac{\partial\rho_{cg}}{\partial r_\beta}.u_\alpha^l\right) - \sum_i w_\alpha^i.v_{m\beta}^i\frac{\partial\Phi^i}{\partial r_\beta} - u_{l\alpha}.v_\beta.\frac{\partial\rho_{cg}}{\partial r_\beta} + u_\alpha^l\left(\rho_{cg}.\frac{\partial v_\beta}{\partial r_\beta} + \frac{\partial\rho_{cg}}{\partial r_\beta}.v_\beta\right)\right)dt' \\
&= u_\alpha^l - \int_0^t \frac{1}{\rho_{cg}}\sum_\beta\frac{\partial}{\partial r_\beta}\left(v_\beta\rho_{cg}.u_\alpha^l - \sum_i w_\alpha^i.v_{m\beta}^i\Phi^i\right)dt' \\
&= u_\alpha^l - \int_0^t \frac{1}{\rho_{cg}}\sum_\beta\frac{\partial}{\partial r_\beta}\left(v_\beta^{cg}\rho_{cg}.u_\alpha^l - \sum_i m^i\frac{w_\alpha^i}{m^i}.\frac{\dot{w}_\beta^i}{m^i}\Phi^i\right)dt'
\end{aligned} \tag{B.4}$$

If we defined $\tilde{v}_\beta^i$ as the fluctuation of the nodal velocities relatively to the CG velocities, and $\tilde{u}_\beta^i$ as the fluctuation of the nodal displacements relatively to the CG displacements :

$$\tilde{v}_\beta^i = \frac{\dot{w}_\beta^i}{m^i} - v_\beta^{cg}; \tilde{u}_\beta^i = \frac{w_\beta^i}{m^i} - u_\beta^l \tag{B.5}$$

It can be obtained :

$$\begin{aligned}
u_\alpha^{cg}(\overrightarrow{r},t) &= u_\alpha^l - \int_0^t \frac{1}{\rho_{cg}}\sum_\beta\frac{\partial}{\partial r_\beta}\left(v_\beta^{cg}\rho_{cg}.u_\alpha^l - \sum_i \frac{w_\alpha^i}{m^i}.\frac{\dot{w}_\beta^i}{m^i}\Phi^i\right)dt' \\
&= u_\alpha^l + \int_0^t \frac{1}{\rho_{cg}}\sum_\beta\frac{\partial}{\partial r_\beta}\left(\sum_i m^i\tilde{v}_\beta^i\tilde{u}_\alpha^i\Phi^i\right)dt'
\end{aligned} \tag{B.6}$$

$\tilde{v}_\beta^i\tilde{u}_\alpha^i$ being of second order, the integral can be neglected. Thus $u_\alpha^{cg} = u_\alpha^l$

B.2 CG Rotation

$$\begin{aligned}\theta^{cg} &= \theta^{l} - \int_0^t \frac{1}{I_{cg}^2} \sum_{i\alpha\beta} \Bigg(\delta_{\alpha\beta}(v_\alpha^i - v_\alpha) M q_\beta^i \Phi^i I_{cg} + (\delta_{\alpha\beta}(r_\alpha^i - r_\alpha) M q_\beta^i + M q_\theta^i) \frac{\partial \Phi^i}{\partial t'} I_{cg} \\ &\qquad - (\delta_{\alpha\beta}(r_\alpha^i - r_\alpha) M q_\beta^i + M q_\theta^i) \frac{\partial I_{cg}}{\partial t'} \Phi^i \Bigg) \\ &= \theta^{l} - \int_0^t \frac{1}{I_{cg}^2} \sum_{i\alpha\beta} \Bigg(\delta_{\alpha\beta}(v_\alpha^i - v_\alpha) M q_\beta^i \Phi^i I_{cg} + \sum_\xi (\delta_{\alpha\beta}(r_\alpha^i - r_\alpha) M q_\beta^i + M q_\theta^i)(v_\xi - v m_\xi^i) \frac{\partial \Phi^i}{\partial r_\xi} I_{cg} \\ &\qquad - I_{cg} \theta^l \frac{\partial I_{cg}}{\partial t'} \Bigg)\end{aligned} \tag{B.7}$$

$$\begin{aligned}\theta^{cg} &= \theta^{l} - \int_0^t \frac{1}{I_{cg}^2} \sum_{i\alpha\beta} \Bigg(\delta_{\alpha\beta}(v_\alpha^i - v_\alpha) M q_\beta^i \Phi^i I_{cg} + \sum_\xi (\delta_{\alpha\beta}(r_\alpha^i - r_\alpha) M q_\beta^i + M q_\theta^i)(v_\xi - v m_\xi^i) \frac{\partial \Phi^i}{\partial r_\xi} I_{cg} \\ &\qquad - I_{cg} \theta^l \left(m^i \frac{\partial \|r^j - r\|^2}{\partial t'} \Phi^i + (m^i \|r^j - r\|^2 + I^i) \frac{\partial \Phi^i}{\partial t'} \right) \Bigg) \\ &= \theta^{l} - \int_0^t \frac{1}{I_{cg}} \sum_{i\alpha\beta} \Bigg(\delta_{\alpha\beta}(v_\alpha^i - v_\alpha) M q_\beta^i \Phi^i + \sum_\xi (\delta_{\alpha\beta}(r_\alpha^i - r_\alpha) M q_\beta^i + M q_\theta^i)(v_\xi - v m_\xi^i) \frac{\partial \Phi^i}{\partial r_\xi} \\ &\qquad - \sum_\xi \theta^l \left(m^i \frac{\partial \|r^j - r\|^2}{\partial t'} \Phi^i + (m^i \|r^j - r\|^2 + I^i)(v_\xi - v m_\xi^i) \frac{\partial \Phi^i}{\partial r_\xi} \right) \Bigg) \\ &= \theta^{l} - \int_0^t \frac{1}{I_{cg}} \sum_{i\alpha\beta} \Bigg(\delta_{\alpha\beta}(v_\alpha^i - v_\alpha) M q_\beta^i \Phi^i\end{aligned} \tag{B.8}$$

$$
\begin{aligned}
&+\sum_{\xi}\Big(\delta_{\alpha\beta}(r^i_\alpha - r_\alpha)Mq^i_\beta + Mq^i_\theta - \theta^l(m^i\|r^j-r\|^2+I^i)\Big)(v_\xi - vm^i_\xi)\frac{\partial\Phi^i}{\partial r_\xi} - \sum_{\xi}\theta^l\left(m^i\frac{\partial\|r^j-r\|^2}{\partial t'}\Phi^i\right)\Bigg) \\
&= \theta^l - \int_0^t \frac{1}{I_{cg}}\sum_{i\alpha\beta}\Bigg(\delta_{\alpha\beta}(v^i_\alpha - v_\alpha)Mq^i_\beta\Phi^i \\
&+\sum_{\xi}\Big((m^i\|r^j-r\|^2+I^i)(\tilde{\theta}^i+\theta^l) - \theta^l(m^i\|r^j-r\|^2+I^i)\Big)(v_\xi - vm^i_\xi)\frac{\partial\Phi^i}{\partial r_\xi} - \sum_{\xi}\theta^l\left(m^i\frac{\partial\|r^j-r\|^2}{\partial t'}\Phi^i\right)\Bigg) \\
&= \theta^l - \int_0^t \frac{1}{I_{cg}}\sum_{i\alpha\beta}\Bigg(\delta_{\alpha\beta}(v^i_\alpha - v_\alpha)Mq^i_\beta\Phi^i + \sum_{\xi}(m^i\|r^j-r\|^2+I^i)\tilde{\theta}^i\tilde{v^i_\xi}\frac{\partial\Phi^i}{\partial r_\xi} - \sum_{\xi}\theta^l\left(m^i\frac{\partial\|r^j-r\|^2}{\partial r_\xi}(v^i_\xi - v_\xi)\Phi^i\right)\Bigg)
\end{aligned}
\tag{B.9}
$$

$$
\begin{aligned}
&\sum_{i\alpha\beta\xi}(m^i\|r^j-r\|^2+I^i)\tilde{\theta}^i\tilde{v^i_\xi}\frac{\partial\Phi^i}{\partial r_\xi} \\
&= \sum_{i\alpha\beta\xi}\frac{\partial}{\partial r_\xi}\Big((m^i\|r^j-r\|^2+I^i)\tilde{\theta}^i\tilde{v^i_\xi}\Phi^i\Big) - m^i\frac{\partial\|r^j-r\|^2}{\partial r_\xi}\tilde{\theta}^i\tilde{v^i_\xi}\Phi^i - (m^i\|r^j-r\|^2+I^i)\frac{\partial\tilde{\theta}^i}{\partial r_\xi}\tilde{v^i_\xi}\Phi^i\Big) \\
&\qquad - (m^i\|r^j-r\|^2+I^i)\tilde{\theta}^i\frac{\partial\tilde{v^i_\xi}}{\partial r_\xi}\Phi^i\Big) \\
&= \sum_{i\alpha\beta\xi}\frac{\partial}{\partial r_\xi}\Big((m^i\|r^j-r\|^2+I^i)\tilde{\theta}^i\tilde{v^i_\xi}\Phi^i\Big) - m^i\frac{\partial\|r^j-r\|^2}{\partial r_\xi}\tilde{\theta}^i\tilde{v^i_\xi}\Phi^i + (m^i\|r^j-r\|^2+I^i)\frac{\partial\theta^l}{\partial r_\xi}\tilde{v^i_\xi}\Phi^i\Big) \\
&\qquad + (m^i\|r^j-r\|^2+I^i)\tilde{\theta}^i\frac{\partial v^l_\xi}{\partial r_\xi}\Phi^i\Big) \\
&= \sum_{i\alpha\beta\xi}\frac{\partial}{\partial r_\xi}\Big((m^i\|r^j-r\|^2+I^i)\tilde{\theta}^i\tilde{v^i_\xi}\Phi^i\Big) - m^i\frac{\partial\|r^j-r\|^2}{\partial r_\xi}\tilde{\theta}^i\tilde{v^i_\xi}\Phi^i + (m^i\|r^j-r\|^2+I^i)\frac{\partial\theta^l}{\partial r_\xi}\tilde{v^i_\xi}\Phi^i\Big)
\end{aligned}
\tag{B.10}
$$

B.3 CG Stresses

In order to identified the CG stresses form the dynamical equilibrium, the temporal derivative of the CG momentum is calculated :

$$\begin{aligned}\frac{\partial p_\alpha^{cg}}{\partial t} = \frac{\partial \sum_i^N p_\alpha^i.\Phi^i}{\partial t} = \sum_i^N \left(p_\alpha^i \frac{\partial \Phi^i}{\partial t} + \dot{p}_\alpha^i \Phi^i \right) = \sum_i^N \left(\dot{p}_\alpha^i \Phi^i - p_\alpha^i \sum_\beta^n \frac{\dot{w}_\beta^i}{m^i} \frac{\partial \Phi^i}{\partial r_\beta} \right) \\ = -\Big(\underbrace{\sum_i^N f_\alpha^i \Phi^i}_{A_\alpha} + \underbrace{\sum_i^N p_\alpha^i \sum_\beta^n \frac{p_\beta^i}{m^i} \frac{\partial \Phi^i}{\partial r_\beta}}_{B_\alpha} \Big)\end{aligned} \tag{B.11}$$

$$A_\alpha = \sum_i^N f_\alpha^i \Phi^i = \sum_{ij}^N \sum_{\gamma=1}^{n+m} K_{\alpha\gamma}^{ij} q_\gamma^j \Phi^i = \sum_i^N \left(\sum_{\gamma=1}^{n+m} K_{\alpha\gamma}^{ii} q_\gamma^i \Phi^i + \sum_{j\neq i}^N \sum_{\gamma=1}^{n+m} K_{\alpha\gamma}^{ij} q_\gamma^j \Phi^i \right) \tag{B.12}$$

Using the symmetry properties of the tensor K table 4.1 we get :

$$\begin{aligned}A_\alpha &= \sum_i^N \sum_{\gamma=1}^{n+m} K_{\alpha\gamma}^{ii}.q_\gamma^i.\Phi^i + \sum_{ij\neq i}^N \sum_{\gamma=1}^{n+m} K_{\alpha\gamma}^{ij}.q_\gamma^j.\Phi^i \\ &= \sum_{ij\neq i}^N \left(\sum_{\gamma=1}^n \left(K_{\alpha\gamma}^{ij}.q_\gamma^j.\Phi^i - K_{\alpha\gamma}^{ij}.q_\gamma^i.\Phi^i \right) + \sum_{\gamma=n+1}^{n+m} \left(K_{\alpha\gamma}^{ij}.q_\gamma^j.\Phi^i - K_{\alpha\gamma}^{ij}.q_\gamma^i.\Phi^i - \sum_{\varphi\xi}^n \varepsilon_{\varphi\xi} K_{\alpha\xi}^{ij} r_\varphi^{ij} q_\gamma^i \Phi^i \right) \right) \\ &= \sum_{ij\neq i}^N \left(\sum_{\gamma=1}^n \left(K_{\alpha\gamma}^{ij}.q_\gamma^j.\Phi^i - K_{\alpha\gamma}^{ji}.q_\gamma^j.\Phi^j \right) + \sum_{\gamma=n+1}^{n+m} \left(K_{\alpha\gamma}^{ij}.q_\gamma^j.\Phi^i - K_{\alpha\gamma}^{ji}.q_\gamma^j.\Phi^j - \sum_{\varphi\xi}^n \varepsilon_{\varphi\xi} K_{\alpha\xi}^{ij} (r_\varphi^j - r_\varphi^i) q_\gamma^i \Phi^i \right) \right)\end{aligned} \tag{B.13}$$

$$
\begin{aligned}
&= \sum_{ij\neq i}^{N}\left(\sum_{\gamma=1}^{n}\left(K^{ij}_{\alpha\gamma}.q^{j}_{\gamma}(\Phi^{i}-\Phi^{j})\right)+\sum_{\gamma=n+1}^{n+m}\left(K^{ij}_{\alpha\gamma}.q^{j}_{\gamma}(\Phi^{i}-\Phi^{j})+2.K^{ij}_{\alpha\gamma}q^{j}_{\gamma}.\Phi^{j}-\sum_{\varphi\xi}^{n}\varepsilon_{\varphi\xi}K^{ij}_{\alpha\xi}(r^{j}_{\varphi}-r^{i}_{\varphi})q^{i}_{\gamma}\Phi^{i}\right)\right)\\
&= \sum_{ij\neq i}^{N}\left(\sum_{\gamma=1}^{n+m}\left(K^{ij}_{\alpha\gamma}.q^{j}_{\gamma}.(\Phi^{i}-\Phi^{j})\right)-\sum_{\gamma=n+1}^{n+m}(2.K^{ij}_{\alpha\gamma}+\sum_{\varphi\xi}^{n}\varepsilon_{\varphi\xi}K^{ij}_{\alpha\xi}r^{ij}_{\varphi})q^{i}_{\gamma}\Phi^{i}\right)\\
&= \sum_{ij\neq i}^{N}\left(\sum_{\gamma=1}^{n+m}\left(K^{ij}_{\alpha\gamma}.q^{j}_{\gamma}.(\Phi^{i}-\Phi^{j})\right)+\sum_{\gamma=n+1}^{n+m}(K^{ji}_{\alpha\gamma}+K^{ii}_{\alpha\gamma})q^{i}_{\gamma}\Phi^{i}\right)\\
&= \sum_{ij\neq i}^{N}\sum_{\gamma=1}^{n+m}\left(K^{ij}_{\alpha\gamma}.q^{j}_{\gamma}.(\Phi^{i}-\Phi^{j})\right)+\sum_{ij}^{N}\sum_{\gamma=n+1}^{n+m}K^{ji}_{\alpha\gamma}q^{i}_{\gamma}\Phi^{i}\\
&= \sum_{ij\neq i}^{N}\sum_{\gamma=1}^{n+m}\left(K^{ij}_{\alpha\gamma}.q^{j}_{\gamma}.(\Phi^{i}-\Phi^{j})\right)+\sum_{ij}^{N}\sum_{\gamma=n+1}^{n+m}K^{ij}_{\alpha\gamma}q^{j}_{\gamma}\Phi^{j}
\end{aligned}
\tag{B.14}
$$

In order to introduce the space divergence in the time derivative of the CG momentum one can notice that :

$$
(\Phi^{i}-\Phi^{j})=\widehat{r}^{ji}_{\beta}\int_{0}^{1}\Phi(\overrightarrow{r}-\overrightarrow{\widehat{r}}^{i}+s.\overrightarrow{\widehat{r}}^{ji})ds \tag{B.15}
$$

and it can be defined :

$$
\Phi^{i}=div(\overrightarrow{g^{i}}) \tag{B.16}
$$

Within a cylindrical coordinate system centered on the node i, and with a function $\overrightarrow{g^{i}}$ chosen to be radial, it can be written for a 2D system :

$$
\overrightarrow{g^{i}}=g^{i}\frac{\overrightarrow{r}-\overrightarrow{\widehat{r}}^{i}}{\|\overrightarrow{r}-\overrightarrow{\widehat{r}}^{i}\|}\;;\;div(\overrightarrow{g^{i}})=\frac{1}{\tilde{r}}\frac{\partial\tilde{r}g^{i}(\tilde{r})}{\partial\tilde{r}} \tag{B.17}
$$

With $\tilde{r} = \| \overrightarrow{r} - \overrightarrow{\widehat{r}}^{\,i} \|$

$$\frac{1}{\tilde{r}} \frac{\partial \tilde{r} g^i(\tilde{r})}{\partial \tilde{r}} = \Phi^i = \frac{1}{2.\pi l_{cg}^2} . e^{\frac{-\tilde{r}^2}{2l_{cg}^2}}$$

$$\frac{\partial \tilde{r} g^i(\tilde{r})}{\partial \tilde{r}} = \tilde{r} \frac{1}{2.\pi l_{cg}^2} . e^{\frac{-\tilde{r}^2}{2l_{cg}^2}}$$

$$\tilde{r} g^i(\tilde{r}) = \int_0^{\tilde{r}} s \frac{1}{2.\pi l_{cg}^2} . e^{\frac{-s^2}{2l_{cg}^2}} ds$$

$$g^i(\tilde{r}) = \frac{1}{\tilde{r}} \int_0^{\tilde{r}} s \frac{1}{2.\pi l_{cg}^2} . e^{\frac{-s^2}{2l_{cg}^2}} ds$$

$$g^i(\tilde{r}) = \frac{-1}{\tilde{r}} \frac{1}{2.\pi} . e^{\frac{-\tilde{r}^2}{2l_{cg}^2}} \tag{B.18}$$

Finally :

$$\Phi^i = \sum_{\beta}^{n} \frac{\partial g_\beta^i}{\partial r_\beta} \; with \; g_\beta^i = \frac{r_\beta - \widehat{r}_\beta^i}{\| r_\beta - \widehat{r}_\beta^i \|^2} \frac{-1}{2.\pi} . e^{\frac{-\| r_\beta - \widehat{r}_\beta^i \|^2}{2l_{cg}^2}} \tag{B.19}$$

Note that g_β is not uniquely defined and that there are mutiple possible different choices of g since only $div(\sigma)$ has a physical measurable meaning.

$$\begin{aligned} A_\alpha &= \sum_{ij \neq i}^{N} \sum_{\gamma=1}^{n+m} \left(K_{\alpha\gamma}^{ij} . q_\gamma^j . (\Phi^i - \Phi^j) \right) + \sum_{ij}^{N} \sum_{\gamma=n+1}^{n+m} K_{\alpha\gamma}^{ij} q_\gamma^j \Phi^j \\ &= -\sum_{\beta}^{n} \frac{\partial}{\partial r_\beta} \left(\sum_{ij \neq i}^{N} \sum_{\gamma=1}^{n+m} K_{\alpha\gamma}^{ij} . q_\gamma^j . \widehat{r}_\beta^{ji} \int_0^1 \Phi(\overrightarrow{r} - \overrightarrow{\widehat{r}}^{\,i} + s . \overrightarrow{\widehat{r}}^{\,ji}) ds - \sum_{ij}^{N} \sum_{\gamma=n+1}^{n+m} K_{\alpha\gamma}^{ij} q_\gamma^j g_\beta^j \right) \end{aligned} \tag{B.20}$$

with $\widehat{r}_\beta^{ji} = \widehat{r}_\beta^i - \widehat{r}_\beta^j$

$$B_\alpha = \sum_{i}^{N} \sum_{\beta}^{n} \frac{\partial}{\partial r_\beta} \left(p_\alpha^i \frac{p_\beta^i}{m^i} \right) \Phi^i \tag{B.21}$$

If we defined $\tilde{v}^i_\beta$ as :

$$\tilde{v}^i_\beta = \frac{p^i_\beta}{m^i} - v^{cg}_\beta \tag{B.22}$$

It is to be noted that :

$$\sum_i^N m^i \tilde{v}^i_\beta \Phi^i = \sum_i^N m^i (\frac{p^i_\beta}{m^i}\Phi^i - v^{cg}_\beta \Phi^i) = (\sum_i^N p^i_\beta \Phi^i - v^{cg}_\beta \sum_i^N m^i \Phi^i) = p^{cg}_\beta - \rho^{cg} v^{cg}_\beta = 0 \tag{B.23}$$

The term B thus becomes :

$$\begin{aligned} B_\alpha &= \sum_i^N \sum_\beta^n \frac{\partial}{\partial r_\beta}\Big(m^i \frac{p^i_\alpha}{m^i}\frac{p^i_\beta}{m^i}\Phi^i\Big) \\ &= \sum_i^N \sum_\beta^n \frac{\partial}{\partial r_\beta}\Big(m^i (\tilde{v}^i_\alpha + v^{cg}_\alpha)(\tilde{v}^i_\beta + v^{cg}_\beta)\Phi^i\Big) \\ &= \sum_i^N \sum_\beta^n \frac{\partial}{\partial r_\beta}\Big(m^i (\tilde{v}^i_\alpha . \tilde{v}^i_\beta + v^{cg}_\alpha v^{cg}_\beta)\Phi^i\Big) \\ &= \sum_i^N \sum_\beta^n \frac{\partial}{\partial r_\beta}\Big(m^i \tilde{v}^i_\alpha . \tilde{v}^i_\beta \Phi^i + \rho^{cg} v^{cg}_\alpha v^{cg}_\beta\Big) \end{aligned} \tag{B.24}$$

To recapitulate :

$$\begin{aligned} &\frac{\partial p^{cg}_\alpha}{\partial t} = -A_\alpha - B_\alpha = \\ &\sum_\beta^n \frac{\partial}{\partial r_\beta}\Big(\sum_{ij\neq i}^N \sum_{\gamma=1}^{n+m} K^{ij}_{\alpha\gamma} . q^j_\gamma . \widehat{r}^{ji}_\beta \int_0^1 \Phi(\overrightarrow{r} - \overrightarrow{\widehat{r}}^{\,i} + s.\overrightarrow{\widehat{r}}^{\,ji}) ds - \sum_{ij}^N \sum_{\gamma=n+1}^{n+m} K^{ij}_{\alpha\gamma} q^j_\gamma g^j_\beta - (\sum_i^N m^i \tilde{v}^i_\alpha . \tilde{v}^i_\beta \Phi^i + \rho^{cg} v^{cg}_\alpha v^{cg}_\beta)\Big) \end{aligned} \tag{B.25}$$

Thus the CG stress can be identified form the dynamic equilibrium :

$$\frac{\partial p^{cg}_\alpha}{\partial t} = \sum_\beta \frac{\partial}{\partial r_\beta}\Big(\sigma_{\alpha\beta} - \rho_{cg} v^{cg}_\alpha v^{cg}_\beta\Big) \tag{B.26}$$

B.4 CG Torques

In order to identified the CG torques form the dynamical equilibrium, the temporal derivative of the CG angular momentum is calculated :

$$\begin{aligned}
\frac{\partial J^{cg}}{\partial t} &= \frac{\partial}{\partial t}\left(\sum_i^N\left(\sum_{\varphi\xi}^n \varepsilon_{\varphi\xi}(r_\varphi^i - r_\varphi)p_\xi^i + J^i\right)\Phi^i\right) \\
&= \sum_i^N \frac{\partial}{\partial t}\left(\sum_{\varphi\xi}^n \varepsilon_{\varphi\xi}\left((r_\varphi^i - r_\varphi)p_\xi^i + J^i\right)\Phi^i + \sum_i^N\sum_{\varphi\xi}^n \varepsilon_{\varphi\xi}\left((r_\varphi^i - r_\varphi)p_\xi^i + J^i\right)\frac{\partial \Phi^i}{\partial t}\right. \\
&= \sum_i^N\sum_{\varphi\xi}^n \varepsilon_{\varphi\xi}\left((r_\varphi^i - r_\varphi)\dot{p}_\xi^i + \dot{J}^i\right)\Phi^i - \sum_i^N\sum_\beta^n\sum_{\varphi\xi}^n \varepsilon_{\varphi\xi}\left((r_\varphi^i - r_\varphi)p_\xi^i + J^i\right)\frac{p_\beta^i}{m^i}\frac{\partial \Phi^i}{\partial r_\beta} \\
&= \sum_i^N\sum_{\varphi\xi}^n \varepsilon_{\varphi\xi}\left((r_\varphi^i - r_\varphi)\dot{p}_\xi^i + \dot{J}^i\right)\Phi^i - \sum_i^N\sum_\beta^n\sum_{\varphi\xi}^n \varepsilon_{\varphi\xi}\left((r_\varphi^i - r_\varphi)p_\xi^i + J^i\right)\frac{p_\beta^i}{m^i}\frac{\partial \Phi^i}{\partial r_\beta} \\
&= -\Bigg(\underbrace{\sum_{ij}^N\sum_{\varphi\xi}^n\sum_{\gamma=1}^{n+m} \varepsilon_{\varphi\xi}(r_\varphi^i - r_\varphi)K_{\xi\gamma}^{ij}q_\gamma^j\Phi^i}_{C_n} + \underbrace{\sum_{ij}^N\sum_{\gamma=1}^{n+m} K_{\theta\gamma}^{ij}q_\gamma^j\Phi^i}_{C_\theta}\Bigg) \\
&\quad - \underbrace{\sum_i^N\sum_\beta^n\sum_{\varphi\xi}^n(\varepsilon_{\varphi\xi}(r_\varphi^i - r_\varphi)p_\xi^i + J^i)\frac{p_\beta^i}{m^i}\frac{\partial \Phi^i}{\partial r_\beta}}_{D}
\end{aligned} \tag{B.27}$$

The calculation of the terms are detailed in the following :

$$\begin{aligned}
D &= \sum_i^N\sum_\beta^n\sum_{\varphi\xi}^n(\varepsilon_{\varphi\xi}(r_\varphi^i - r_\varphi)p_\xi^i + J^i)\frac{p_\beta^i}{m^i}.\frac{\partial \Phi^i}{\partial r_\beta} \\
&= \sum_i^N\sum_\beta^n\sum_{\varphi\xi}^n \frac{\partial}{\partial r_\beta}\left((\varepsilon_{\varphi\xi}(r_\varphi^i - r_\varphi)p_\xi^i + J^i)\frac{p_\beta^i}{m^i}.\Phi^i\right) + \sum_i^N\sum_\beta^n\sum_{\varphi\xi}^n \varepsilon_{\beta\xi}p_\xi^i\frac{p_\beta^i}{m^i}.\Phi^i \\
&= \sum_i^N\sum_\beta^n\sum_{\varphi\xi}^n \frac{\partial}{\partial r_\beta}\left((\varepsilon_{\varphi\xi}(r_\varphi^i - r_\varphi)p_\xi^i + J^i)\frac{p_\beta^i}{m^i}.\Phi^i\right)
\end{aligned} \tag{B.28}$$

Using the previously introduced definition of $\tilde{v}_\beta^i = \frac{p_\beta^i}{m^i} - v_\beta^{cg}$:

$$= \sum_{i}^{N} \sum_{\beta}^{n} \sum_{\varphi\xi}^{n} \frac{\partial}{\partial r_\beta} \Big((\varepsilon_{\varphi\xi}(r^i_\varphi - r_\varphi) p^i_\xi + J^i)(\tilde{v}^i_\beta + v^{cg}_\beta).\Phi^i \Big)$$

$$= \sum_{i}^{N} \sum_{\beta}^{n} \sum_{\varphi\xi}^{n} \frac{\partial}{\partial r_\beta} \Big((\varepsilon_{\varphi\xi}(r^i_\varphi - r_\varphi) p^i_\xi + J^i)\tilde{v}^i_\beta.\Phi^i + J^{cg} v^{cg}_\beta \Big) \tag{B.29}$$

If the displacement and rotational components of γ are separated it can be written :

$$C_n = \sum_{ij}^{N} \sum_{\varphi\xi}^{n} \sum_{\gamma=1}^{n+m} \varepsilon_{\varphi\xi}(r^i_\varphi - r_\varphi) K^{ij}_{\xi\gamma}.q^j_\gamma.\Phi^i$$

$$= \sum_{ij}^{N} \sum_{\varphi\xi}^{n} \Big(\varepsilon_{\varphi\xi}(r^i_\varphi - r_\varphi) \Big(\sum_{\gamma=1}^{n} K^{ij}_{\xi\gamma}.q^j_\gamma.\Phi^i + \sum_{\gamma=n+1}^{n+m} K^{ij}_{\xi\gamma}.q^j_\gamma.\Phi^i \Big) \Big)$$

$$= \underbrace{\sum_{ij}^{N} \sum_{\varphi\xi}^{n} \sum_{\gamma=1}^{n} \varepsilon_{\varphi\xi}(r^i_\varphi - r_\varphi) K^{ij}_{\xi\gamma}.q^j_\gamma.\Phi^i}_{C^n_n} + \underbrace{\sum_{ij}^{N} \sum_{\varphi\xi}^{n} \sum_{\gamma=n+1}^{n+m} \varepsilon_{\varphi\xi}(r^i_\varphi - r_\varphi) K^{ij}_{\xi\gamma}.q^j_\gamma.\Phi^i}_{c^m_n} \tag{B.30}$$

Using the relations and symmetries of the stiffness matrix these terms can be re-written :

$$C^n_n = \sum_{ij}^{N} \sum_{\varphi\xi}^{n} \sum_{\gamma=1}^{n} \varepsilon_{\varphi\xi}(r^i_\varphi - r_\varphi) K^{ij}_{\xi\gamma}.q^j_\gamma.\Phi^i$$

$$= \sum_{ij\neq i}^{N} \sum_{\varphi\xi}^{n} \sum_{\gamma=1}^{n} \varepsilon_{\varphi\xi} \Big((r^i_\varphi - r_\varphi) K^{ij}_{\xi\gamma}.q^j_\gamma.\Phi^i - (r^i_\varphi - r_\varphi) K^{ij}_{\xi\gamma}.q^i_\gamma.\Phi^i \Big)$$

$$= \sum_{ij\neq i}^{N} \sum_{\varphi\xi}^{n} \sum_{\gamma=1}^{n} \varepsilon_{\varphi\xi} \Big((r^i_\varphi - r_\varphi) K^{ij}_{\xi\gamma}.q^j_\gamma.\Phi^i - (r^j_\varphi - r_\varphi) K^{ij}_{\xi\gamma}.q^j_\gamma.\Phi^j \Big)$$

$$= \sum_{ij\neq i}^{N} \sum_{\varphi\xi}^{n} \sum_{\gamma=1}^{n} \varepsilon_{\varphi\xi} \Big((r^i_\varphi - r_\varphi) K^{ij}_{\xi\gamma}.q^j_\gamma.(\Phi^i - \Phi^j) - r^{ij}_\varphi K^{ij}_{\xi\gamma}.q^j_\gamma.\Phi^j \Big) \tag{B.31}$$

$$
\begin{aligned}
C_n^m &= \sum_{ij}^{N}\sum_{\varphi\xi}^{n}\sum_{\gamma=n+1}^{n+m} \varepsilon_{\varphi\xi}(r_\varphi^i - r_\varphi) K_{\xi\gamma}^{ij}.q_\gamma^j.\Phi^i \\
&= \sum_{ij\neq i}^{N}\sum_{\varphi\xi}^{n}\sum_{\gamma=n+1}^{n+m} \varepsilon_{\varphi\xi}\Big((r_\varphi^i - r_\varphi) K_{\xi\gamma}^{ij}.q_\gamma^j.\Phi^i - (r_\varphi^i - r_\varphi) K_{\xi\gamma}^{ij}.q_\gamma^i.\Phi^i - (r_\varphi^i - r_\varphi)\sum_{\phi\chi}\varepsilon_{\phi\chi} r_\phi^{ij} K_{\xi\chi}^{ij}.q_\gamma^i.\Phi^i \Big) \\
&= \sum_{ij\neq i}^{N}\sum_{\varphi\xi}^{n}\sum_{\gamma=n+1}^{n+m} \varepsilon_{\varphi\xi}\Big((r_\varphi^i - r_\varphi) K_{\xi\gamma}^{ij}.q_\gamma^j.\Phi^i + (r_\varphi^j - r_\varphi) K_{\xi\gamma}^{ij}.q_\gamma^j.\Phi^j - (r_\varphi^i - r_\varphi)\sum_{\phi\chi}\varepsilon_{\phi\chi} r_\phi^{ij} K_{\xi\chi}^{ij}.q_\gamma^i.\Phi^i \Big)
\end{aligned}
\tag{B.32}
$$

$$
\begin{aligned}
&= \sum_{ij\neq i}^{N}\sum_{\varphi\xi}^{n}\sum_{\gamma=n+1}^{n+m} \varepsilon_{\varphi\xi}\Big((r_\varphi^i - r_\varphi) K_{\xi\gamma}^{ij}.q_\gamma^j.(\Phi^i - \Phi^j) - r_\varphi^{ij} K_{\xi\gamma}^{ij}.q_\gamma^j.\Phi^j + (r_\varphi^j - r_\varphi) 2.K_{\xi\gamma}^{ij}.q_\gamma^j.\Phi^j \\
&\qquad\qquad - (r_\varphi^i - r_\varphi)\sum_{\phi\chi}\varepsilon_{\phi\chi} r_\phi^{ij} K_{\xi\chi}^{ij}.q_\gamma^i.\Phi^i \Big) \\
&= \sum_{ij\neq i}^{N}\sum_{\varphi\xi}^{n}\sum_{\gamma=n+1}^{n+m} \varepsilon_{\varphi\xi}\Big((r_\varphi^i - r_\varphi) K_{\xi\gamma}^{ij}.q_\gamma^j.(\Phi^i - \Phi^j) - r_\varphi^{ij} K_{\xi\gamma}^{ij}.q_\gamma^j.\Phi^j - (r_\varphi^i - r_\varphi) 2.K_{\xi\gamma}^{ij}.q_\gamma^i.\Phi^i \\
&\qquad\qquad - (r_\varphi^i - r_\varphi)\sum_{\phi\chi}\varepsilon_{\phi\chi} r_\phi^{ij} K_{\xi\chi}^{ij}.q_\gamma^i.\Phi^i \Big)
\end{aligned}
\tag{B.33}
$$

$$
\begin{aligned}
&= \sum_{ij\neq i}^{N}\sum_{\varphi\xi}^{n}\sum_{\gamma=n+1}^{n+m} \varepsilon_{\varphi\xi}\Big((r_\varphi^i - r_\varphi) K_{\xi\gamma}^{ij}.q_\gamma^j.(\Phi^i - \Phi^j) - r_\varphi^{ij} K_{\xi\gamma}^{ij}.q_\gamma^j.\Phi^j \Big) + \sum_{ij\neq i}^{N}\sum_{\varphi\xi}^{n}\sum_{\gamma=n+1}^{n+m} (r_\varphi^i - r_\varphi)\Big(K_{\xi\gamma}^{ji} + K_{\xi\gamma}^{ii} \Big).q_\gamma^i.\Phi^i \\
&= \sum_{ij\neq i}^{N}\sum_{\varphi\xi}^{n}\sum_{\gamma=n+1}^{n+m} \varepsilon_{\varphi\xi}\Big((r_\varphi^i - r_\varphi) K_{\xi\gamma}^{ij}.q_\gamma^j.(\Phi^i - \Phi^j) - r_\varphi^{ij} K_{\xi\gamma}^{ij}.q_\gamma^j.\Phi^j \Big) + \sum_{ij}^{N}\sum_{\varphi\xi}^{n}\sum_{\gamma=n+1}^{n+m} \varepsilon_{\varphi\xi}(r_\varphi^i - r_\varphi) K_{\xi\gamma}^{ji}.q_\gamma^i.\Phi^i \\
&= \sum_{ij\neq i}^{N}\sum_{\varphi\xi}^{n}\sum_{\gamma=n+1}^{n+m} \varepsilon_{\varphi\xi}\Big((r_\varphi^i - r_\varphi) K_{\xi\gamma}^{ij}.q_\gamma^j.(\Phi^i - \Phi^j) - r_\varphi^{ij} K_{\xi\gamma}^{ij}.q_\gamma^j.\Phi^j \Big) + \sum_{ij}^{N}\sum_{\varphi\xi}^{n}\sum_{\gamma=n+1}^{n+m} \varepsilon_{\varphi\xi}(r_\varphi^j - r_\varphi) K_{\xi\gamma}^{ij}.q_\gamma^j.\Phi^j
\end{aligned}
\tag{B.34}
$$

By regrouping the components of γ :

$$C_n = C_n^n + C_n^m = \sum_{ij\neq i}^{N}\sum_{\varphi\xi}^{n}\sum_{\gamma=1}^{n+m}\varepsilon_{\varphi\xi}\left((r_\varphi^i - r_\varphi)K_{\xi\gamma}^{ij}.q_\gamma^j.(\Phi^i-\Phi^j) - r_\varphi^{ij}K_{\xi\gamma}^{ij}.q_\gamma^j.\Phi^j\right) + \sum_{ij}^{N}\sum_{\varphi\xi}^{n}\sum_{\gamma=n+1}^{n+m}\varepsilon_{\varphi\xi}(r_\varphi^j - r_\varphi)K_{\xi\gamma}^{ij}.q_\gamma^j.\Phi^j \tag{B.35}$$

For a later simplification we can rewrite for $m = 1$

$$-\sum_{ij\neq i}^{N}\sum_{\varphi\xi}^{n}\sum_{\gamma=1}^{n+m}\varepsilon_{\varphi\xi}r_\varphi^{ij}K_{\xi\gamma}^{ij}.q_\gamma^j.\Phi^j = -\sum_{ij\neq i}^{N}\sum_{\varphi\xi}^{n}\sum_{\gamma=1}^{n+m}\varepsilon_{\varphi\xi}r_\varphi^{ij}K_{\gamma\xi}^{ji}.q_\gamma^j.\Phi^j = -\sum_{ij\neq i}^{N}\sum_{\varphi\xi}^{n}\sum_{\gamma=1}^{n+m}\varepsilon_{\varphi\xi}r_\varphi^{ji}K_{\gamma\xi}^{ij}.q_\gamma^i.\Phi^i$$
$$=\sum_{ij\neq i}^{N}\sum_{\varphi\xi}^{n}\sum_{\gamma=1}^{n+m}\varepsilon_{\varphi\xi}r_\varphi^{ij}K_{\gamma\xi}^{ij}.q_\gamma^i.\Phi^i = -\sum_{ij}^{N}\sum_{\gamma=1}^{n+m}K_{\gamma\theta}^{ij}.q_\gamma^i.\Phi^i = -\sum_{ij}^{N}\sum_{\gamma=1}^{n+m}K_{\gamma\theta}^{ji}.q_\gamma^j.\Phi^j = -\sum_{ij}^{N}\sum_{\gamma=1}^{n+m}K_{\theta\gamma}^{ij}.q_\gamma^j.\Phi^j \tag{B.36}$$

Thus :

$$C_n = \sum_{ij\neq i}^{N}\sum_{\varphi\xi}^{n}\sum_{\gamma=1}^{n+m}\varepsilon_{\varphi\xi}(r_\varphi^i - r_\varphi)K_{\xi\gamma}^{ij}.q_\gamma^j.(\Phi^i-\Phi^j) - \sum_{ij}^{N}\sum_{\gamma=1}^{n+m}K_{\theta\gamma}^{ij}.q_\gamma^j.\Phi^j + \sum_{ij}^{N}\sum_{\varphi\xi}^{n}\sum_{\gamma=n+1}^{n+m}\varepsilon_{\varphi\xi}(r_\varphi^j - r_\varphi)K_{\xi\gamma}^{ij}.q_\gamma^j.\Phi^j \tag{B.37}$$

$$C_\theta = \sum_{ij}^{N}\sum_{\gamma=1}^{n+m}K_{\theta\gamma}^{ij}.q_\gamma^j.\Phi^i = \sum_{ij}^{N}\left(\sum_{\gamma=1}^{n}K_{\theta\gamma}^{ij}.q_\gamma^j.\Phi^i + \sum_{\gamma=n+1}^{n+m}K_{\theta\gamma}^{ij}.q_\gamma^j.\Phi^i\right)$$
$$=\sum_{ij\neq i}^{N}\left(\sum_{\gamma=1}^{n}\left(K_{\theta\gamma}^{ij}.q_\gamma^j.\Phi^i - K_{\theta\gamma}^{ij}.q_\gamma^i.\Phi^i\right) + \sum_{\gamma=n+1}^{n+m}\left(K_{\theta\gamma}^{ij}.q_\gamma^j.\Phi^i - K_{\theta\gamma}^{ij}.q_\gamma^i.\Phi^i - \sum_{\varphi\xi}^{n}\varepsilon_{\varphi\xi}K_{\theta\xi}^{ij}r_\varphi^{ij}.q_\gamma^i.\Phi^i\right)\right)$$
$$=\sum_{ij\neq i}^{N}\left(\sum_{\gamma=1}^{n}\left(K_{\theta\gamma}^{ij}.q_\gamma^j.\Phi^i + K_{\theta\gamma}^{ij}.q_\gamma^j.\Phi^j\right) + \sum_{\gamma=n+1}^{n+m}\left(K_{\theta\gamma}^{ij}.q_\gamma^j.\Phi^i - K_{\theta\gamma}^{ij}.q_\gamma^j.\Phi^j - \sum_{\varphi\xi}^{n}\varepsilon_{\varphi\xi}K_{\theta\xi}^{ij}r_\varphi^{ij}.q_\gamma^i.\Phi^i\right)\right) \tag{B.38}$$

$$
\begin{aligned}
&= \sum_{ij\neq i}^{N}\left(\sum_{\gamma=1}^{n}\left(K^{ij}_{\theta\gamma}.q^{j}_{\gamma}.(\Phi^{i}-\Phi^{j})-2.K^{ij}_{\theta\gamma}.q^{i}_{\gamma}.\Phi^{i}\right)\right)+\sum_{ij\neq i}^{N}\sum_{\gamma=n+1}^{n+m}K^{ij}_{\theta\gamma}.q^{j}_{\gamma}.(\Phi^{i}-\Phi^{j})+\sum_{ij}^{N}\sum_{\gamma=n+1}^{n+m}K^{ij}_{\theta\gamma}.q^{i}_{\gamma}.\Phi^{i}\\
&= \sum_{ij\neq i}^{N}\sum_{\gamma=1}^{n+m}K^{ij}_{\theta\gamma}.q^{j}_{\gamma}.(\Phi^{i}-\Phi^{j})-\sum_{ij\neq i}^{N}\sum_{\gamma=1}^{n}2.K^{ij}_{\theta\gamma}.q^{i}_{\gamma}.\Phi^{i}+\sum_{ij}^{N}\sum_{\gamma=n+1}^{n+m}K^{ij}_{\theta\gamma}.q^{i}_{\gamma}.\Phi^{i}\\
&= \sum_{ij\neq i}^{N}\sum_{\gamma=1}^{n+m}K^{ij}_{\theta\gamma}.q^{j}_{\gamma}.(\Phi^{i}-\Phi^{j})+\sum_{ij\neq i}^{N}\sum_{\gamma=1}^{n}(K^{ji}_{\theta\gamma}+K^{ii}_{\theta\gamma}).q^{i}_{\gamma}.\Phi^{i}+\sum_{ij}^{N}\sum_{\gamma=n+1}^{n+m}K^{ij}_{\theta\gamma}.q^{j}_{\gamma}.\Phi^{j}\\
&= \sum_{ij\neq i}^{N}\sum_{\gamma=1}^{n+m}K^{ij}_{\theta\gamma}.q^{j}_{\gamma}.(\Phi^{i}-\Phi^{j})+\sum_{ij}^{N}\sum_{\gamma=1}^{n+m}K^{ij}_{\theta\gamma}.q^{j}_{\gamma}.\Phi^{j}
\end{aligned}
\tag{B.39}
$$

$$
\begin{aligned}
C_n+C_\theta = &\sum_{ij\neq i}^{N}\sum_{\gamma=1}^{n+m}K^{ij}_{\theta\gamma}.q^{j}_{\gamma}.(\Phi^{i}-\Phi^{j})+\sum_{ij\neq i}^{N}\sum_{\varphi\xi}^{n}\sum_{\gamma=1}^{n+m}\varepsilon_{\varphi\xi}(r^{i}_{\varphi}-r_{\varphi})K^{ij}_{\xi\gamma}.q^{j}_{\gamma}.(\Phi^{i}-\Phi^{j})\\
&+\sum_{ij}^{N}\sum_{\varphi\xi}^{n}\sum_{\gamma=n+1}^{n+m}\varepsilon_{\varphi\xi}(r^{j}_{\varphi}-r_{\varphi})K^{ij}_{\xi\gamma}.q^{j}_{\gamma}.\Phi^{j}
\end{aligned}
\tag{B.40}
$$

Using the same methods for introducing the spatial derivatives as in B.3 :

$$
\begin{aligned}
C_n+C_\theta = &-\sum_{ij\neq i}^{N}\sum_{\varphi\xi}^{n}\sum_{\gamma=1}^{n+m}\left(\left(\varepsilon_{\varphi\xi}(r^{i}_{\varphi}-r_{\varphi})K^{ij}_{\xi\gamma}.q^{j}_{\gamma}+K^{ij}_{\theta\gamma}.q^{j}_{\gamma}\right).\sum_{\beta}^{n}\frac{\partial}{\partial r_\beta}\left(\widehat{r}^{ji}_{\beta}\int_0^1\Phi(\overrightarrow{r}-\overrightarrow{\widehat{r}}^{\,i}+s.\overrightarrow{\widehat{r}}^{\,ji})ds\right)\right)\\
&+\sum_{ij}^{N}\sum_{\gamma=n+1}^{n+m}\varepsilon_{\varphi\xi}(r^{j}_{\varphi}-r_{\varphi})K^{ij}_{\xi\gamma}q^{j}_{\gamma}.\sum_{\beta}^{n}\frac{\partial g^{j}_{\beta}}{\partial r_\beta}
\end{aligned}
\tag{B.41}
$$

$$
\begin{aligned}
= &-\sum_{\beta}^{n}\frac{\partial}{\partial r_\beta}\left(\sum_{ij\neq i}^{N}\sum_{\varphi\xi}^{n}\sum_{\gamma=1}^{n+m}(\varepsilon_{\varphi\xi}(r^{i}_{\varphi}-r_{\varphi})K^{ij}_{\xi\gamma}.q^{j}_{\gamma}+K^{ij}_{\theta\gamma}.q^{j}_{\gamma}).\widehat{r}^{ji}_{\beta}\int_0^1\Phi(\overrightarrow{r}-\overrightarrow{\widehat{r}}^{\,i}+s.\overrightarrow{\widehat{r}}^{\,ji})ds\right.\\
&\left.-\sum_{ij}^{N}\sum_{\gamma=n+1}^{n+m}\varepsilon_{\varphi\xi}(r^{j}_{\varphi}-r_{\varphi})K^{ij}_{\xi\gamma}q^{j}_{\gamma}g^{j}_{\beta}\right)\\
&-\sum_{\beta\xi}^{n}\varepsilon_{\beta\xi}\Big(\sum_{ij\neq i}^{N}\sum_{\gamma=1}^{n+m}K^{ij}_{\xi\gamma}.q^{j}_{\gamma}.\widehat{r}^{ji}_{\beta}\int_0^1\Phi(\overrightarrow{r}-\overrightarrow{\widehat{r}}^{\,i}+s.\overrightarrow{\widehat{r}}^{\,ji})ds-\sum_{ij}^{N}\sum_{\gamma=n+1}^{n+m}K^{ij}_{\xi\gamma}q^{j}_{\gamma}g^{j}_{\beta}\Big)
\end{aligned}
\tag{B.42}
$$

To recapitulate :

$$
\begin{aligned}
\frac{\partial J^{cg}}{\partial t} &= -C_n - C_\theta - D \\
&= \sum_\beta^n \frac{\partial}{\partial r_\beta} \Bigg(\sum_{ij\neq i}^N \sum_{\varphi\xi}^n \sum_{\gamma=1}^{n+m} (\varepsilon_{\varphi\xi}(r_\varphi^i - r_\varphi) K_{\xi\gamma}^{ij}.q_\gamma^j + K_{\theta\gamma}^{ij}.q_\gamma^j).\widehat{r}_\beta^{ji} \int_0^1 \Phi(\overrightarrow{r} - \overrightarrow{\widehat{r}}^{\,i} + s.\overrightarrow{\widehat{r}}^{\,ji}) ds \\
&\quad - \sum_{ij}^N \sum_{\gamma=n+1}^{n+m} \varepsilon_{\varphi\xi}(r_\varphi^j - r_\varphi) K_{\xi\gamma}^{ij} q_\gamma^j g_\beta^j - \sum_i^N (\sum_{\varphi\xi}^n \varepsilon_{\varphi\xi}(r_\varphi^i - r_\varphi) p_\xi^i + J^i) \tilde{v}_\beta^i.\Phi^i - J^{cg} v_\beta^{cg} \Bigg) \\
&\quad - \sum_{\xi\beta}^n \varepsilon_{\xi\beta} \Big(\sum_{ij\neq i}^N \sum_{\gamma=1}^{n+m} K_{\xi\gamma}^{ij}.q_\gamma^j.\widehat{r}_\beta^{ji} \int_0^1 \Phi(\overrightarrow{r} - \overrightarrow{\widehat{r}}^{\,i} + s.\overrightarrow{\widehat{r}}^{\,ji}) ds - \sum_{ij}^N \sum_{\gamma=n+1}^{n+m} K_{\xi\gamma}^{ij} q_\gamma^j g_\beta^j \Big) \\
&= \sum_\beta^n \frac{\partial}{\partial r_\beta} \Bigg(\sum_{ij\neq i}^N \sum_{\varphi\xi}^n \sum_{\gamma=1}^{n+m} (\varepsilon_{\varphi\xi}(r_\varphi^i - r_\varphi) K_{\xi\gamma}^{ij}.q_\gamma^j + K_{\theta\gamma}^{ij}.q_\gamma^j).\widehat{r}_\beta^{ji} \int_0^1 \Phi(\overrightarrow{r} - \overrightarrow{\widehat{r}}^{\,i} + s.\overrightarrow{\widehat{r}}^{\,ji}) ds \\
&\quad - \sum_{ij}^N \sum_{\gamma=n+1}^{n+m} \varepsilon_{\varphi\xi}(r_\varphi^j - r_\varphi) K_{\xi\gamma}^{ij} q_\gamma^j g_\beta^j - \sum_i^N (\sum_{\varphi\xi}^n \varepsilon_{\varphi\xi}(r_\varphi^i - r_\varphi) p_\xi^i + J^i) \tilde{v}_\beta^i.\Phi^i - J^{cg} v_\beta^{cg} \Bigg) \\
&\quad - \sum_{\xi\beta}^n \varepsilon_{\xi\beta}\sigma_{\xi\beta}
\end{aligned}
\tag{B.43}
$$

At last the torques can be identified from :

$$
\frac{\partial J^{cg}}{\partial t} = \sum_\beta^n \frac{\partial}{\partial r_\beta} \Big(m_\beta - v_\beta^{cg} J^{cg} \Big) - \sum_{\beta\gamma}^n \varepsilon_{\beta\gamma}\sigma_{\beta\gamma} \tag{B.44}
$$

FOLIO ADMINISTRATIF

THÈSE SOUTENUE DEVANT L'INSTITUT NATIONAL DES SCIENCES APPLIQUÉES DE LYON

NOM : Glacet
Prénoms : Arthur

DATE de SOUTENANCE : 16/07/2018

TITRE : **Study of Quasi-Periodic Architectured materials :** Vibrations, Dynamic Fracture and Homogenization

NATURE : Doctorat

Numéro d'ordre :

École doctorale : MEGA
Spécialité : Mécanique - Génie Mécanique - Génie Civil

Cote B.I.U. - Lyon : / et bis

CLASSE :

RÉSUMÉ :
Les Structures Quasi-périodiques (QP) on montrées des propriétés particulières dans de domaine atomique, notamment dans le domaine vibrationnel. Il pourrais être intéressant de pouvoir transférer ces propriétés à des méta-matériaux macroscopiques. Des réseaux de poutres quasi-périodique 2D sont étudiés dans cette thèse du fait de la simplicité du modèle élément finis (EF) poutre Euler Bernoulli usuellement utilisé pour la modélisation des réseaux de poutres. Ces réseaux de poutres peuvent facilement être produit par fabrication additive ou par découpe laser. Il est possible de faire varier l'élancement des poutre (le ratio hauteur sur longueur) qui est un paramètre intéressant pour modifier la réponse mécanique du réseau. En utilisant la méthode EF l'influence de l'élancement des poutres sur la réponse vibrationnel des réseaux de poutres QP vas être étudiée. La méthode numérique Kernel Polynomial est adapté avec sucés de la dynamique moléculaire aux réseaux de poutres pour étudier leurs modes vibratoires sans avoir a diagonaliser complètement la matrice dynamique. Les réseaux de poutres QP pressentent des propriétés similaire à leur compère atomique : localisation de mode sur des sous-structures et relation de dispersion hiérarchisée. Le comportement à la fracture est aussi étudié étant donné que les symétrie présentent dans les QP pourrais permettre des réseaux de poutres QP ne présentant pas de plan faibles pour la propagation de fissures. Cela a été prouvé vrai d'après des calcul EF statique avec un critère de fracture fragile sur l'énergie de déformation. Les simulation statique ne suffisent pas car elles ne peuvent capturer les phénomène dynamique complexe qui apparaissent lors de la fissuration fragile. Les propriétés de vibration du QP pourrais aussi avoir un impact sur la propagation dynamique de fissure. Un modèle dynamique de fissuration est développée afin d'étudier l'impact de l'élancement sur la capacité des réseaux de poutres QP à dissiper de l'énergie par fissuration . Finalement une méthode Coarse Graining est développée pour identifier un milieux cosserat continue équivalant au réseau de poutres QP pour différentes échelles. Cette méthode permet d'identifier la densité, les déformations, les contraintes et donc le modules d'élasticité du milieu cosserat équivalant. Cela permet une meilleur compréhension du rôle des sous structures précédemment identifiées.

MOTS-CLÉS : Quasi-periodique, Éléments Finis, Réseaux de Poutres , Vibration , Fracture, Coarse Graining.

Laboratoire(s) de recherche : Laboratoire de Mécanique des Contacts et des Structures
UMR CNRS 5259 - INSA de Lyon
18-20 rue des Sciences
69621 Villeurbanne Cedex FRANCE

Directeur de thèse : TANGUY Anne

Co-directeur de thèse : RÉTHORÉ Julien

Président du jury : le président
Composition du jury :

KONDO DJIMÉDO	Professeur, Université Pierre-et-Marie-Curie	Rapporteur
LAZARUS VÉRONIQUE	Directrice de Recheche, ENSTA ParisTech	Rapporteur
MORESTIN FABRICE	Professeur, INSA-Lyon	Examinateur
MOSSÉRI RÉMY	Directeur de Recheche, Université Pierre-et-Marie-Curie	Examinateur
RÉTHORÉ JULIEN	Directeur de recherche CNRS, Centrale Nantes	Co-Directeur de thèse
TANGUY ANNE	Professeur , INSA-Lyon,	Directrice de thèse